WAVE INDUCED MOTION OF SMALL ICE MASSES

DARYL ATTWOOD

WAVE INDUCED MOTION OF SMALL ICE MASSES

BY

© DARYL ATTWOOD, B.ENG.

A THESIS SUBMITTED TO THE SCHOOL OF
GRADUATE STUDIES IN PARTIAL FULFILLMENT OF
THE REQUIREMENTS FOR THE DEGREE OF
MASTER OF ENGINEERING

FACULTY OF ENGINEERING AND APPLIED SCIENCE
MEMORIAL UNIVERSITY OF NEWFOUNDLAND

OCTOBER 1986

ST. JOHN'S NEWFOUNDLAND

ISBN 0-315-45088-6

ERROR STATEMENT

The wave and motion spectra generated in this work were amplitude spectra, as opposed to energy spectra. Because of this, significant motions and wave heights should have been determined by multiplying the areas under the appropriate spectra by a factor of 2.8, rather than the value 4.0 reported on page 78. The error applies to both the actual response spectra and those generated by combining wave spectra with RAO's, and therefore the comparisons between these groups of spectra is completely correct. However, the significant wave heights reported in Table 3 on page 15 and the significant motions in Tables 5 and 6 on pages 85 and 104 respectively should be smaller by a factor SQRT(2). I include the corrected values below. Also, the scales on Figures 59-66 should be smaller by the same SQRT(2). Finally, Figures 9-12 compare Jonswap energy spectra to my actual amplitude spectra. A more realistic comparison of the measured and target spectra is shown below, depicting amplitude spectra for both cases.

IRREGULAR WAVE EXPERIMENTS

MODEL	TEST	MEASURED SIGNIFICANT WAVE HEIGHT (cm)
LARGE CUBE	LIR857	10.0
	LIR1143	14.1
CYLINDER	CIR857	8.7
	CIR1143	11.5
	CIR1429	15.4
TRAPEZOID	TIR857	9.5
	TIR1143	13.2
	TIR1429	16.0
SPHERE	SIR857	6.3
	SIR1143	11.2
	SIR1429	12.5

TABLE 3

Surge Motion

Model	Test	Significant Motion (cm) Actual	Experimental RAO	Theoretical RAO
Large Cube	LIR857	5.84	6.96	3.82
	LIR1143	9.74	9.1[illegible]	5.35
Cylinder	CIR857	6.80	6.66	5.44
	CIR1143	9.49	9.56	7.74
	CIR1429	13.90	12.87	10.61
Trapezoid	TIR857	7.93	8.09	5.03
	TIR1143	10.01	11.27	7.23
	TIR1429	15.08	16.01	10.37
Sphere	SIR857	10.15	10.89	3.35
	SIR1143	11.98	10.97	4.86
	SIR1429	10.00	12.09	5.63

TABLE 5

Heave Motion

Model	Test	Significant Motion (cm) Actual	Experimental RAO	Theoretical RAO
Large Cube	LIR857	9.91	9.10	12.39
	LIR1143	12.52	16.03	22.49
Cylinder	CIR857	9.21	11.19	17.71
	CIR1143	11.02	15.67	24.88
	CIR1429	17.61	17.95	26.33
Trapezoid	TIR867	4.66	5.90	3.52
	TIR1143	6.58	7.78	7.98
	TIR1429	10.92	10.15	10.29
Sphere	SIR857	5.59	4.50	6.06
	SIR1143	8.04	6.28	8.26
	SIR1429	9.45	7.41	8.70

TABLE 6

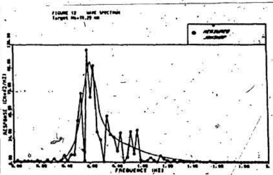

ABSTRACT

Experiments have been performed to assess the ability of linear diffraction theory to predict the motion of ice masses under wave excitation. Variables in the regular wave portion of the experiment included iceberg size and shape and wave steepness. Regular wave tests demonstrated accurate motion prediction, with best results achieved for smooth sided bodies undergoing small amplitude motion. Accuracy was lower for low frequency surge and heave resonance results, and generally for bodies with steeply sloping sides.

Irregular tests were performed to demonstrate the ability to predict motion in an irregular seaway. It was seen that by combining response amplitude operators (RAO's) with wave spectra, response spectra for individual bodies could be predicted. The predicted spectra generated using experimentally determined RAO's very accurately mirrored the ones generated by transforming irregular-wave body response data to the frequency domain. Predicted spectra generated using theoretically determined RAO's were studied as well. It was found that the accuracy of such spectra was directly tied to the accuracy of the associated RAO's.

ACKNOWLEDGEMENT

I would like to express my sincere gratitude to several individuals and groups without whom this work would have been impossible. Thanks are due to my wife Connie whose never-waning encouragement was a constant source of inspiration. My supervisor, Dr. J.H. Lever provided me with the freedom and encouragement to pursue various projects over my graduate career for which I am very grateful. Mr. Bruce Colbourne answered all my "dumb" questions concerning marine engineering and, as the other graduate students in the Ocean Engineering programme have discovered, is a veritable "graduate's consultant". Mr. Deb Sen's assistance with the theoretical analysis is gratefully acknowledged. Mike Sullivan, Howard Mesh, Lloyd Little, and Blair Wilkie displayed remarkable enthusiasm and patience during the course of the experiment.

Dr. G.R. Peters, Dean of Engineering, and Dr. D.B. Muggeridge, Chairman, Ocean Engineering Research Group, are due thanks for their support during my pursuit of this degree. The Natural Sciences and Engineering Research Council of Canada, and the Centre for Cold Ocean Resources Engineering, Dr. J. Clark, Director, have supported me financially over the past two years, for which many, many thanks are extended.

TABLE OF CONTENTS

LIST OF ILLUSTRATIONS

LIST OF ILLUSTRATIONS

Cont'd

LIST OF ILLUSTRATIONS

Cont'd

LIST OF TABLES

1.0 INTRODUCTION

Exploration and production activities related to offshore petroleum discoveries near the Grand Banks of Newfoundland have led to much concern regarding the potential impact of ice masses with drilling rigs, production platforms, etc. Work is underway to determine the loading on and deformation of offshore structures in the event of a collision (1, 2). Dynamic models have been developed to determine the extent of structural damage for a given set of input conditions (iceberg size, shape, structural geometry). The motion of the ice mass is obviously a critical variable in the whole problem, and one which has not been well understood.

Initially, iceberg impact velocities were estimated using average drift speeds calculated from hourly drilling rig observations (3, 4, 5). Recently, however, the contribution of wave forces to iceberg motion has been considered important, particularly for smaller masses. Experimental work by Lever, Reimer, and Diemand (6) suggests that the velocities of wave driven bergy bits and growlers can substantially exceed their associated drift speeds.

Sen (7) has developed a computer program based on the singularity distribution method for establishing motion response of bodies having arbitrary shape in regular waves. The response of the body is based on linearized potential flow theory, with the flow assumed inviscid, irrotational, and incompressible. The flow field is then characterized by a single-valued velocity potential composed of the incident wave potential together with the diffraction potential produced by the stationary body and six radiation potentials arising from the body's oscillatory motion about its equilibrium position. Proper matching of boundary conditions leads to the calculation of response amplitude for a unit amplitude input wave.

The foundation of the three-dimensional singularity distribution method was first established by Kim (8) and later expanded and verified (9, 10, 11, 12, 13).

Sen (7) has demonstrated the applicability of the program by performing calculations based on rectangular and cylindrical floating bodies. Comparison of his results with those of other investigators (Faltinsen) confirms the accuracy of the computations.

To handle the problem of wave induced motion in an irregular sea Lever and Sen (14) have combined the response amplitude operators calculated by Sen's computer program (7) with a Jonswap sea spectrum (15) using the well established procedures described in (16). The Jonswap spectrum was chosen as a reasonable representation of a North Atlantic wave energy distribution. The procedure followed by Lever and Sen (14) in determining the significant motions of ice masses with known RAO's in particular sea conditions is given in (16). The square of the response to a unit regular wave is multiplied by the wave energy at the corresponding frequency. The response spectrum formed by repeating this procedure over all frequencies is then integrated. Characteristic motion values, such as significant (average of highest 1/3) amplitude may be obtained from the resulting value, assuming narrow banded spectra.

The accuracy of results obtained from such a theory is governed by several items. The assumptions made in the application of linear potential flow theory are: (i) viscous effects are negligible; (ii) incident wave steepness is small; and, (iii) body motion is small. One purpose of this research is to determine how accurately the regular wave motion of small ice masses can be predicted by the theory.

The influence of fluid viscosity on wave-induced ice motion may be broken down conceptually into regions based on wavelength (λ)/body size ratio. It can be shown that this ratio is equivalent to Froude number. It is expected that for small values of the ratio ($\lambda/Lc<5.0$) the ratio of waveheight: body characteristic length will also be small, since wave steepness is practically constrained to a relatively narrow range. Milgram (17) points out that form drag forces are related to the occurrence of flow separation during motion. For small values of λ/Lc there will be insufficient time for vortices to form prior to flow reversal, and form drag forces will not present a large problem. For small bodies ($\lambda/Lc>12$), relative ice/fluid motion will be small as motion approaches that of a particle, and viscous forces will not significantly affect ice behaviour (6). Between these two regimes viscous effects may result in prediction problems. It is noted that irregular seas contain all wave frequencies so that in such seas, the influence of fluid viscosity on wave induced motion is unclear.

As wave steepness and amplitude of body motion are varied, a range of discrepancies in theoretical/experimental body motion will exist. Steeper waves have associated nonlinear effects which will tend to produce motions not accurately predicted by the linear theory.

A convenient measure of steepness is H/λ, H and λ being wave height and wavelength respectively. The entire theory is founded on the approximation that $H/\lambda << 1$, such that any parameter having a magnitude of the order $(H/\lambda)^n$, $n \geq 2$ is small enough to be negligible. This approximation, in turn, allows a convenient simplification - the dynamics of fluid motion are calculated assuming the free surface (ie. the wave profile) to be the undisturbed (ie. mean) water surface. As H/λ increases, the assumption of "smallness of steepness" is violated and the accuracy expected using linear theory is reduced.

Similarly, large motion of the body contradicts the condition implied in the linear theory wherein the radiation potentials are calculated for small motion near the equilibrium position. The most important implication of this assumption is that the wetted surface of the body is treated as a fixed quantity, equalling that of a mean wetted surface. As body motion becomes larger, changes in wetted surface become more pronounced and prediction using linear theory is less accurate. This effect will be particularly significant near regions of resonance.

In addition to the effects of wave steepness, body motion amplitude (relative to berg size), and viscosity, the shape of the icebergs is thought to affect prediction ability. Sharply cornered icebergs will tend to induce vortex formation during motion. This will lead to difficult to predict viscous effects, causing errors in prediction. In addition, steeply sloping sides, such as those observed on icebergs having considerable underwater "rams", lead to drastic changes in waterplane area as the body oscillates, again reducing prediction ability as this is not incorporated in the linear theory.

A further purpose of the research is to determine whether differences in the RAO's predicted by Sen's program and those measured experimentally lead to large errors in significant motion in irregular waves as determined by Lever and Sen's procedure (14). The effect of errors in the prediction of regular wave induced motion on corresponding irregular wave prediction, as represented by a lumped parameter such as significant motion, is studied. Also, icebergs exhibit considerable non-linear behaviour, such as body submergence and large excursions from equilibrium position during wave excitation. The ability to use linear superposition in spite of this fact will be studied.

In order to meet the objectives set forth a series of wave tank experiments have been performed. Firstly, a series of regular wave experiments have been carried out to determine the degree to which measured RAO's differ from those predicted by linear theory. Variables in the regular waves portion include frequency, wave steepness, and berg size and shape. Secondly, a series of irregular wave experiments were included. The degree to which RAO discrepancies lead to errors in signficant motion prediction was studied here.

2.0 EXPERIMENTAL PROGRAM

2.1 Ice Models and Waves

The experiments were carried out in two major groups: regular waves and irregular seas. Table 1 shows the wave characteristics associated with the regular wave experiments. The waves chosen reflect ones typically encountered on the Grand Banks of Newfoundland, and the water depth is similar to that location as well. An object, such as an iceberg, while moving through an incompressible fluid may be expected to experience forces resulting from gravity, inertia, and viscosity. In order to correctly model such a system, equality of Froude and Reynolds numbers is required. However, if the fluids used are the same in model and prototype, equality of both numbers is impossible. Froude number represents the ratio of inertial to gravitational forces, and in cases where surface waves are considered to be the predominant driving mechanism, such as the present case, this number is used as the scaling law. Froudian Scaling Laws are as follows:

$$Ls = Lm/Lp$$
$$Vm/Vp = (Ls)^{\frac{1}{2}}$$
$$Tm/Tp = (Ls)^{\frac{1}{2}}$$
$$fm/fp = (1/Ls)^{\frac{1}{2}}$$

where: Ls = Linear model scale

V = Velocity

T = Time

TABLE 1

REGULAR WAVE EXPERIMENTS

MODEL	TEST	FREQUENCY(HZ)	WAVELENGTH(M)	WAVEHEIGHT(CM)	STEEPNESS
SMALL CUBE	D557A60	.557	4.9	7.94	62
	D697A60	.697	3.2	5.74	56
	D836A60	.836	2.2	4.49	49
	D104A60	1.040	1.4	2.73	51
	D119A60	1.190	1.1	1.89	58
MEDIUM CUBE	M557A60	.557	4.9	6.60	74
	M557A50	.557	4.9	9.07	54
	M557A40	.557	4.9	10.37	47
	M697A60	.697	3.2	4.30	74
	M697A50	.697	3.2	5.61	57
	M697A40	.697	3.2	7.00	46
	M836A60	.836	2.2	5.10	43
	M836A50	.836	2.2	4.83	46
	M836A40	.836	2.2	6.50	34
	M104A60	1.040	1.4	4.30	33
	M104A50	1.040	1.4	2.79	50
	M104A40	1.040	1.4	3.30	42
	M119A60	1.190	1.1	1.83	60
	M119A50	1.190	1.1	2.10	52
	M119A40	1.190	1.1	2.50	44
	M119A20	1.190	1.1	5.41	20
LARGE CUBE	L557A40	.557	4.9	10.10	49
	L697A60	.697	3.2	6.25	51
	L836A60	.836	2.2	4.62	48
	L836A40	.836	2.2	5.80	38
	L104A60	1.040	1.4	2.24	63
	L104A40	1.040	1.4	2.90	48
	L119A60	1.190	1.1	2.54	43
	L119A40	1.190	1.1	3.54	31
CYLINDER	C557A60	.557	4.9	7.35	67
	C557A40	.557	4.9	11.30	43
	C697A60	.697	3.2	5.51	58
	C697A40	.697	3.2	8.35	38
	C836A60	.836	2.2	3.30	67
	C836A40	.836	2.2	6.97	32
	C104A60	1.040	1.4	2.58	54
	C104A40	1.040	1.4	3.70	38
	C119A60	1.190	1.1	1.70	65
	C119A40	1.190	1.1	3.11	35
TRAPEZOID	T557A60	.557	4.9	6.30	78
	T557A40	.557	4.9	11.00	45
	T697A60	.697	3.2	5.53	58
	T697A40	.697	3.2	7.83	41
	T836A60	.836	2.2	3.83	57
	T836A40	.836	2.2	5.65	39
	T104A60	1.040	1.4	2.30	61
	T104A40	1.040	1.4	3.61	39
	T119A60	1.190	1.1	2.15	51
	T119A40	1.190	1.1	2.40	46
SPHERE	S557A60	.557	4.9	8.00	61
	S697A60	.697	3.2	5.98	54
	S836A60	.836	2.2	5.22	42
	S104A60	1.040	1.4	3.42	41
	S119A60	1.190	1.1	2.56	43

f = frequency

m, p = model, prototype.

The scaling factor chosen was 70:1.

Water depth in the tank was 1.8 metres, corresponding to a prototype depth of 126 metres. The wave periods in full scale ranged from 7 to 15 seconds. The model periods corresponding to the aforementioned waves range from .837 to 1.793 seconds, ie. frequencies from .557 Hz to 1.19 Hz. The wavelengths were determined using the following equation, derived for linear waves in finite water depth.

$$L = gT^2/2\pi \ \tanh[2\pi\, d/L]$$

where: L = wavelength

g = acceleration due to gravity

T = wave period

d = water depth.

The test identifiers shown in Table 1 indicate several items. For example, test M557A60 indicates the medium cube (M), with model scale wave frequency of .557 Hz, and a target wave steepness of 60:1. The actual steepnesses measured have been included.

Figures 1-4 show the model icebergs used in the experiment. The three cubes represent full scale icebergs having masses of 1500, 12100, and 43,100 tonnes. They were chosen to investigate the effect of viscosity on motion prediction. For example, the cubes' ratio of characteristic

CUBE (3 SIZES)

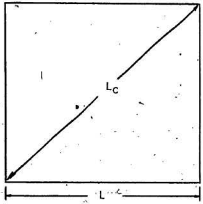

MODEL	LEN.(cm)	MASS(kg)	CHAR. LENGTH(cm)	WATERPL. AREA(cm^2)	RADIUS OF GYRATION(cm)
SMALL	17.5	4.5	24.7	306.3	7.1
MEDIUM	34.6	35.4	48.9	1197.2	14.0
LARGE	51.9	125.8	73.4	2693.6	21.2

FIGURE 1

CYLINDER

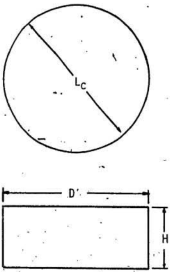

DIAMETER(cm)	HEIGHT(cm)	MASS(kg)	CHAR. LENGTH(cm)	WATERPL. AREA(cm^2)	RADIUS OF GYRATION(cm)
48.5	19.8	30.9	48.5	1847.5	13.4

FIGURE 2

TRAPEZOID

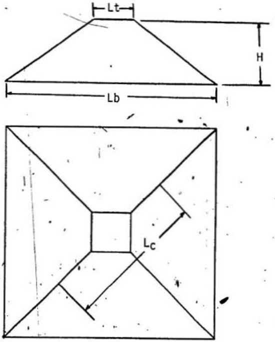

Lt(cm)	Lb(cm)	H(cm)	MASS(kg)	CHAR. LENGTH(cm)	WATERPL. AREA(cm^2)	RADIUS OF GYRATION(cm)
12.9	65.5	20.0	32.3	48.4	1171.3	15.9

FIGURE 3

SPHERE

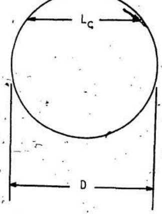

DIAMETER(cm)	MASS(kg)	CHAR. LENGTH(cm)	WATERPLANE AREA(cm^2)	RADIUS OF GYRATION(cm)
31.0	13.6	25.9	526.9	10.5

FIGURE 4

lengths is 1:2:3. As may be seen in Table 2, the ratio of wavelength to characteristic length for the small cube in 1.1 metre wavelength is very close to that for the medium cube in 2.2 metre waves and the large cube in 3.2 metre waves. These cases are essentially equivalent in terms of Froudian Scaling (excepting discrepancies arising due to corrections made to account for electronics). However, Reynolds number is directly proportional to characteristic length, and, since frictional forces are directly related to Reynolds number, the effect of viscosity will differ for these tests. The discrepancy in RAO values for tests such as these will reveal the relative importance of viscosity.

TABLE 2

RATIO OF WAVELENGTH: BERG CHARACTERISTIC LENGTH

	CHARACTERISTIC	WAVELENGTH (m)				
SHAPE	LENGTH (m)	1.100	1.429	2.229	3.171	4.700
Small Cube	.1732	6.351	8.251	12.87	18.31	27.14
Medium Cube Trapezoid Cylinder	.3386	3.249	4.220	6.583	9.365	13.88
Large Cube	.5138	2.141	2.781	4.338	6.172	9.148
Sphere	.2590	4.247	5.517	8.606	12.243	18.147

The medium sized cube, along with the "cylinder" and "trapezoid" have the same characteristic length (largest waterline dimension) and are within 13% of having the same mass. These models were chosen to represent particular commonly observed icebergs. The trapezoid was chosen to represent icebergs having a substantial underwater "ram". The cylinder was chosen to represent smoother, older icebergs. The sphere is of considerably smaller mass and represents a small, smooth bergy bit. Ballasting of this model was required to prevent rolling, and the weight added was accounted for in the theoretical calculation. It was expected that models with drastically sloping sides, such as the trapezoid and sphere, will show poorer matching than that observed with the cylinder and cubes.

The models were made from paraffin wax having a density of 870 kg/m^3. This value approximates that of iceberg ice, but impurities present lead to the values measured and reported in Figures 1-4.

The irregular sea experiments were carried out using the same models. The small and medium cubes could not be used in the irregular tests due to model rolling problems. Characteristics associated with the seas are given in Table 3. As in the regular wave tests, the test identifying code is significant. For example, test CIR1143 implies the cylinder (c) in an irregular wave train having target significant wave height of 11.43 centimetres. The choice of significant sea heights was made based on Lever and Sen's (14) use of 2, 4, 6, 8, and 10 metre full scale sea heights. Difficulties with high frequency wave board movements forced the elimination of tests corresponding to the two lowest sea states, and

IRREGULAR WAVE EXPERIMENTS

MODEL	TEST	MEASURED SIGNIFICANT WAVE HEIGHT (cm)	TARGET PEAK PERIOD (sec)	TARGET PEAK FREQUENCY (hz)
LARGE CUBE	LIR857	14.2	1.30	.77
	LIR1143	19.9	1.50	.67
CYLINDER	CIR857	12.3	1.30	.77
	CIR1143	16.3	1.50	.67
	CIR1429	21.8	1.67	.60
TRAPEZOID	TIR857	13.4	1.30	.77
	TIR1143	18.6	1.50	.67
	TIR1429	22.6	1.67	.60
SPHERE	SIR857	11.7	1.30	.77
	SIR1143	15.9	1.50	.67
	SIR1429	17.7	1.67	.60

TABLE 3

the 6, 8, and 10 metre full scale cases correspond to model Hs's of 8.57 cm, 11.43 cm, and 14.29 cm. As with Lever and Sen (14), a few simplifying assumptions were made to reduce the characterization of the sea spectrum to a single variable: significant wave height. The relationships used to generate the irregular sea were chosen to produce waves expected to be common in Canadian Atlantic waters, particularly near the Grand Banks of Newfoundland (15). The relationship between peak period Tp and significant wave height Hs is as follows:

$$Tp = 4.43\ Hs^{\frac{1}{2}}$$

The peak enhancement factor γ was given a value of 2.2. The relationship between peak frequency fo and peak period is:

$$fo = 1/Tp$$

The spectrum is given by the equation:

$$Sw(f) = A/f^5 \exp(-B/f^4)\ \gamma^a$$

where $a = \exp[-(f-fo)^2/(2\sigma^2 fo^2)]$

$\sigma = 0.07$ for $f \le fo$

$\sigma = 0.09$ for $f > fo$

$A = 5\ Hs^2 fo^4/(16\ \gamma^{1/3})$

$B = 5\ fo^4/4$

2.2 Experimental Facility and Equipment

Tests were carried out at the wave tank located in the fluids laboratory at Memorial (Figure 5). The tank has measurements of 58.27 m x 4.57 m x 3.04 m and is constructed of reinforced concrete. Waves are created by

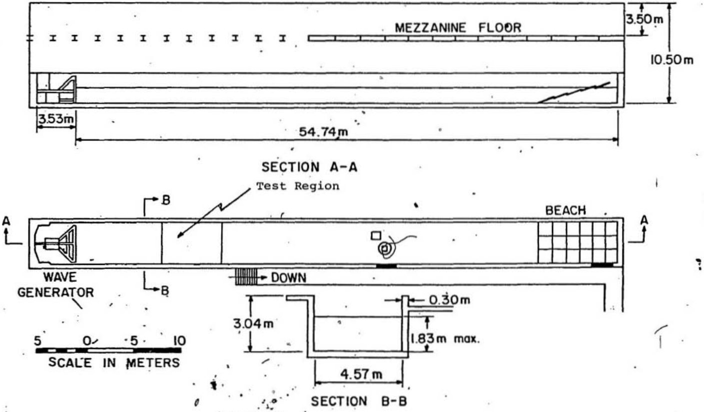

FIGURE 5 Elevation and Plan Views of Wave Flume.

the movement of a piston type aluminum board. The board is driven by an M.T.S. hydraulic ram, the motion of which is controlled by a closed loop wave generator. The wave generator sends a signal to the ram, causing it to move. The position of the board is measured and an indication of same is relayed to the generator. The desired and actual positions of the board are compared and a signal is sent to compensate for any deviation. This correcting procedure is a high speed process and occurs continuously during wave board operation.

An energy absorbing beach is located at the opposite end of the tank, the main duty of which is to prevent the reflection of significant waves back toward the wave board. Murray and Muggeridge (18) report reflection coefficients less than 10% for the beach, where reflection coefficient is defined as the ratio of reflected wave height: incident wave height. Further technical information concerning the wave tank is seen in (18).

Wave motion was analysed with the aid of resistance type wave probes, data obtained being stored on Hewlett Packard cartridges at a frequency of 10 Hz. Probe accuracy was checked daily by a series of static tests. Wave information was gathered and plotted for each test run, with the probes located near the center of the test region (Figure 6).

The equipment used to provide motion information associated with the moving bergs is known as the Selspot System. The system consists of two cameras capable of sensing the position of infrared light emitting diodes, at a frequency of 19.5 Hz, together with electronics enabling the transformation of the sensed positions to a digital form. Software has

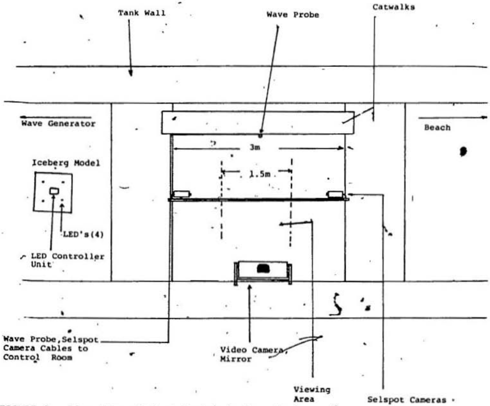

FIGURE 6 Plan View of Test Region in Wave Tank

been developed to take the raw digitized position information and store it on personal computer floppy disks. Once the data was stored on disks, manipulation was handled by programs developed for a Personal Computer. A six-degree of freedom time series was generated describing surge, sway, heave, pitch, yaw, and roll motions. Body motions are defined relative to the direction of wave propagation. For example, surge motion is parallel to the wave tank walls, with sway motion perpendicular to surge. The software was set up to determine motions within this frame of reference despite the inevitable yawing motion of the bodies and associated horizontal rotation of the LEDS. Additional programs have been developed to further manipulate the data and produce plots.

Problems previously encountered due to reflection of light from the water surface have been averted by mounting the LEDs atop thin shafts of wood inserted in the iceberg models. The weight and moment of inertia of the wood/battery/remote LED controller were small compared to those of the ice models. For the smaller models (small cube, sphere) the theoretical predictions accounted for the equipment. The effect of the additional weight and moment of inertia was checked for one of the larger models and found to be negligible and was therefore neglected for others.

A complete description of the Selspot System is available in Reference (19).

2.3 Confirmation Tests

A series of tests were run to confirm the accuracy of the Selspot motion measuring system. Initially, a series of static tests were run. The LED's were mounted on a piece of wood which was placed on a ladder supported by catwalks spanning the wave tank. Information was gathered to identify the initial position of the wood. Next the system was translated and rotated by known amounts in all six degrees of freedom and more data was gathered to define the new position. Results of the static tests are shown in Table 4.

It should be kept in mind that a graduated ruler was used to give the system its initial surge and sway, so that those results cannot be expected to be as accurate as those in which precisely angled blocks produced angular movements.

With this in mind the results of the confirmation tests lead to the conclusion that in most cases the system is accurate to within 5%.

In order to ensure that the system was functioning properly in terms of tracking moving bodies a dynamic test was conducted. This test consisted of mounting the previously described wood on cables, and supporting it in the viewing area in the configuration of a simple pendulum. The mass of the board and electronics was measured as 0.752 kg, and the length of the cable was 1.21 metres. For a simple pendulum, (small ocsillations) the period of oscillation is

$$T = 2\pi \quad (l/g)^{\frac{1}{2}}$$

$$= 2\pi \quad (1.21/9.81)^{\frac{1}{2}} = 2.21 \text{ seconds.}$$

ACTUAL MEASUREMENT	MEASURED MOVEMENT	%ERROR
-15° Roll	-14.98	0.12
	-14.72	1.87
15° Roll	14.29	4.71
	13.94	7.07
-15° Pitch	-15.15	1.02
	-14.18	5.44
15° Pitch	13.64	9.01
	14.14	5.73
-15° Yaw	-15.51	3.41
	-14.97	0.20
15° Yaw	14.99	0.04
	15.40	2.67
10 cm Surge	10.97	9.73
	9.93	0.70
-10 cm Surge	-8.94	10.53
-5 cm Sway	-4.71	5.77
	-4.81	3.80
5 cm Sway	5.67	13.54
4.5 cm Heave	4.57	1.69
8.5 cm Heave	8.57	0.82

TABLE 4

The system was given an initial surge amplitude of approximately 10 centimetres. During the test it was observed that surge motion decreased, sway motion gradually increased, and the system rotated about a vertical axis. The results of the dynamic test have been plotted and are shown in Figures 7 and 8.

It is noted that: period of oscillation is measured to be 2.1 seconds; surge and pitch amplitudes decrease with time; sway and roll amplitudes increase with time; a gradual rotation about the z (vertical) axis is noted. In general the plotted results correspond to what was observed during the test.

The static and dynamic tests have shown that the Selspot system as set up can be relied upon to measure motion accurately.

2.4 Methodology

The analysis of the regular waves portion of the experiment was relatively straight-forward. Sen's program was run for all models considered. It has been shown (7) that improved results may be obtained from the program as a larger number of panels are used to discretize the body. Sen (7) reports that 48 panels are sufficient to obtain accurate results for a floating box. In this work at least 80 panels have been used to describe the models. The program provided RAO's for the models as a function of wave frequency. Iceberg motion information measured during the regular wave tests was compared with wave data to provide RAO points. Motion values were taken by averaging several cycles of response

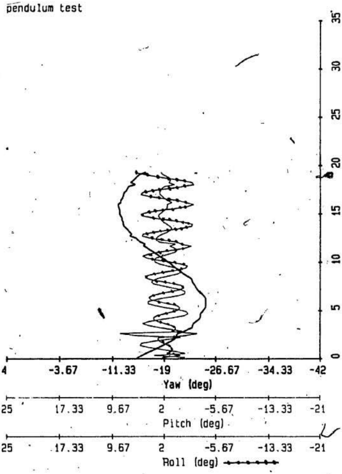
pendulum test
Seconds
0
5
10
15
20
25
30
35
4
-3.67
-11.33
-19
-26.67
-34.33
-42
Yaw (deg)
25
17.33
9.67
2
-5.67
-13.33
-21
Pitch (deg)
25
17.33
9.67
2
-5.67
-13.33
-21
Roll (deg)

FIGURE 7

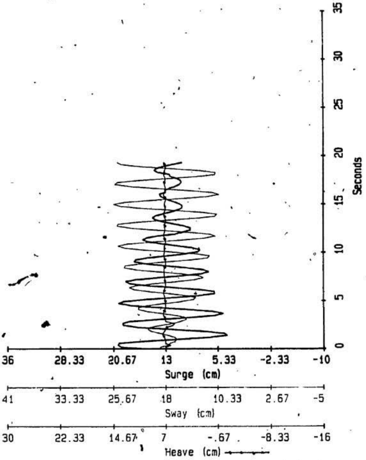

Seconds
0
5
10
15
20
25
30
35
36
28.33
20.67
13
5.33
-2.33
-10
Surge (cm)
41
33.33
25.67
18
10.33
2.67
-5
Sway (cm)
30
22.33
14.67
7
-.67
-8.33
-16
Heave (cm)

FIGURE 8

data. Even in cases where some residual wave action was evident it was found that the standard deviation of a series of regular wave results was in the order of a few millimetres. After each series of wave frequency tests had been completed, RAO versus frequency curves were plotted and compared to those generated theoretically. To evaluate the relative performance of different bodies an error indicator has been defined as follows: Error = ((Experimental result - theoretical result)/theoretical result) x 100.0. Comparison of the average error for all tests on the models is then helpful in analysis. Unfortunately, the steepness range was restricted to 40:1 - 60:1, as the berg models tended to roll in steeper waves.

The irregular wave experiments involved somewhat more analysis to provide informative results. The Jonswap spectrum served as the basis for irregular wave generation. The spectrum was transformed to the time domain and the corresponding signal was sent to the wave board. Because of the rather small size of the viewing area available using the selspot system it was necessary to carry out the irregular sea tests in segments.

The total time period associated with each spectrum was 64 seconds, but the bergs typically passed through the viewing area in 10-15 seconds. As a result the waves were sent in four sixteen second segments with the wave board paused in between. A signal was sent to the control room when the first wave hit a model berg so as to coordinate wave/response data sets.

The raw results of these procedures were two sets of time series: the wave amplitude measured by the wave probe, and the model response measured by the Selspot system. To evaluate Lever and Sen's procedure it was necessary to transform both these time series to the frequency domain. This was accomplished using an algorithm based on material in reference (20). The Fourier points may be calculated using the following equation:

$$a_0 = \bar{x}$$

$$a_{n/2} = \Sigma -1^t \, x_t / N$$

$$a_p = 2[\, \Sigma x_t \cos(2\pi \, pt/N)]/N \quad p = 1, 2 \ldots N/2-1$$

$$b_p = 2[\, \Sigma x_t \sin(2\pi \, pt/N)]/N$$

where N = number of timeseries points

x_t = amplitude of t^{th} time pt.

a_p, b_p = real and imaginary values of the Fourier transform.

The data was then transformed into a magnitude density spectrum using the following equation:

$$S(f) = \frac{a^2+b^2}{\Delta f}$$

where Δf = frequency increment.

The result of this procedure was a wave spectrum (examples shown together with target Jonswap spectra in Figures (9-12)) as well as a response spectrum for each irregular test. Results were considered for heave as well as surge motion. Lever and Sen's method, as described earlier, involves the combining of wave spectra with RAO's to produce response spectra. To evaluate this method, then, the wave spectra generated here were combined with both the theoretical RAO's generated by Sen's program, and the experimentally determined RAO's to produce two predicted response spectra. These spectra were compared with the response spectra determined by transforming the Selspot model response time series. In comparing the spectra, shape, peak location, and peak magnitude were considered. Although varying slightly for the different test runs, approximately 780 data points were used to generate spectra having frequency resolution of 0.03 Hz. No spectral smoothing was carried out. Also, since the system noted the initial position of the body and reported motions with respect to it, no significant mean value was present in the data. Since the sampling rate was 19.5 Hz, the Nyquist frequency was 9.75 Hz, an order-of magnitude higher than the expected peak frequencies. As a result of this, aliasing, or the inability to distinguish frequencies higher than the Nyquist frequency from lower ones, should not be a problem. The repeated matching of the target and actual peak frequencies confirms good spectral stability.

Finally, all spectra were integrated and the signficant motions determined in order to discover whether spectral discrepancies led to large errors in predicting characteristic motions.

It was expected that the predicted spectra formed using measured RAO's would match well with the actual ones, thereby confirming the use of the linear superposition. The comparison of the actual spectra with the predicted ones generated using theoretical RAO's was included to discover to what extent discrepancies in RAO's affect irregular sea predictions.

FIGURE 9 WAVE SPECTRUM
Target Hs=8.57 cm
Measured Hs=11.57 cm

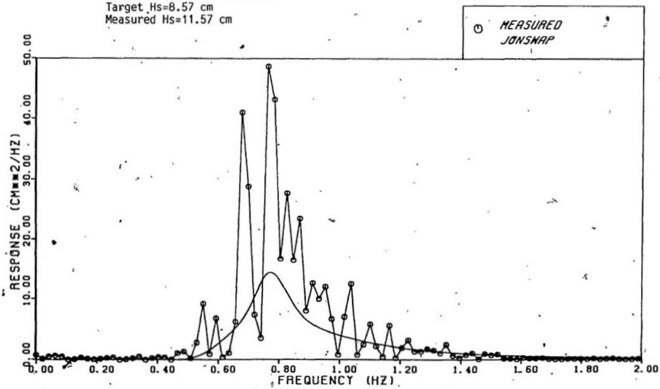

FIGURE 10 WAVE SPECTRUM
Target Hs=11.43 cm
Measured Hs= 16.3 cm

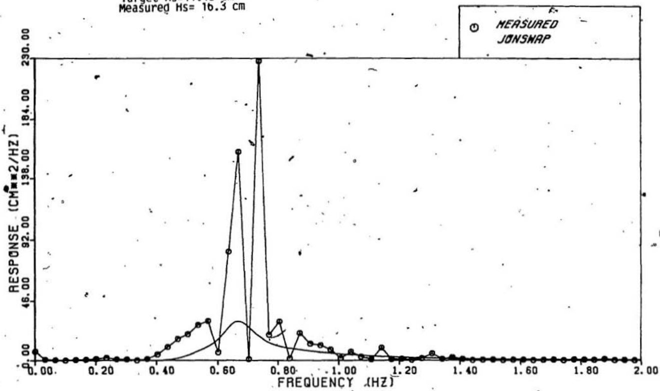

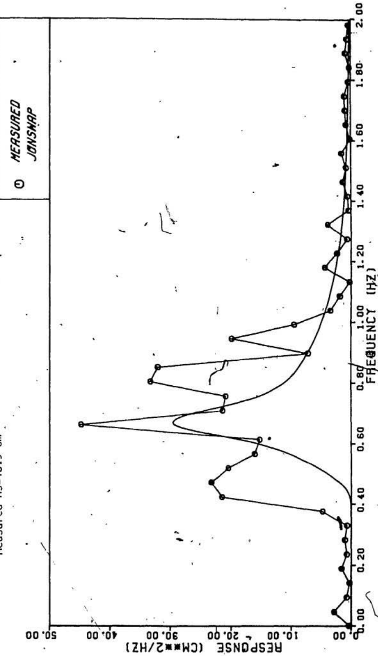

FIGURE 11 WAVE SPECTRUM
Target Hs= 11.43 cm
Measured Hs=15.9 cm

FIGURE 12 WAVE SPECTRUM
Target Hs=14.29 cm
Measured Hs=17.7 cm

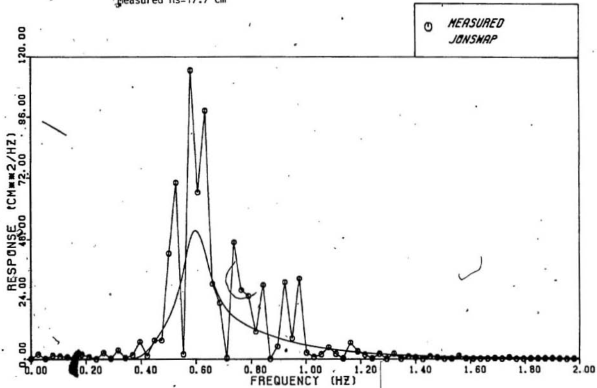

3.0 DISCUSSION OF RESULTS

In this section a discussion of the results of the test program will be presented. Firstly, the regular waves portion will be considered. Particular attention will be given to trends noted regarding relative accuracy of experimental results compared to theoretical prediction as size and shape of berg model and wave steepness are varied. Secondly, the irregular sea portion of the experiment is discussed, with an eye to the ability of theoretical predictions to match experimental results, in terms of predicted and experimental response spectra. A summary of regular wave results appears in Appendix 1. Timeseries of berg response and wave amplitude appear in Appendices 2 and 3, respectively.

3.1 Regular Waves

3.1.1 Surge Results

3.1.1.1 Small Cube

A plot showing the values of surge Response Amplitude Operator (RAO) for the small cube versus regular wave frequency is given in Figure (13). It is noted that a substantial peak occurs in the theoretical response plot at the frequency value 0.697 Hz. The existence of such a predicted peak is fairly common and may be linked to the predicted pitch response at the same frequency (see Figure (14)). The frequency location of a peak in a surge RAO curve will coincide with the location of pitch resonance whenever the body rotates about a point other than the body's center of gravity (CG). All motions (both predicted and measured) have been determined here for the CG, so that if, as is assumed in linear diffraction theory, pitch motion occurs about the centroid of the waterplane, pitch resonance and surge peaks will coincide. The experimental results, however, did not reflect the peak, with the surge values showing a gradual climb from high frequency to low frequency waves. That is, actual rotation occurs about a point closer to the CG. For a large portion of the frequency range it was seen that the theory underpredicted the experimental values.

3.1.1.2 Medium Cube

Sixteen tests were run using this model, as it was chosen to form the basis of the wave steepness study. Surge RAO's for this model are shown in Figure (15). For the high frequency range of tests, the steeper waves (40:1, 50:1), as expected, led to poorer matching of experimental data to theoretical prediction, with larger surge response in steeper waves. This is caused by a breakdown in linear theory with increasingly steep waves. In the lower frequency range, the trend for increasing steepness was not as clearly demonstrated. Problems with model rolling prevented the use of waves having steepness greater than 40:1.

Another interesting trend may be seen in these tests. The theory matches the experiment more closely in the high frequency region than at low frequencies. This may be explained in terms of motion amplitude. In the higher frequency cases, absolute surge amplitude is in the order of 5% of the length of the model. In the lower frequency area, motion is of the order of 18% of cube length. One of the assumptions of the linear theory used to predict the motion was that motion amplitude would be small. As the overall value of amplitude becomes greater, the linear theory can be less expected to mirror experimental results. This trend can be clearly seen in this series of tests. An alternative explanation for this behavior lies in the fact that the higher frequency waves (lower wavelength (λ)/Lc) would result in a lower viscosity induced error (17).

The average discrepancy (((experimental - theoretical) /theoretical) x 100) for the surge results of 60:1 tests on the medium cube (37.4%) was considerably less than for that of the small cube (99.6%). This could be explained using the same logic as in the previous paragraph. That is, average motion amplitude relative to model size is much greater in the small cube tests, therefore, theory is expected to be less accurate. Additionally, errors due to viscous effects are expected to be greater for the smaller cube, contributing to the larger average discrepancy. This may be demonstrated by noting that Reynold's number is directly tied to berg size, with relative viscous force magnitudes greater for smaller objects. Since the theory assumes inviscid conditions, errors are expected to be larger for the small cube.

It is observed here, as in those tests for the small cube, that in the majority of cases the theory underpredicts the experimental amplitude. It is noted that no peaks occured in the predicted surge RAO curves, as pitch resonance lies outside the test frequency range (Figure 16).

3.1.1.3 Large Cube

The average discrepancy in the surge results for the 60:1 tests using this model was 36.0%; only slightly lower than for those using the medium cube, but considerably lower than for the small cube.

In every case for this model the theoretical results underpredicted the experimental values (see Figure (17)).

Tests at different steepnesses were carried out at only three frequencies and there was no noticeable trend with respect to the relative magnitudes of discrepancy.

As in the cases of the other cubic models, it was again noted that theoretical results matched experimental ones more closely at higher frequencies than at lower values.

The model cubes provide some interesting results in terms of the effects of viscosity and body motion amplitude on prediction ability. The ratio of the lengths of the three cubes is very close to 1:2:3. Tests have been run at wavelengths 1.1 m, 2.2 m, and 3.2 m, or close to 1:2:3. These tests, in terms of Froudian scaling, are similar. However, Reynold's number increased with berg size. It may be assumed, then, that any differences in the relative discrepancies for these tests were caused by differing viscous effects. The surge discrepancies for the three tests (small cube - 1.1m, medium cube - 2.2m, large cube - 3.2m) are 79%, 24%, and 32%. This is generally as would be expected, since the smallest cube would be expected to have the largest viscosity - induced error. Another series of tests were run at wavelengths of 1.4 m, 3.2 m, and 4.9 m, again close to 1:2:3. The surge discrepancies for these tests were 108%, 93%, and 59%. The trend for this series is similar to the previous one, indicating that viscosity may be a significant variable in terms of surge motion.

The ratios of surge motion: particle motion (as indicated by wave height) have been plotted against non-dimensional wavelength (Figure 25). This plot clearly shows the three regimes of motion (non-particle-like (wavelength (λ)/Lc<5), transition (5< λ/Lc<12), and particle-like (λ/Lc>12)) described by Lever et al (6). It has been postulated that if viscosity is to lead to a problem it will do so in the transition range between non-particle and particle motion. In Figure 26 the ratio of experimental to predicted RAO has been plotted against non-dimensional wavelength. There is a general trend for theory to underpredict surge motion in the transition regime.

The effect of body motion amplitude may be seen in Figure 27. Here the ratio experimental/theoretical RAO has been plotted against non-dimensional motion amplitude. There is a trend away from the value of 1 as motion amplitude increases, as would be expected since the linear theory assumes small amplitude motion. Unfortunately, the effects of non-dimensional wavelength and motion amplitude cannot be separated completely, since larger motions occur for larger λ/Lc.

3.1.1.4 Cylinder

The cylindrical model, having similar characteristic length and mass as the medium cube, may be used together with the trapezoid and sphere to provide a basis for the study of the effect of shape on the ability to predict berg motion.

The average discrepancy for surge results at steepness 60:1 (22.5%) was approximately 40% less than for corresponding tests on the medium cube. This may be explained by noting that during the experimental runs, all the models experienced some yaw motion. Since the theoretical predictions assume no such motion, this leads to an error in cube surge motion prediction, as the wave front impinges on a body whose geometry varies with time. However, in the case of the cylinder, this yawing motion would introduce no error, as no change in geometry is produced by motion about the vertical axis.

Experiments were run at two different steepnesses for this model. Overall, there was no significant difference in the average discrepancies for the two steepnesses (see Figure (19)).

It is again observed that the theoretical results match the experimental data more closely for the higher frequency range, and in the great majority of cases, surge motion is underpredicted by the theory. It is encouraging to note that a theoretically predicted peak in the RAO curve at 0.836 Hz is confirmed by the 60:1 experimental result. This peak is related to a peak in pitch response (Figure (20)) at the same frequency. The surge peak did not occur in the 40:1 tests, and this is due to the lack of pitch resonance during this test run. Resonance is a sensitive phenomena and is apparently influenced by wave steepness.

3.1.1.5 Trapezoid

This model, having similar size and characteristic length as the cylinder and medium cube, provides a good basis for the study of shape effect.

The average discrepancy in surge RAO for trapezoid tests run at (60:1) steepness (72.6%) is approximately 90% greater than for the medium cube and 220% greater than for the cylinder. The generally poor matching observed using this model (see Figure (21)) may be explained by comparing its geometry with those of the cylinder and cube. The sloping sides of the trapezoid lead to a drastic change in underwater volume and waterplane area as the body undergoes changes in draft associated with its motion. These drastic changes are not accounted for in the linear theory, and as a result, calculations of added mass and force will not reflect experimental conditions. In addition, prediction difficulties are expected with this model as yaw motion occurs.

It is noted that all experimental results in this case were underpredicted by the theory.

No trends were evident in this test series with respect to wave steepness or low versus high frequency relative discrepancies.

An observed peak in surge again was found to agree with the experimental pitch resonance frequency, with the peak being more pronounced at the lower wave steepness.

3.1.1.6 Sphere

Surge RAO values for the sphere are shown in Figure (23). This model had a considerably lower mass and characteristic length than the other bodies used to study shape effect. Nevertheless, it is thought that results might help to confirm conclusions regarding this effect.

The average value of discrepancy in surge RAO is much higher (140%) than for any of the other bodies. This may be explained in exactly the same way as for the trapezoid. That is, the high degree of variability in underwater geometry due to body motion leads to large discrepancies between experiment and theory.

Underprediction of surge values was again noted in the tests using this model, but no trend was observed relating discrepancy to frequency.

Pitch resonance was not predicted for the sphere, but the phenomena was observed experimentally at .697 Hz. An associated surge peak occured at the same frequency. The experimental pitch/resonance may have been caused by irregularities in model shape associated with the mounted electronics or by oscillating moments induced by viscous shear forces. Neither of these effects are included in the prediction technique.

FIGURE 13

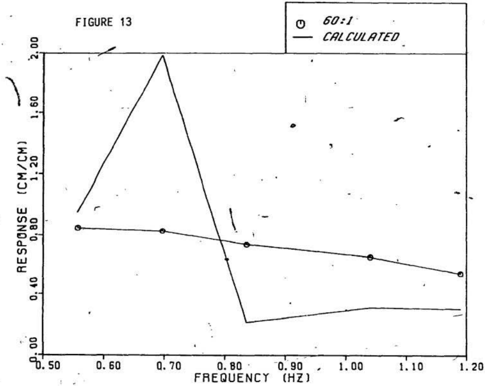

SMALL CUBE...SURGE RESPONSE...REG. WAVES

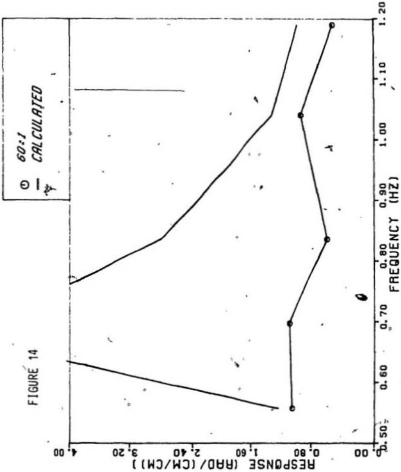

FIGURE 14

SMALL CUBE...PITCH RESP....REG. WAVES

FIGURE 15

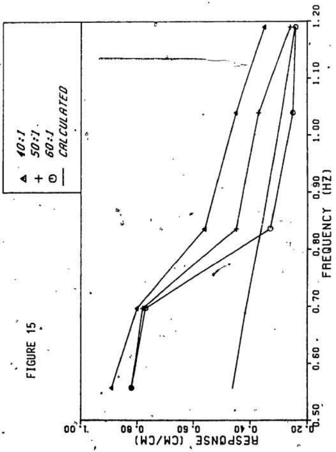

MED. CUBE... SURGE RESP.... REG. WAVES

FIGURE 16

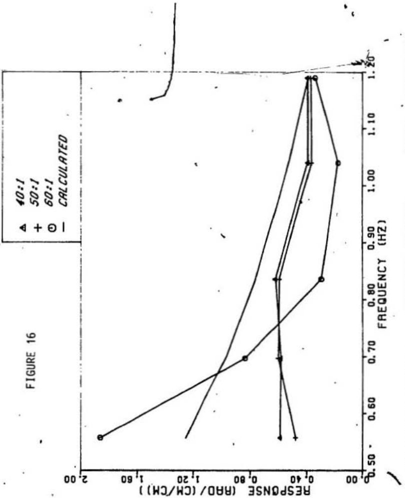

MEDIUM CUBE...PITCH RESP....REG. WAVES

FIGURE 17

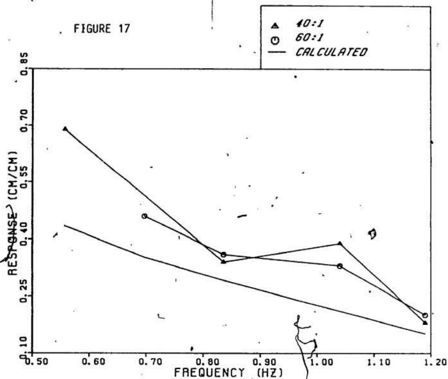

LAR. CUBE...SURGE RESP...REG. WAVES

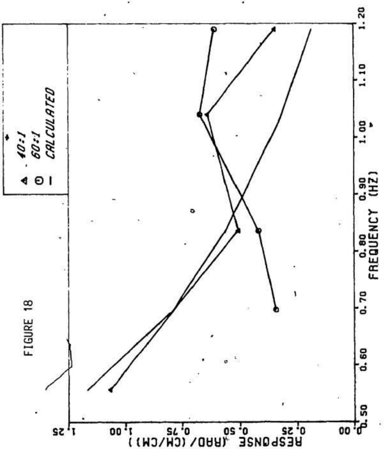

FIGURE 18

LARGE CUBE...PITCH RESP....REG. WAVES

FIGURE 19

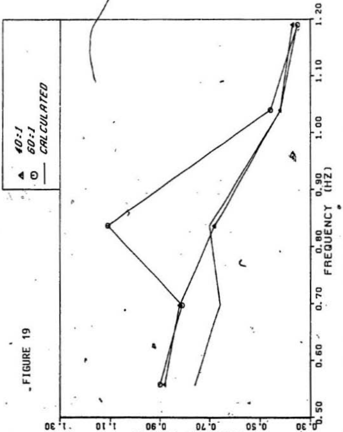

CYLINDER... SURGE RESP.... REG. WAVES

FIGURE 20

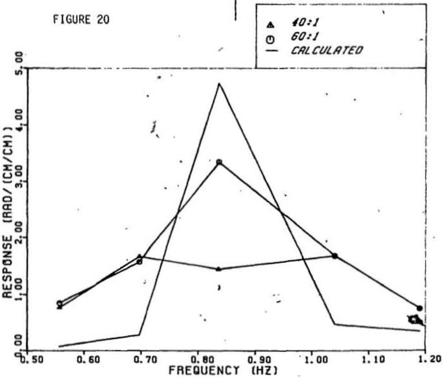

CYLINDER...PITCH RESP....REG. WAVES

FIGURE 21

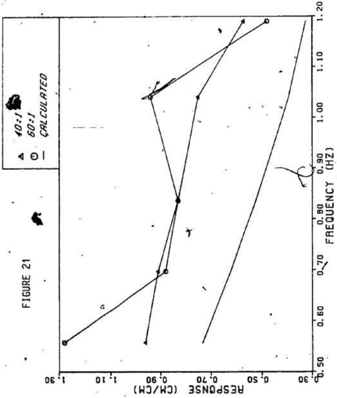

TRAPEZOID... SURGE RESP.... REG. WAVES

FIGURE 22

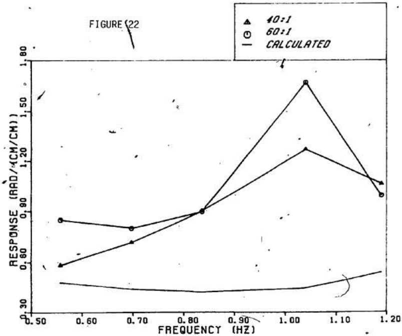

TRAPEZOID...PITCH RESP....REG. WAVES

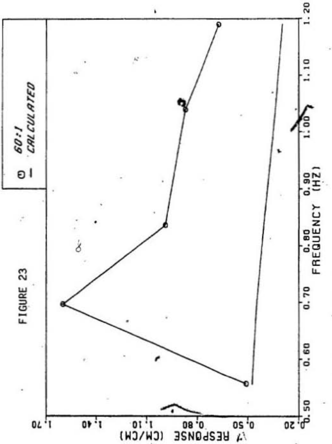

FIGURE 23

SPHERE... SURGE RESPONSE... REG. WAVES

FIGURE 24

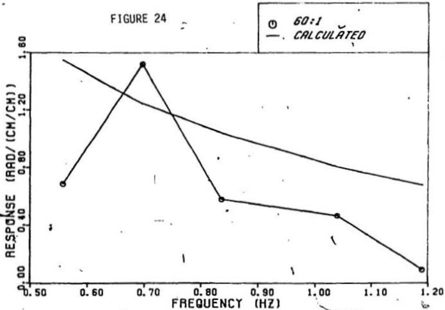

SPHERE...PITCH RESP....REG. WAVES

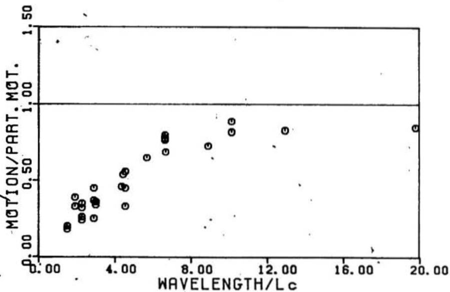

FIGURE 25 Surge motion/particle motion vs. Non-dimensional wavelength (All cubes)

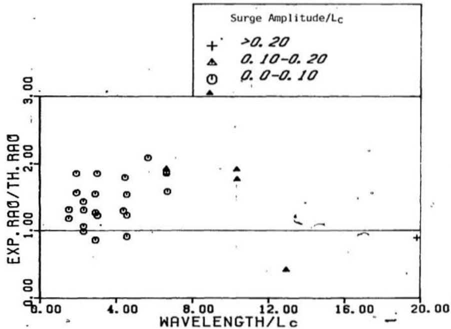

FIGURE 26 Experimental RAO/Theoretical RAO vs. Non-dimensional wavelength (Three categories of non-dimensional surge amplitude) (All Cubes)

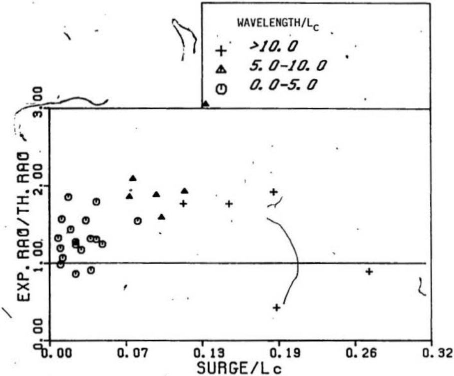

FIGURE 27 Experimental RAO/Theoretical RAO vs. Non-dimensional Surge motion (Three categories of non-dimensional wavelength) (All cubes)

3.1.2 Heave Results

3.1.2.1 Small Cube

An approximation to the natural heaving frequency for a cube can be determined as follows:

$$F = (M+M_a)\ddot{x}$$

$$F_g - F_b = (M+M_a)\ddot{x}$$

$$P_i g l^3 - P_w g (.875\ l+x) l^2 = (P_i l^3 + M_a)\ddot{x}$$

where P_i = density of ice

P_w = density of water

F_g = gravitational force

F_b = buoyant force

l = length of any side of cube .

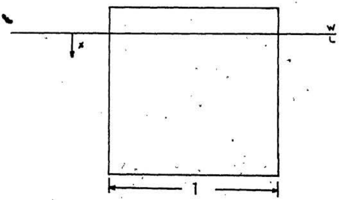

g = acceleration due to gravity

x = displacement from position of static equlibrim

M = mass of body

M_a = added mass associated with body

f = frequency

t = time

Note: P_i/P_w = .875

assuming Ma = 0.7 M = $.7P_i l^3$ (from linear theory of Sen)

$P_i g l^3 - P_w g\,(.875\,l+x)l^2 = (1.7\,P_i l^3)\ddot{x}$

dividing by Pw

$P_i/P_w\,gl^3 - gl^2(.875\,l+x) = 1.7\,P_i/P_w\,l^3\ddot{x}$

$.875\,gl^3 - .875\,gl^3 - gl^2x = 1.7(.875)l^3\ddot{x}$

The natural frequency for the cube may then be determined as follows:

$fn = (.16705/l)^{\frac{1}{2}}$

for the small cube, l = .175 metres;

fn = .97702 sec^{-1}.

It is noted that this approximation neglects the effect of damping and the dependence of added mass on frequency.

This resonant frequency is clearly shown by the theoretical results for the small cube model (refer Figure (28)). The experimental results closely match theoretical values at lower frequencies where berg motion approaches that of a particle (ie. Heave/Wv Ht = 1.0). However, there exists a wide disparity in those regions close to resonance. The experimental results show a peak at a value of 0.836 Hz, slightly lower than that predicted by theory. One explanation is that actual added mass in heave may be greater than 0.7m. It is not expected that experimental results and predicted values will closely mirror one another in the resonance region, since complete body submergence, which was in fact observed during the experiment, cannot be accounted for by linear theory. In addition, the large magnitude of body motion in the resonance region contributes to poor experimental/theoretical matching both by violating the small motion assumption and by increasing viscous damping.

It is interesting to note that contrasting the surge results, experimental heave values show that the theory overpredicts the heave amplitude. It is postulated that viscous drag, which is not considered in the theoretical calculation, accounts for the experimental heave values being consistently lower than those predicted.

3.1.2.2 Medium Cube

Values of RAO plotted against wave frequency are shown in Figure (29). The average value of medium cube heave RAO discrepancy for the 60:1 steepness waves (42%) is greater than the average for the small cube (31%). This is interesting in that it represents the reverse trend than was displayed by surge results.

The natural frequency for this cube may be approximated, as before, as .70 Hz. This value is very accurately matched by experimental results. However, the values of the RAO's in this frequency region show much greater discrepancy between theory and experiment than at higher and lower frequency values. Again, it is seen that linear theory significantly overpredicts resonant heave amplitudes.

These results display some interesting trends with respect to wave steepness as well. At non-resonance frequencies, there was no significant difference from steepest to shallowest wave. However, the steeper wave results appear to more closely approximate predicted values in the resonance range than do the shallower ones.

Two trends observed in the small cube results are repeated using this model: heave motion is tending to an RAO value of 1 for lower frequencies, representing particle motion, and the theory has consistently overpredicted experimental results.

3.1.2.3 Large Cube

The average of the 60:1 steepness test heave RAO discrepancies for the large cube (187%) is greater again than for the medium cube, continuing the trend observed between small and medium cubes. However, this result has been biassed by the high frequency heave RAO results. Large discrepancies were determined between the experimental and theoretical results using the method previously mentioned (% discrepancy = [experimental-theoretical/theoretical] x 100). In fact, however the absolute values were quite close to one another, and the large value of discrepancy appeared as a result of the relatively small values of RAO (Refer Figure (30)). Neglecting the large cube high frequency points, there seems to be only a slight trend in heave results from the small to the medium and large cube, with discrepancies seen to gradually increase with an increase in cube size.

There was no trend with respect to wave steepness effects and heave results for this model.

The natural frequency for this cube may be approximated as 0.56 Hz, and this value was observable both in theoretical and experimental results.

Several trends previously noted were repeated for this model. For most cases the heave response was over-predicted by the theory. Matching was seen to be much better in regions away from the natural frequency of the body than in areas near resonance, where theory significantly overpredicts heave motion.

In the section discussing surge results two different cases of similar (Froudian) tests were described. It was shown that surge discrepancies for the tests in question showed a reducing trend for the small to large cubes. The heave results of the same tests will now be discussed. The heave discrepancies for the first series were 46%, 60% and 18%. The discrepancies for the second series were 94%, 26% and 31%. There seems to be a similar trend here with discrepancy getting smaller with increasing model size. This is as expected, since increasing model scale reduces the magnitude of viscous forces relative to inertial ones. Since the potential flow theory used neglects viscosity entirely, predictions should improve with increasing model scale.

Similar plots have been generated for the cubes' heave results as were done for surge. In Figure 34 the ratio of heave motion: particle motion has been plotted against non dimensional wavelength. Once again the regimes described by Lever et al (6) are clearly shown. The natural frequency (heave) for the cubes, if non-dimensionalized as wavelength/characteristic length, is 6.67. This value is accurately seen as a peak in the data in Figure 34. For the region of non-dimensional wavelength 0-5, the motion is clearly non-particle like. For wavelengths greater than 10, the motion is particle-like. In Figure 35 a measure of heave error is shown plotted against non-dimensional wavelength. The high values shown at the low wavelength end of the scale reflect the very small high frequency heave motions for the large cube discussed previously. Neglecting these points, the general trend seems to be values close to 1 for Experimental /Theoretical Heave RAO for values of Wavelength/Lc less than 4 and greater than 8, with more discrepancy existing in the transition region of 4-8. This is as was expected, since, as was discussed in the introduction, viscosity will not be a problem for large or small values of wavelength/Lc, but may lead to some difficulties in the mid-range region. The existence of a clear trend in heave results, which was not as evident in the surge results, leads to the conclusion that viscosity plays more of a role in heave prediction error than in surge results.

In Figure 36 the same indicator of prediction error has been plotted against non-dimensional heave motion. In the surge results there was a trend toward poorer prediction as the amplitude of body motion increased, but no such trend is evident in the heave results. As mentioned previously, non-dimensional motion and wavelength are not entirely independent parameters. Good agreement for large heave motion is probably a result of such motion occuring at large λ/Lc.

3.1.2.4 Cylinder

The average discrepancy in cylinder heave RAO values for 60:1 steepness tests (27%) was approximately 35% lower than that for the medium sized cube. This improvement in prediction could be due to the effect of yaw motion on the cube. Yaw motion occured in just about all test runs, but such motion would introduce no discrepancy for this particular model (cylinder), whereas changes in underwater geometry relative to direction of wave front movement may affect cube motion.

The resonant frequency, as predicted by Sen's theoretical calculation, was accurately matched by the experimental results (Refer Figure (31)).

Matching was seen to be much better in the range away from the resonant frequency.

In all cases the experimental results were overpredicted by theory.

At lower frequencies the value of the RAO tended to a value of one.

No observable trend was seen with respect to wave steepness.

3.1.2.5 Trapezoid

The average discrepancy for heave RAO for 60:1 steepness tests (155%) for this model was 474% greater than for the cylinder and 278% greater than for the medium cube. The reason for the overall poor matching observed with this model can be traced to its sloping sides. As was described in the section discussing surge results, the underwater geometry of this model changes much more significantly than does the geometry of the cylinder or the cube under the action of the oscillatory motion. The restoring forces felt by this model are thus highly non-linear in nature and as a result motion is not expected to be accurately predicted by the theory.

In all but one of the frequencies tested, this model showed slightly better matching for the shallower than the steeper wave tests (Ref to Figure (32)).

It is interesting to note that, contrasting the previously discussed models, in most frequency ranges for this model, heave is underpredicted by theory. Again, this is probably due to the nonlinearity introduced by the changing underwater geometry.

3.1.2.6 Sphere

The average discrepancy value for this model (238%) was even greater than for the trapezoid. However, this average value was based largely on a high frequency point with a very low predicted heave value. Nevertheless, this model showed generally poor performance overall, failing to indicate the predicted resonance region. In more frequency ranges than not, theory underpredicted the experimental values.

The generally poor matching observed using this model can be explained in a similar manner as was the trapezoid. That is, large changes in underwater geometry as a function of body motion lead to difficult to account for non-linear restoring forces.

FIGURE 28

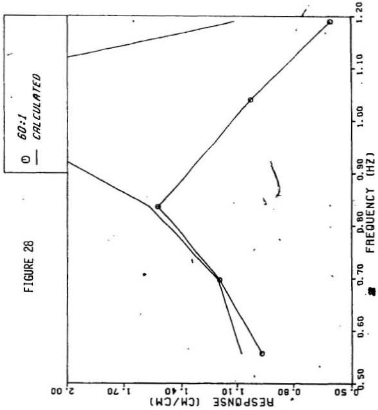

SMALL CUBE...HEAVE RESP....REG. WAVES

FIGURE 29

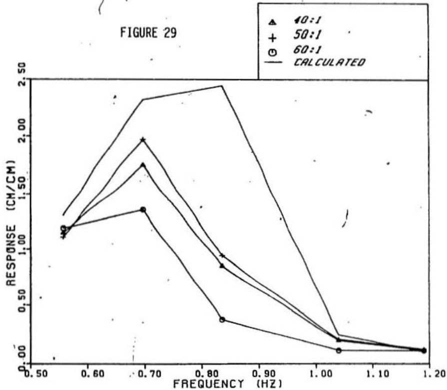

MED. CUBE...HEAVE RESP....REG. WAVES

FIGURE 30

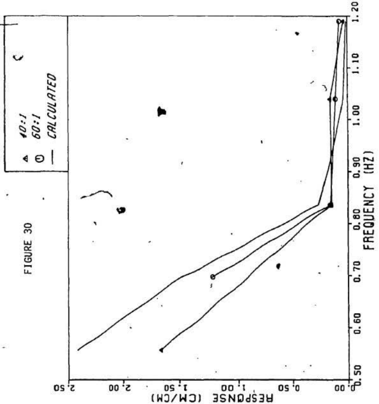

LAR. CUBE...HEAVE RESP.....REG. WAVES

FIGURE 31

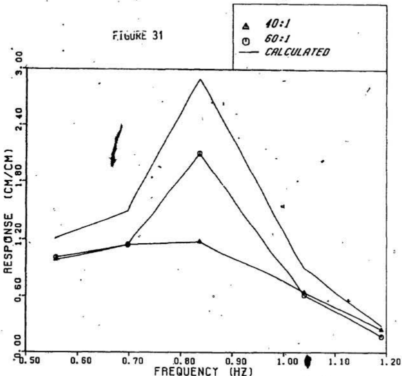

CYLINDER....HEAVE RESP....REG. WAVES

FIGURE 32

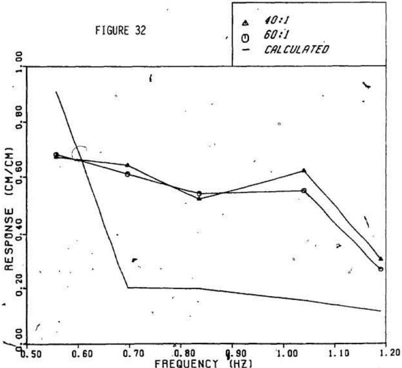

TRAPEZOID...HEAVE RESP....REG. WAVES

FIGURE 33

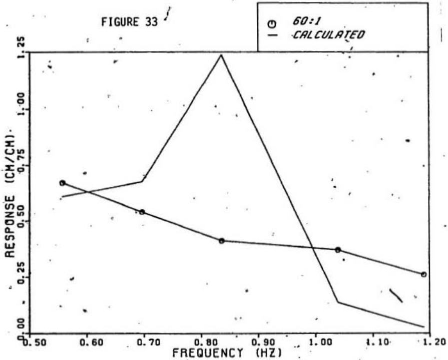

SPHERE...HEAVE RESPONSE...REG. WAVES

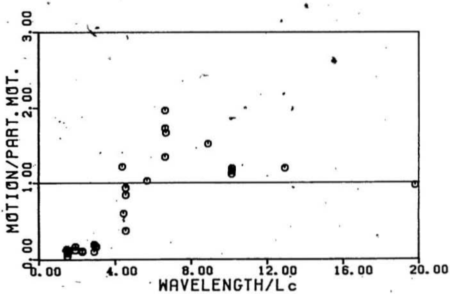

FIGURE 34 Heave motion/Particle motion vs. non-dimensional wavelength (All cubes)

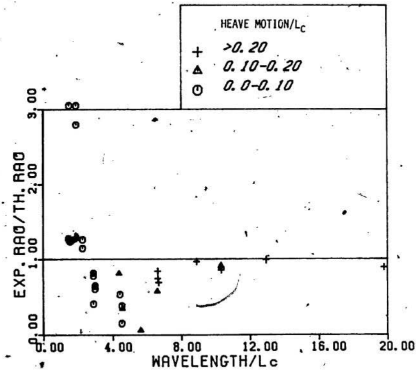

FIGURE 35 Experimental RAO/Theoretical RAO vs. Non-dimensional wavelength
(Three categories of non-dimensional heave motion)
(All cubes)

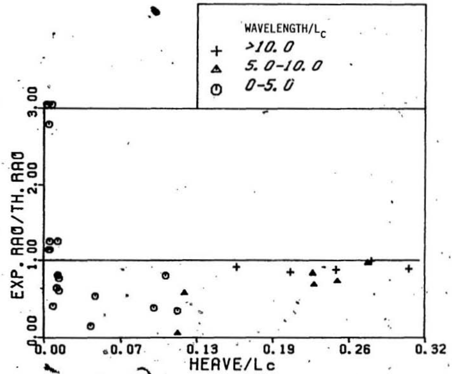

FIGURE 36 Experimental RAQ/Theoretical RAO vs. non-dimensional Heave motion
(Three categories of non-dimensional wavelength)
(All cubes)

3.2 Irregular Seas

In this portion of the experiment a comparison is made between response spectra of the bergs as measured by the Selspot System, and those determined by combining Response Amplitude Operators for the berg in question with the measured wave spectra. Two different "theoretical" response spectra have been determined for each test, one using the theoretical RAO's determined using Sen's program, and one using the experimentally determined RAO's from the regular wave tests. In this section these two theoretical spectra will be referred to as "predicted using calculated RAO's" and "predicted using experimental RAO's".

In all cases the measured sea spectra have been used rather than the target Jonswap spectra when generating predicted response spectra. The issue under study here is how well the linear theory can be used to predict motion in an irregular seaway, rather than the ability of the experimental equipment to produce a target sea state.

3.2.1 Surge Results

3.2.1.1. Large Cube

The surge spectra for this particular model appear in Figures (37-38). In Figure (37) the spectra for surge response for test LIR857 is shown. The spectra show peaks at approximately .65 and .75 Hz as well as a low frequency peak in the .1 Hz region. It is interesting to note that the low frequency peaks appeared (though with different magnitudes) in both the actual as well as the predicted traces, so there can be no doubt about their existence. However, the expected peak period for the associated wave spectrum was 1.30 seconds. It is expected that the great majority of response energy should be in the .75 Hz range. The low frequency peaks are due to relatively low amplitude, long period waves present in the tank during the test. The surge response of a body to such a long wave can be quite great. The result of this effect is quite a substantial low frequency peak in surge response. The relative size of the peak in the spectrum determined using the experimentally determined RAO's can be traced to the slope of the RAO curve in the low frequency region. The values of response were increasing at a rather large rate as frequency is reduced. The procedure used for determining the value of RAO outside the test range is a straight line extrapolation. This would lead to high values at low frequency such as in the 0.10 Hz region, and consequently unrealistically high peaks. This may be contrasted with the theoretically determined RAO values, which do not show such a large increase with decreasing frequency, and as a result the peaks are not of such great magnitude.

Several examples of the target Jonswap spectra as well as the associated measured wave spectra were shown in Figure 9-12. It can be clearly seen in these typical examples that while there is relatively little energy in this low frequency range compared to the .5-1.0 Hz range, there is significantly more energy in the measured versus the target JONSWAP spectra. This confirms that the low frequency peaks are the result of substantial surge response to relatively small amplitude waves which are preferentially present in the wave tank. As a result of this, further discussion in this section will be confined to those frequencies in the range of significant JONSWAP wave energy and will tend to ignore the relative magnitude of low frequency peaks. In this way, the problem of extrapolating the RAO's beyond the regular wave frequency points is also avoided.

There are three peaks in the actual response data, one at .63 Hz, another at .75 Hz, and a third at .88 Hz. The first is predicted quite accurately by the theory; while the second is predicted but has a lower magnitude than actual. The third peak is predicted by the theoretical algorithms, but its amplitude is not closely matched. The prediction of the frequency location of the spectral peaks is quite encouraging.

The magnitude variation between the three spectra may be traced to the discrepancy between calculated and experimentally determined RAO's. In Table (5) appear the values of the significant surge motion (peak - peak) determined by multiplying the square root of the area under the appropriate spectrum by a factor of 4.0. In cases where unrealistically high low frequency spectral peaks existed, the low frequency regions were not included in the integration procedure. For this particular case the value of significant surge amplitude predicted using experimental RAO's is within 19% of the actual but the value determined using calculated RAO's is only 65% as large as the actual.

In the frequency range containing the bulk of the response energy, say 0.55 to 1.0 Hz, the predicted surge RAO averages 70% of the experimental value (see Figure 17). The fact that the predicted significant surge motion is only 65% as large as actual is thus essentially due to the difference in RAO's in the region of peak energy. The predicted response in an irregular sea is not made much better or worse by the linear superposition applied using spectral analysis.

Many of the comments regarding surge motion made with respect to test LIR857 apply equally well to the results of LIR1143 (Figure (38)). Again the low frequency spikes are due to low frequency components developed in the tank. The expected peak frequency for this sea state is 0.67 Hz. This frequency is seen very well in the resulting spectra. The integration procedure results in very similar relative values as in the LIR857 sea state. The predicted significant surge motion using experimental RAO's is 6% lower than the value determined from the actual spectra. The value found using calculated RAO's is 55% of the actual value. Again, in the region containing most of the response energy, the theoretical RAO average 70% of the experimental values.

3.2.1.2 Cylinder

The spectra for surge response for the cylindrical model are shown in Figures (39-41). The most predominant frequency peak observed in the actual results of test CIR857 (at approximately .80 Hz) was matched quite accurately by the predicted spectra. Another peak at approximately .65 Hz was also observed in both the actual and predicted spectra, although without the same degree of matching as that associated with the higher peak. A further peak at .90 Hz is accurately predicted also.

The value of the significant surge motion, as determined using the areas under these spectra, for the "predicted using theoretical RAO" case is 80% as great as the value than for the actual data. This is to be expected, because the values of surge RAO in the peak frequency response region average about 85% of the experimentally determined values. The value for significant surge motion for the spectrum formed using measured RAO's is within 2.0% of the value determined from the actual spectrum (Table 5).

The surge response spectra for the cylinder in test CIR1143 are shown in Figure (40). The peaks predicted by the theory using both measured and calculated RAO's are located approxiamtely .15 Hz above a peak in the actual results.

A very encouraging point is to be found in the calculation of significant surge motion for these spectra. Even though the peaks were found at slightly different frequency locations, the signficant surge motions for actual and predicted using experimental RAO spectra were found to be within 1% of each other, essentially identical within experimental error. The value for predicted using calculated RAO's was found to be 82% as great as the actual case, which was to be expected considering the relationship between calculated and measured RAO's (see Table 5).

The CIR1429 surge spectra for the cylindrical model are shown in Figure (41). The peaks in the spectrum for actual data are for all intents and purposes identically matched by the predicted spectra. It is interesting to note how closely the peak energy frequency in these curves matches the Jonswap peak frequency of .60 Hz. The significant surge motion for the actual and "predicted using measured RAO" spectra are within 7% of one another. The value for the predicted using calculated RAO is 76% as great as the actual case (see Table 5), again, essentially a result of the ratio between predicted and measured RAO's in the region of peak wave energy.

3.2.1.3 Trapezoid

Plots of response spectra for the trapezoidal model appear in Figures (42-44). Energy peaks have been correctly predicted at the 0.75 Hz frequency area for test TIR857. This frequency range is close to the Jonswap peak frequency of 0.77 Hz for this significant sea height. The magnitude of the peaks in the spectra are not matched well between predicted and actual cases, but the significant surge motion, as determined using the area under the "predicted using experimental RAO" spectrum is within 2% of the actual value. The value determined using calculated RAO's is 64% of the actual value. This may again be explained by noting that the calculated RAO values for the frequencies .557-1.0 (where the great majority of the wave energy exists) average 61% of their measured counterparts (Table 5).

The surge response spectra for test TIR1143 shows excellent frequency location matching between predicted and actual cases. The significant surge motion for the predicted using measured RAO spectrum is within 13% of the value for the actual spectrum. As expected the value obtained using calculated RAO's is 72% as large as the actual value (Table 5).

The spectra for test TIR1429 are shown in Figure (44). The location of three frequency peaks are correctly matched by the predicted spectra (.43 Hz, .67 Hz, .88 Hz). The magnitudes of these frequency peaks are reasonably close to one another with the exception of the predicted using experimental RAO peak at 0.40 Hz. The large value of this peak may be traced to the steeply sloping RAO curve for this model in the lower frequency region. Having no regular wave data for this region, the only alternative is to extrapolate the curve to the desired frequency. Unfortunately this may lead to unrealistically high values for energy density in such frequency ranges. It is noted that the less steep theoretical RAO curve, when extrapolated, lead to a less severe and possibly more realistic value of surge response.

It is nevertheless encouraging to note that despite this problem the significant surge motion (experimental RAO) was only 6% greater than the value obtained for the actual spectrum. As was the case for the previously discussed sea states with this model, the significant surge motion (calculated RAO) was smaller than the actual case (69%).

3.2.1.4 Sphere

The surge response spectra for the spherical model are shown in Figures (45-47). Peaks in the SIR857 actual response spectrum at .67 and .77 Hz were correctly predicted by both theoretical spectra. The magnitude of the actual data peaks was quite closely matched by the spectrum determined using experimental RAO's. The significant surge motion for this spectrum was within 6% of the actual spectrum. The value for the spectrum found using calculated RAO's was only 33% as large as the actual figure. As in previous cases, this may be explained by noting that the values for theoretical surge RAO between .6 and 1.0 average 34% of the measured values (Table 5).

Very similar comments can be made regarding the SIR1143 sea response spectra. Energy peaks are very accurately predicted by the experimental RAO spectrum (magnitude of significant motion within 8%). The location of the peaks is confirmed by the calculated RAO spectrum but the signficant motion is 41% of the actual value. For the bulk response frequency range of .40-1.0 Hz the theoretical surge RAO's average 50% of their measured counterparts.

There are two predominant energy regions in the SIR1429 actual surge response spectrum. The location of the first, at .65 Hz, is accurately predicted by both theoretical spectra. The location of the second is .07 Hz greater than predicted. The magnitude of the peaks predicted by the experimental RAO spectrum are greater than the actual ones, but the value of significant surge motion is within 21% of the actual value. The value of significant surge motion (calculated RAO) is 56% of the actual value, which compares well with the 50% ratio of average RAO's in the region of peak wave energy.

Surge Motion

Model	Test	Frequency Range (Hz)	Significant Motion (CM) Actual	Experimental RAO	Theoretical RAO	Peak Energy Range (Δf) (Hz)	$\left(\frac{\text{Sig. Mot. (Theo. RAO)}}{\text{Sig. Mot. (Actual)}}\right)$	$\left(\frac{\text{Theo. RAO}}{\text{Exp. RAO}}\right)$ AVG. (In Range Δf)
Large Cube	LIR857	0.0 - 2.0	8.26	9.82	5.40	.55 - 1.0	.65	.70
	LIR1143	0.0 - 2.0	13.78	12.92	7.56	.55 - 1.0	.55	.70
Cylinder	CIR857	0.3 - 2.0	9.62	9.42	7.70	.55 - 1.0	.80	.85
	CIR1143	0.3 - 2.0	13.42	13.52	10.94	.40 - 1.0	.82	.85
	CIR1429	0.0 - 2.0	19.66	18.20	15.00	.40 - 1.0	.76	.85
Trapezoid	TIR857	0.2 - 2.0	11.22	11.44	7.12	.60 - 1.0	.64	.61
	TIR1143	0.2 - 2.0	14.16	15.94	10.22	.30 - 1.0	.72	.61
	TIR1429	0.0 - 2.0	21.32	22.64	14.66	.30 - 1.0	.69	.61
Sphere	SIR857	0.2 - 2.0	14.36	15.40	4.74	.60 - 1.0	.33	.34
	SIR1143	0.0 - 2.0	16.94	15.52	6.88	.40 - 1.0	.41	.50
	SIR1429	0.0 - 2.0	14.14	17.10	7.96	.50 - 1.0	.56	.50

TABLE 5

FIGURE 37

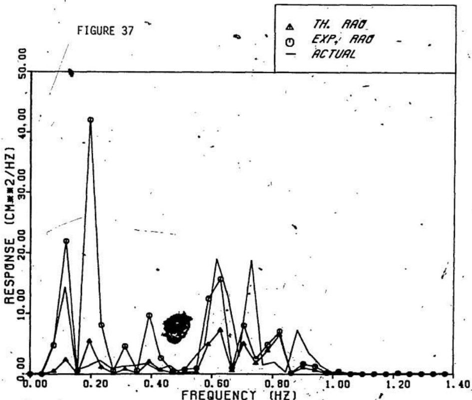

LARGE CUBE...SURGE RESPONSE...LIR857

FIGURE 38

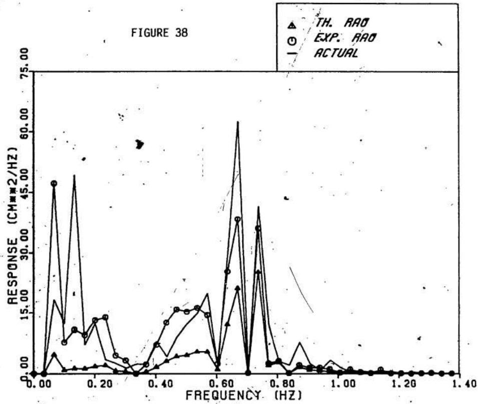

LARGE CUBE...SURGE RESPONSE...LIR1143

FIGURE 39

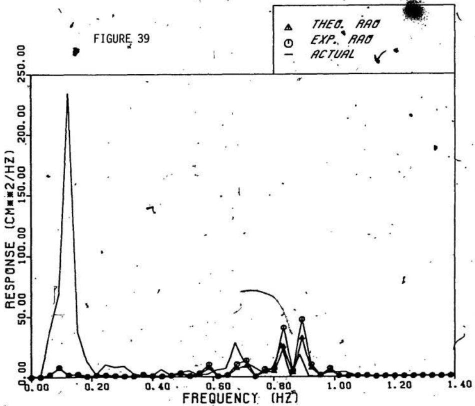

CYLINDER...SURGE RESPONSE...CIR857

FIGURE 40

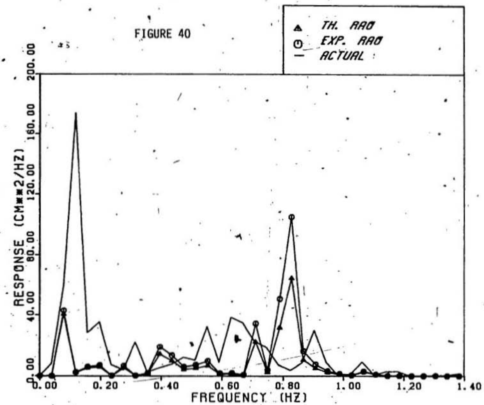

CYLINDER...SURGE RESPONSE...CIR1143

FIGURE 41

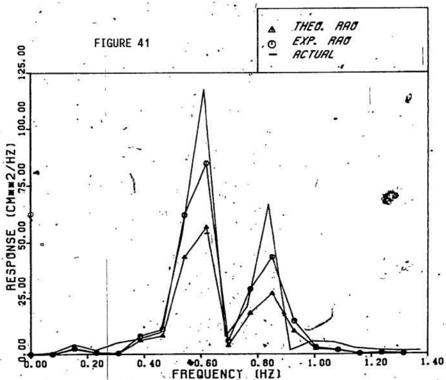

CYLINDER...SURGE RESPONSE...CIR1429

FIGURE 42

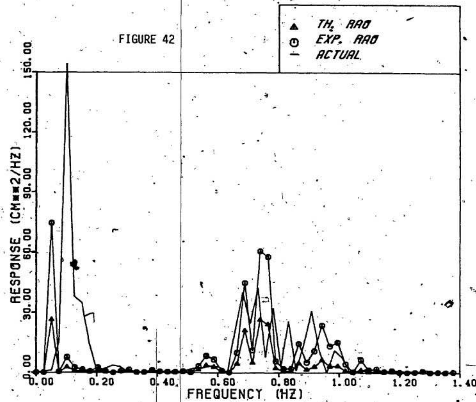

TRAPEZOID...SURGE RESPONSE...TIR857

FIGURE 43

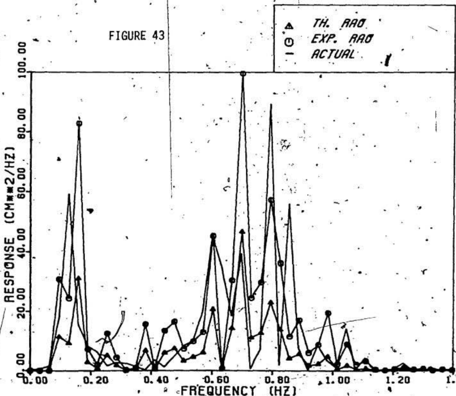

TRAPEZOID...SURGE RESPØNSE...TIR1143

FIGURE 44

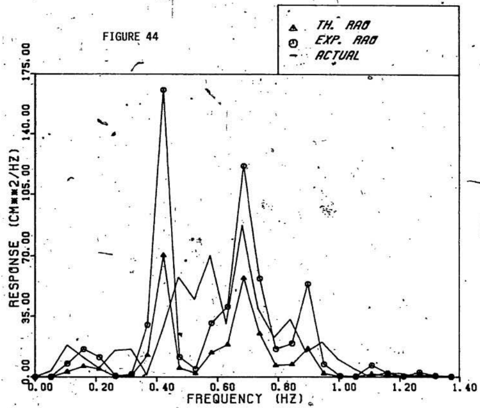

TRAPEZOID...SURGE RESPONSE...TIR1429

FIGURE 45

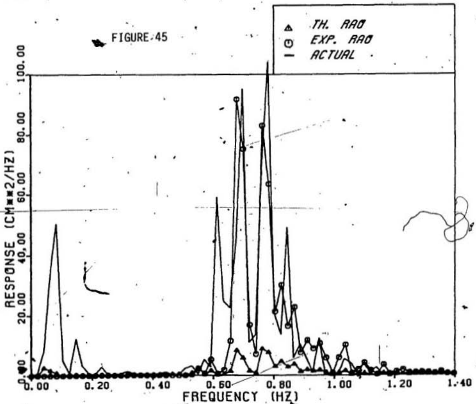

SPHERE... SURGE RESPONSE... SIR857

FIGURE 46

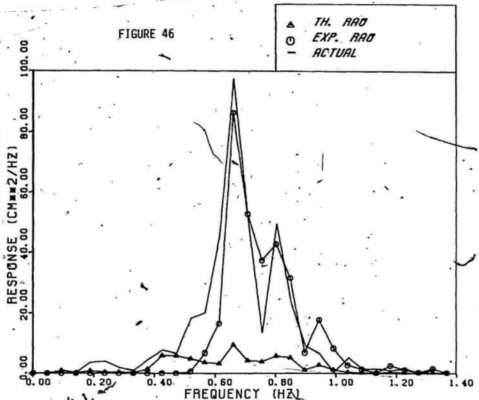

SPHERE...SURGE RESPONSE...SIR1143

FIGURE 47

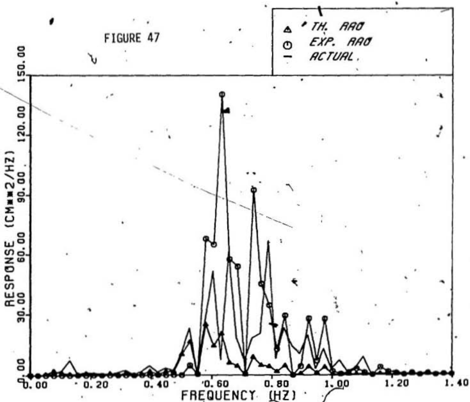

SPHERE...SURGE RESPONSE...SIR1429

3.2.2 Heave Results

3.2.2.1 Large Cube

The spectra showing heave results for this model are shown in Figures (48-49). For the LIR857 test there is a substantial low frequency (.1 Hz) peak in the predicted spectra. Only a very small peak occurs in the "actual" spectrum. The large magnitude of the predicted peak is a consequence of a steeply rising low frequency RAO curve. The lack of large spikes in the actual heave response spectra confirms the explanation suggested for those existing in corresponding surge results. The heave response of a floating body to a low-frequency small amplitude wave is not great and would not result in large energy spikes. There is very good matching between predicted and actual spectra at higher frequencies for this test. The actual and experimental RAO spectra show significant heave motion values within 8% of one another (see Table 6). The value determined using calculated RAO's is 25% higher than the actual case. For the region of high response energy, however, the values of predicted RAO are an average of 41% higher than the experimentally determined ones, which in part accounts for this result.

The frequency location of maximum energy is accurately predicted but is lower than the Jonswap value of 0.77 Hz.

Similar comments can be made for the LIR1143 test (Figure 49). The low frequency peaks exist in the predicted spectra but not in the actual results. The location of peak energy is very accurately predicted.

As expected, the significant heave motion calculated using experimental RAO's is reasonably close (28% greater) to the actual value, whereas the value determined using theoretical RAO's is 80% greater than the actual case (see Table 6). The theoretical RAO values average approximately 42% higher, which again partially accounts for this result.

3.2.2.2 Cylinder

The heave response of the cylinder for the CIR857 test is shown in Figure (50). The location of peaks seen in the actual data is accurately predicted by both predicted spectra (using calculated and measured RAO's). The relative magnitudes of the response are a problem for this data group, but can be partially explained by the relative magnitudes of the RAO's.

The significant heave motion determined by integrating the "predicted using measured RAO" spectrum shows a value 21% greater than that calculated using the actual spectrum. The value determined using the "predicted using calculated RAO" spectrum is 92% greater than the "actual" value. The spectra for this test show a very narrow energy distribution closely clustered about the 0.80 frequency region. It is noted that the calculated RAO for a frequency of 0.836 Hz is 76% higher than the average measured value. This explains the large value of significant heave motion.

The heave response for the CIR1143 test is shown in Figure (51). The energy peaks predicted by the theory are approximately .08 Hz away from the peak seen in the actual data. The significant heave motion predicted using experimental RAO's is 42% greater than the actual, and the value determined using calculated RAO's is 126% greater. The difference in RAO's does not explain these results as well as for the other tests.

Cylinder heave response for test CIR1429 is shown in Figure (43). The spectra determined using both measured and calculated RAO's correctly mirror the location of two peaks observed in the "actual" spectrum.

The significant heave motion determined for these spectra is as expected. The value determined using measured RAO's is within 2% of the actual case, and the value determined using calculated RAO is 50% greater than the actual. These spectra show considerable energy between.6 and 1.0 Hz, and in this range the calculated RAO's are about 42% greater than their measured counterparts (Table 6).

3.2.2.3 Trapezoid

The heave response spectra for this model are shown in Figures (53-55). The spectra for the TIR857 test shows an energy peak near 0.75 Hz for both the actual and calculated using experimental RAO cases. The location of this peak is close to the Jonswap peak frequency (0.77 Hz). The spectrum determined from calculated RAO's showed an increase in magnitude near this frequency but not the clearly defined peak seen in the other two spectra.

The significant heave motion for the spectrum determined using experimental RAO's was 26% greater than the value determined using the actual spectrum. The value for the calculated RAO case was 75% as great as the actual value. this may be explained by noting that for the predominant energy frequency range (0.60-1.00) the average calculated heave RAO is 58% as great as the measured value (Table 6).

The spectra for heave response in the TIR1143 test is shown in Figure (54). The existence of energy peaks present in the actual data at .6, .7, and .8 Hz has been correctly predicted by the theory. The magnitude of these peaks has been reasonably well matched by the predicted using experimental RAO procedure. The large values of response predicted by the calculated RAO procedure in the low frequency range are a result of the extrapolation of the calculated RAO curve. The low values of response predicted in the higher frequency range by the calculated RAO procedure are a result of the low values of RAO calculated relative to the actual values. From the RAO curves (Figure (32)) it is observed that the calculated RAO curve crosses the measured one at a value of .60 Hz, and this is the value where the spectra are most closely matched.

The value for significant heave motion for the measured RAO method is 18% greater than the actual value, and the value for the calculated RAO method is 21% greater. However, the theoretical RAO values in the peak wave energy region average 42% less than the measured ones. This anomaly shows up the previously mentioned difficulty in predicting the motion of a body with dramatic variation in underwater geometry.

The results of the TIR1429 test clearly show the problems associated with the linear extrapolation procedure for estimating RAO values outside the frequency range of calculation (or experimentation). The actual and measured RAO spectra match quite well in this test, with energy peak locations accurately confirmed and the significant heave motions within 7% of one another. The large response at low frequency is again a result of the extrapolation of the theoretical RAO curve and the significant motion is 68% greater than actual data. Again, the theoretical RAO's average 42% less than the measured ones in the region of peak wave energy.

3.2.2.4 Sphere

The spectra for heave response of the spherical model are shown in Figures (56-58). An energy peak at .78 Hz in the SIR857 test is correctly predicted by both theoretical spectra. A predicted peak at .70 Hz is not very definite in the actual data.

The significant heave motion determined from the experimental RAO's is 20% less than the actual value. The value for the calculated RAO's is 23% greater than the actual data. This may be explained by noting that the theoretical RAO's are 39% greater than the measured counterparts for the peak response frequency range (see Table 6).

The SIR1143 test heave response spectra are seen in Figure (57). Energy peaks at .45, .67, and .88 Hz are quite accurately predicted, but the magnitude is accurately predicted only in the .67 Hz peak. As expected, the largest disparity in peak magnitudes occurs at approximately 0.80 Hz, the location at which measured and calculated RAO's differ by the largest amount.

Similar comments can be made with respect to the SIR1429 test heave response. The locations of energy peaks are quite accurately predicted, but a relatively wide disparity in peak magnitude exists in the .80 Hz region.

For both of these latter two tests, the differences between actual and "predicted using theoretical RAO" motions are not well accounted for by the difference in average RAO values in the peak wave energy region. However, the predicted significant heave motions are not much different than the actual, so it appears that the difference in RAO's has not led to a cooresponding difference in significant motions.

Heave Motion

Model	Test	Frequency Range (Hz)	Significant Motion (CM) Actual	Experimental RAO	Theoretical RAO	Peak Energy Range (Δf) (Hz)	$\left(\frac{\text{Sig. Mot. (Theo. RAO)}}{\text{Sig. Mot. (Actual)}}\right)$	$\left(\frac{\text{Theo. RAO}}{\text{Exp. RAO}}\right)_{\text{AVG.}}$ (In Range Δf)
Large Cube	LIR857	0.4 - 2.0	14.02	12.84	17.52	.55 - 1.0	1.250	1.418
	LIR1143	0.4 - 2.0	17.70	22.68	31.80	.55 - 1.0	1.797	1.418
Cylinder	CIR857	0.0 - 2.0	13.02	15.82	25.04	.55 - 1.0	1.923	1.423
	CIR1143	0.0 - 2.0	15.58	22.16	35.18	.40 - 1.0	2.258	1.423
	CIR1429	0.0 - 2.0	24.90	25.38	37.24	.40 - 1.0	1.496	1.423
Trapezoid	TIR857	0.2 - 2.0	6.58	8.34	4.98	.60 - 1.0	.757	.581
	TIR1143	0.2 - 2.0	9.30	11.00	11.28	.30 - 1.0	1.213	.581
	TIR1429	0.0 - 2.0	15.44	14.36	25.86	.30 - 1.0	1.675	.581
Sphere	SIR857	0.0 - 2.0	7.90	6.36	9.70	.60 - 1.0	1.228	1.387
	SIR1143	0.1 - 2.0	11.38	8.88	11.68	.40 - 1.0	1.026	1.387
	SIR1429	0.1 - 2.0	13.36	10.48	12.30	.50 - 1.0	.921	1.387

TABLE 6

FIGURE 48

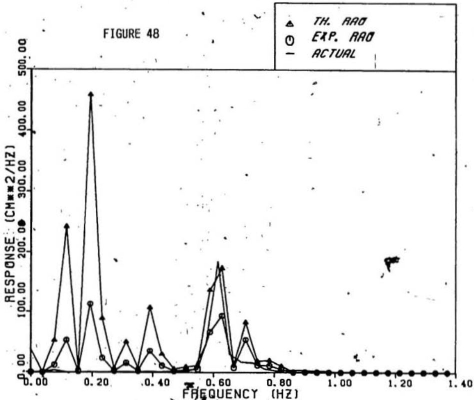

LARGE CUBE...HEAVE RESPONSE...LIR857

FIGURE 49

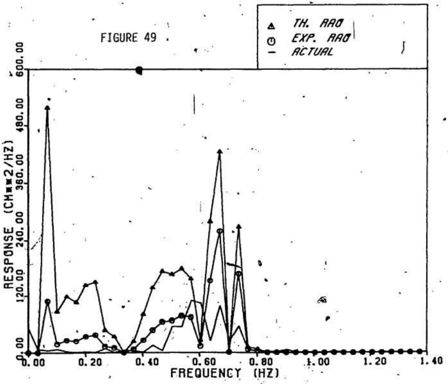

LARGE CUBE...HEAVE RESPONSE...LIR1143

FIGURE 50

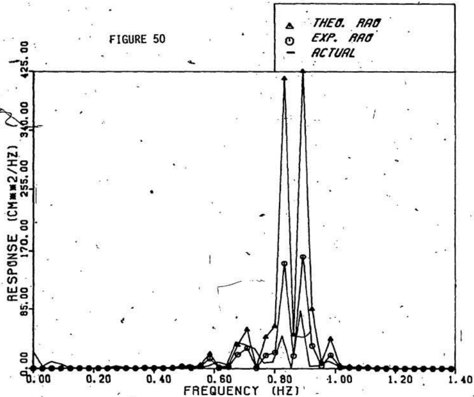

CYLINDER...HEAVE RESPONSE...CIR857

FIGURE 51

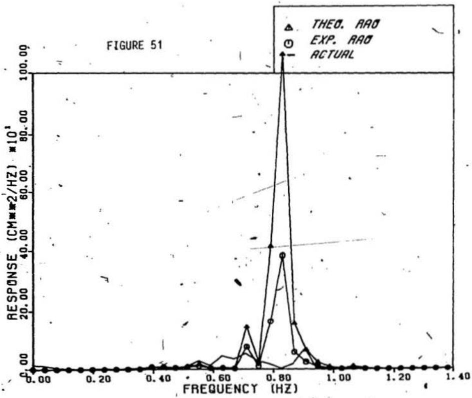

CYLINDER...HEAVE RESPONSE...CIR1143

FIGURE 52

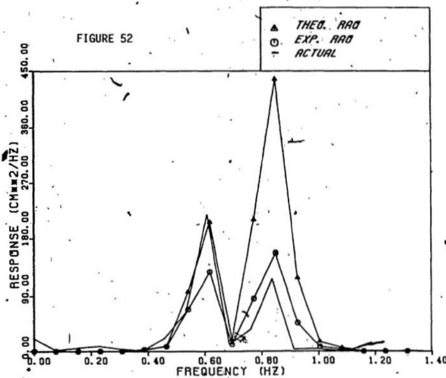

CYLINDER...HEAVE RESPONSE...CIR1429

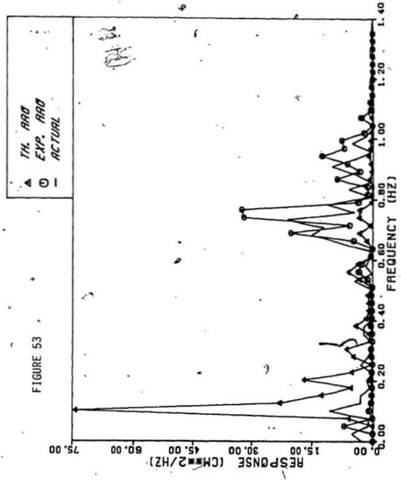

FIGURE 53

TRAPEZOID...HEAVE RESPONSE...TIR857

FIGURE 54

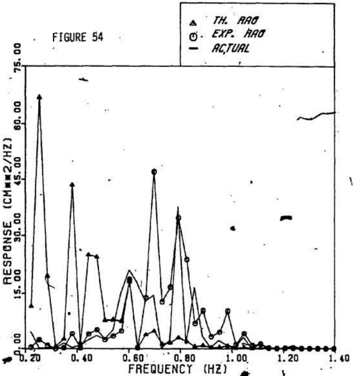

TRAPEZOID...HEAVE RESPONSE...TIR1143

FIGURE 55

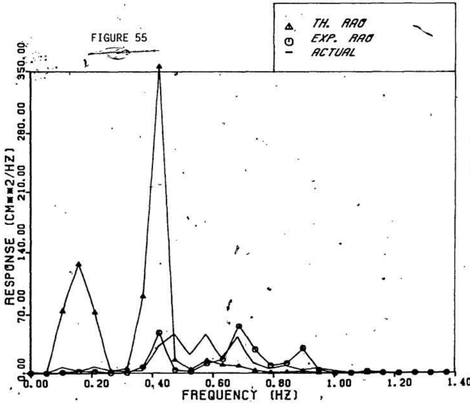

TRAPEZOID...HEAVE RESPONSE...TIR1429

FIGURE 56

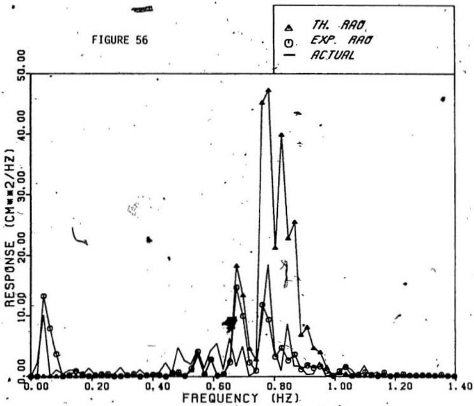

SPHERE...HEAVE RESPONSE...SIR857

FIGURE 57

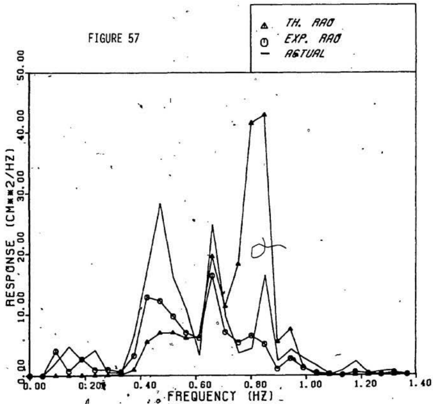

SPHERE...HEAVE RESPONSE...SIR1143

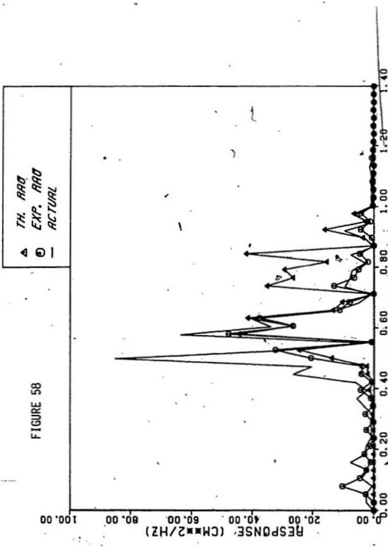

FIGURE 58

SPHERE... HEAVE RESPONSE... SIR1429

4.0 DISCUSSION AND CONCLUSIONS

There were two major objectives of this work. Firstly, the applicability of linear diffraction theory to predicting the motion of ice masses in regular waves was to be studied. Secondly, the principle of linear superposition as applied to the prediction of motion in irregular waves was to be investigated.

Several variables were thought to affect the prediction accuracy, and the experiments were carried out to specifically study these properties. Linear diffraction theory neglects the effect of viscosity entirely. In order to study this effect three cubes having lengths in the ratio 1:2:3 were studied while under the action of waves having lengths in the identical ratio. These cases are identical from the point of view of Froudian scaling, but, since viscous forces are directly related to Reynold's number and body characteristic length, viscous effects will differ. As reported in the previous section, it was seen that a general improvement in prediction occurred as the size of the model was increased. Viscous effects, then, result in increasing error as smaller models are used. This is an important result when considering the size of the most important "models", - real icebergs.

Linear theory also assumes that the motion of the body relative to its size will be small. To study the effect of this variable on prediction accuracy the cubes were again used. The amplitude of motion of the cubes in each test run was normalized with body characteristic length and plotted against a measure of prediction error. The surge results showed a general trend of increasing error with increasing motion amplitude, but the same could not be said for heave results. It is thought that viscosity effects caused the ambiguous nature of the heave plot. As described in the introduction, viscosity-induced problems in motion prediction are related to the ratio λ/Lc. Motion amplitude is unfortunately also related to the wavelength λ, and as a result an independent study of viscosity or motion amplitude related problems is difficult. Two more general points with respect to the experiments and these effects are as follows. Firstly, considering all test frequencies, surge RAO's were more accurately predicted for the large cube than the smaller ones. This is as expected, since the associated relative motion amplitudes were smaller for the large cube, and viscosity is expected to produce smaller errors for larger models. Secondly, RAO's in general showed better matching for high frequency surge and non-resonance heave conditions where body motion amplitude was small, than for the corresponding low frequency surge and heave resonance situations.

The shape of the icebergs was thought to affect the ability of linear theory to predict motion. The theory assumes that little change will occur in two important parameters - waterline area and underwater shape - as the body oscillates. This will be the case for bodies having relatively straight (vertical) sides, such as the cubes and cylinder, but the trapezoid and sphere were expected to present some problems with this assumption. The results here were clear. The cylinder in fact produced the best average results, with the cubes next and the trapezoid and sphere showing the poorest matching. The fact that the cylinder outperformed the cubes was due to the fact that it possessed the additional advantage of not presenting a different shape to the wave front as the inevitable yawing motion occurred during the experiments.

Linear theory assumes that the waves under study will be relatively "shallow" in nature, that is, their ratio of wavelength to wave height will be large. To discover whether this problem appeared in practice, tests were run at several different steepnesses. However, the results of this study were not conclusive. A trend of improved prediction existed for the medium cube as shallower waves were used, but this trend was not repeated for the other berg shapes. Undoubtedly an insufficient range of steepnesses were used to clearly observe the effect of wave steepness, owing to the previously mentioned model rolling problems.

Throughout the entire test program it was observed that surge was underpredicted by theory, whereas heave was consistently overpredicted. It is thought that second order wave effects caused the models to surge more than expected. Heave motion, alternatively, was generally damped by fluid viscosity and was hence lower than predicted.

The irregular sea portion of the tests brought forward some interesting points to be considered when predicting berg motion in an irregular seaway. If RAO's are used to determine berg motion, the spectral results will in general be as accurate as are the RAO's. The experiment has shown significant discrepancies between calculated and measured RAO's in heave resonance and high surge amplitude regions. If the bulk of the wave energy is in such a high amplitude region, the discrepancies in response spectrum shape can be considerable. If, however, the bulk of wave energy is located at a region where RAO's closely match measured results, good spectral prediction can be expected.

Problems were encountered when extrapolating a steeply rising RAO curve outside the region of measured results. This practice may lead to unrealistically high RAO values and resulting problems with response spectrum shape.

In figures 59-66 the full scale signficant surge and heave motions for each model have been plotted against significant wave height. The points determined from actual response data and those from spectra generated using experimental RAO's are very close to one another in most cases. This confirms the prediction procedure's accuracy as a tool for motion prediction in an irregular seaway. This is a useful and non-trivial result, in that while the models were seen to exhibit considerable non-linear behaviour (submergence, large excursions from zero position), the principle of linear superposition has held up quite well.

The effect of wave groups should be mentioned in this work. Such groups result from the existence of a series of waves having similar frequencies. They may be described physically as a wave packet or envelope travelling in a wave train. Forces associated with such wave groups are proportional to the product of the amplitudes of the constituent waves. These forces occur predominantly at frequencies representing differences between constituent waves' frequencies. Such forces will then become a problem only for bodies experiencing resonance at low frequencies corresponding to the difference in frequency between waves within a group, for example a moored semi-submersible. Low frequency spectral disturbances caused by group phenomena would be indistinguishable from those previously mentioned caused by residual waves in the tank. As described earlier, these low frequency problems were eliminated prior to spectral analysis. The fact that the significant motion of the bodies could be predicted by combining RAO's with wave spectra is a good indication that second order group related forces have not created a problem for the experiments.

The points from spectra generated using theoretical RAO's are somewhat lower in surge motion and usually somewhat higher in heave motion. The accuracy of these points is closely tied to the accuracy of the RAO's used to generate them. Care should be taken when applying this procedure and as many RAO calculations or experiments as possible should be carried out to ensure that the total range of significant wave energy is covered with good frequency resolution.

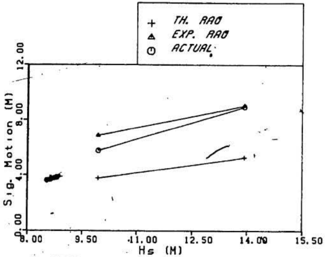

FIGURE 59
LARGE CUBE
SIG. SURGE MOT. VS SIG. WV. HGT.

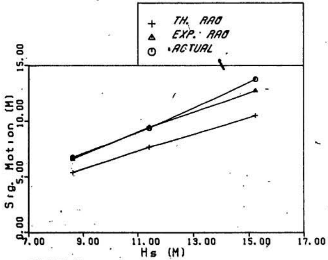

FIGURE 60
CYLINDER
SIG. SURGE MOT. VS SIG. WV. HGT.

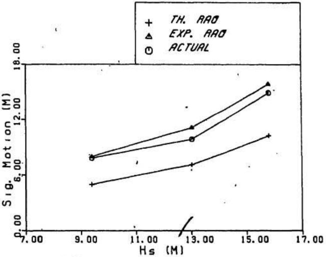

FIGURE 6.1
TRAPEZOID
SIG. SURGE MOT. VS SIG. WV. HGT.

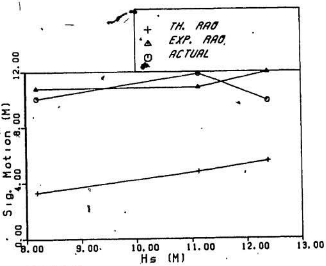

FIGURE 62
SPHERE
SIG. SURGE MOT. VS SIG. WV. HGT.

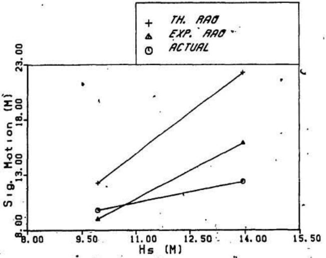

FIGURE 63
LARGE CUBE
SIG. HEAVE MOT. VS SIG. WV. HGT.

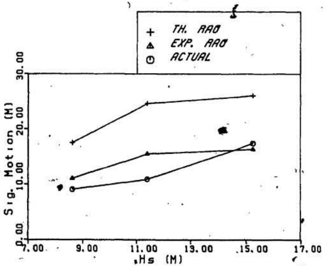

FIGURE 64
CYLINDER
SIG. HEAVE MOT. VS SIG. WV. HGT.

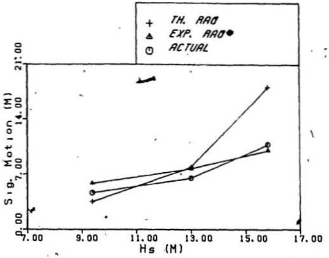

FIGURE 65
TRAPEZOID
SIG. HEAVE MOT. VS SIG. WV. HGT.

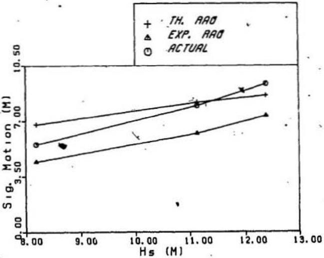

FIGURE 66
SPHERE
SIG. HEAVE MOT. VS SIG. WV. HGT.

5.0 FURTHER RESEARCH

Any experimental work leads to a series of further questions to be answered and "things we could have done differently". This experiment is no exception. Already in mind is an improved method of handling the irregular portion of the experiment. If the towing carriage could be used as a base for the selspot cameras and moved along with the berg as it is excited by an irregular wave train, the motion of the carriage could be accounted for and later removed from Selspot data. In this way there would be an unlimited period of time during which data could be gathered, undoubtedly leading to smoother spectral forms.

Another experiment to be investigated involves the motion of icebergs in the area of a semi-submersible. Data gathering is at present difficult with two moving bodies in the tank, but problems are being gradually eliminated. An experiment involving a statistically significant number of test runs to study berg motion near a semi-submersible is presently under consideration.

REFERENCES

1. Arockiasamy, M., Reddy, D.V., and Muggeridge, D.B., "Dynamic Responses of Moored Semi-Submersibles in an Ice Environment," Structures Congress, ASCE, Houston, 1983.

2. Cammaert, A.B., Wong, T.T., and Curtis, D.D., "Impact of Icebergs on Offshore Gravity and Floating Platforms", POAC '83, Helsinki, 1983.

3. Joordan, Appleby, and Fidjestoel, "Ice Structure Interaction - Some Recent Veritas Approaches," Journal of Canadian Petroleum Technology, Volume 22, Number 6, pp. 55-57 (November-December), 1983.

4. Marex Marine Environmental Services Ltd., "Offshore Labrador 1975," Summary Report Prepared for Eastcan, 1976.

5. Marex Marine Environmental Services Ltd., "Iceberg Observations," Offshore Labrador - Appendix 3, Iceberg Observations D.V. Sedco 445, 1975.

6. Lever, J.H., Reimer, E., and Diemand, D., "A Model Study of the Wave Induced Motion of Small Icebergs and Bergy Bits", Proceedings of 3rd Offshore Mechanics and Arctic Engineering Symposium, New Orleans, Vol. III, 1984, pp. 282-290.

REFERENCES (Cont'd)

7. Sen, D., "Prediction of Wave Loads and Motions of Floating Marine Structures by Three-Dimensional Flow Theory", M. Eng. Thesis, Faculty of Engineering and Applied Science, Memorial University of Newfoundland, St. John's, Newfoundland, 1983.

8. Kim, W.D., "On the Harmonic Oscillation of a Rigid Body on a Free Surface", Journal of Fluid Mechanics, Vol. 21, Part 3, 1965, pp. 427-451.

9. Garrison, C.J., "Hydrodynamics of Large Objects in the Sea, Part II: Motion of Free Floating Bodies", Journal of Hydronautics, Vol. 9, No. 2, 1975, pp. 58-63.

10. Faltinsen, O.M., and Michelsen, F.C., "Motion of Large Structures in Waves at Zero Froude No.", Int. Sym. on Dynamics of Marine Vehicles and Structures in Waves, London, 1974, pp. 91-106.

11. Hsuing, C.C., Sen, D., and Tse, C.C., "Floating Production System: Hydrodynamics Analysis and Model Testing", Technical Report to CanOcean Ltd., Memorial University of Newfoundland, 1983.

12. Nojiro, N., "A Study of Hydrodynamic Pressures and Wave Loads on Three-Dimensional Floating Bodies", IHI Engineering Review, Vol. 14, No. 2, 1981, pp. 6-20.

REFERENCES (Cont'd)

13. Pinkster, J.A., and Van Oortmerssen, G., "Computation of the First and Second Order Wave Forces on Bodies Oscillating in Regular Waves", Proc. of 2nd Int. Cnf. on Numerical Ship Hydrocynamics, U. of California, Berkely, 1977, pp. 136-166.

14. Lever, J.H., and Sen, D., "A Method of Upgrade Iceberg Velocity Statistics to Include Wave-Induced Motion", OMAE, Tokyo, 1986. Vol. IV, pp. 320-327.

15. Leblond, P.H., Calisal, S.M., and Isaacson, M., "Wave Spectra in Canadian Waters", Canadian Contract Report of Hydrography and Ocean Sciences.

16. Battacharya, R., "Dynamics of Marine Vehicles", Wiley, New York, 1978.

17. Milgram, J.H., "Waves and Wave Forces", Marine Science Communications, 1978.

18. Muggeridge, Chen, Murray, "Calibration of a 58 m Wave Flume and an Initial Study of the Response of a Circular Cylinder to Sinusoidal Waves", Faculty of Engineering and Applied Science, MUN, 1981.

19. Laurich, P.H., "The Selspot System", Selcom Ltd., 1984.

20. Chatfield, "The Analysis of Time Series", Chapman and Hall, 1980.

APPENDIX 1

REGULAR WAVE RESULTS

SMALL CUBE

TEST	WAVE HGT	SURGE	SURGE / WAVE HGT	PREDICTED	% DISCREPANCY	HEAVE	HEAVE / WAVE HGT	PREDICTED	% DISCREPANCY
D557A60	7.94	6.74	0.85	0.9527	11	7.69	0.97	1.079	10
D697A60	5.74	4.78	0.83	1.9840	58	6.90	1.20	1.209	1
D836A60	4.49	3.29	0.73	0.2147	242	6.82	1.52	1.564	3
D104A60	2.73	1.76	0.65	0.3106	108	2.82	1.03	16.600	94
D119A60	1.89	1.00	0.54	0.3009	79	1.10	0.60	1.114	46

PITCH MOTION
(SMALL CUBE)

TEST	WAVE AMP	PITCH (RAD)	NON-DIM'L PITCH	PREDICTED	DISCREPANCY
D557A60	3.97	0.1692	1.054	2.596	59
D697A60	2.87	0.1269	1.094	21.23	95
D836A60	2.25	0.0550	0.605	2.787	78
D104A60	1.37	0.0516	0.931	1.332	30
D119A60	0.95	0.0201	0.523	0.976	46

MEDIUM CUBE

TEST	WAVE HGT	SURGE	SURGE / WAVE HGT	PREDICTED	% DISCREPANCY	HEAVE	HEAVE / WAVE HGT	PREDICTED	% DISCREPANCY
M557A60	6.60	5.41	0.82	0.4632	77	7.92	1.20	1.3030	8
M557A50	9.07	7.41	0.82		77	10.16	1.12		14
M557A40	10.37	9.24	0.89		92	12.06	1.16		11
M697A60	4.30	3.29	0.77	0.4139	86	5.80	1.35	2.3230	42
M697A50	5.61	4.39	0.78		88	11.06	1.97		15
M697A40	7.00	5.57	0.80		93	12.08	1.73		26
M836A60	5.10	1.68	0.33	0.3620	9	1.94	0.38	2:4500	84
M836A50	4.83	2.20	0.45		24	4.55	0.94		60
M836A40	6.50	3.65	0.56		55	5.53	0.85		63
M104A60	4.30	1.06	0.25	0.2893	14	0.41	0.10	0.2434	59
M104A50	2.79	1.04	0.37		28	0.57	0.20		18
M104A40	3.30	1.49	0.45		56	0.63	0.19		22
M119A60	1.83	0.44	0.24	0.2431	1	0.18	0.10	0.0873	15
M119A50	2.10	0.54	0.26		7	0.24	0.11		26
M119A40	2.50	0.88	0.35		44	0.25	0.10		15
M119A20	5.41	1.71	0.32		32	0.59	0.11		26

PITCH MOTION
(MEDIUM CUBE)

TEST	WAVE AMP	PITCH (RAD)	NON-DIM'L PITCH	PREDICTED	DISCREPANCY
M557A60	3.3	0.1269	1.860	1.252	49
M557A50	4.5	0.0444	0.477		62
M557A40	5.2	0.0635	0.590		53
M697A60	2.2	0.0381	0.837	0.975	14
M697A50	2.8	0.0349	0.603		38
M697A40	3.5	0.0423	0.585		40
M836A60	2.6	0.0159	0.295	0.762	61
M836A50	2.4	0.0296	0.596		22
M836A40	3.2	0.0412	0.623		18
M104A60	2.2	0.0079	0.174	0.525	67
M104A50	1.4	0.0106	0.365		30
M104A40	1.7	0.0138	0.391		26
M119A60	0.9	0.0063	0.338	0.385	12
M119A50	1.1	0.0085	0.372		3
M119A40	1.3	0.0106	0.393		2
M119A20	2.7	0.0159	0.283		27

LARGE CUBE

TEST	WAVE HGT	SURGE	SURGE / WAVE HGT	PREDICTED	% DISCREPANCY	HEAVE	HEAVE / WAVE HGT	PREDICTED	% DISCREPANCY
L557A40	10.10	6.96	0.69	0.4337	59	16.86	1.67	2.409	31
* L697A60	6.25	2.90	0.46	0.3521	32	7.61	1.22	1.491	~~18~~
L836A60	4.62	1.65	0.36	0.2908	23	0.78	0.17	0.262	35
L836A40	5.80	2.00	0.34		19	0.92	0.16		39
L104A60	2.24	0.74	0.33	0.2101	56	0.26	0.12	0.043	174
L104A40	2.90	1.14	0.39		87	0.49	0.17		295
L119A60	2.54	0.53	0.20	0.1509	33	0.20	0.08	0.012	522
L119A40	3.54	0.65	0.18		21	0.16	0.04		257

* Measurable data period quite short

PITCH MOTION
(LARGE CUBE)

TEST	WAVE AMP	PITCH (RAD)	NON-DIM'L PITCH	PREDICTED	DISCREPANCY
L557A40	5.05	0.0740	1.0678	1.1690	9
* L697A60	3.13	0.0148	0.3446	0.7887	56
L836A60	2.31	0.0132	0.4169	0.5589	25
L836A40	2.90	0.0201	0.5047		10
L104A60	1.12	0.0103	0.6706	0.3155	112
L104A40	1.45	0.0127	0.6376		102
L119A60	1.27	0.0106	0.6065	0.1828	232
L119A40	1.77	0.0085	0.3482		90

* Measurable data period quite short

CYLINDER

TEST	WAVE HGT	SURGE	SURGE / WAVE HGT	PREDICTED	% DISCREPANCY	HEAVE	HEAVE / WAVE HGT	PREDICTED	% DISCREPANCY
C557A60	7.35	6.65	0.90	0.7603	19	7.53	1.02	1.2070	15
C557A40	11.30	9.94	0.88		16	11.24	0.99		18
C697A60	5.51	4.47	0.81	0.6589	23	6.35	1.15	1.5070	23
C697A40	8.35	6.86	0.82		25	9.61	1.15		24
C836A60	3.30	3.69	1.11	0.7009	60	6.90	2.09	2.8930	28
* C836A40	6.97	4.80	0.68		1.7	8.23	1.18		59
C104A60	2.58	1.18	0.46	0.4186	8.9	1.57	0.61	0.8867	31
C104A40	3.70	1.57	0.42		1.3	2.35	0.64		28
C119A60	1.70	0.59	0.35	0.3517	1.6	0.27	0.16	0.2693	40
C119A40	3.11	1.14	0.37		3.9	0.71	0.23		16

* Measurable data period quite short

PITCH MOTION
(CYLINDER)

TEST	WAVE AMP	PITCH (RAD)	NON-DIM'L PITCH	PREDICTED	DISCREPANCY
C557A60	3.68	0.065	0.8478	0.0736	1052
C557A40	5.65	0.090	0.7683		944
C697A60	2.76	0.090	1.5723	0.2743	473
C697A40	4.18	0.015	1.6648		506
C83[illegible]0	1.65	0.115	3.3455	4.7400	29
* C836A40	3.49	0.105	1.4400		70
C104A60	1.29	0.045	1.6730	0.4698	256
C104A40	1.85	0.065	1.6800		258
C119A60	0.85	0.015	0.7418	0.3347	121
C119A40	1.56	0.025	0.7500		124

* Measurable data period quite short

TRAPEZOID

TEST	WAVE HGT	SURGE	SURGE / WAVE HGT	PREDICTED	% DISCREPANCY	HEAVE	HEAVE / WAVE HGT	PREDICTED	% DISCREPANCY
T557A60	6.30	8.10	1.28	0.7329	75	4.26	0.68	0.9128	26
T557A40	11.00	10.53	0.96		31	7.35	0.67		27
T697A60	5.53	4.91	0.88	0.6207	43	3.38	0.61	0.2017	202
T697A40	7.83	7.14	0.91		47	4.98	0.64		215
T836A60	3.83	3.18	0.83	0.5234	58	2.10	0.54	0.1980	171
T836A40	5.65	4.71	0.83		59	2.90	0.52		163
T104A60	2.30	2.17	0.94	0.3933	140	1.30	0.55	0.1601	243
T104A40	3.61	2.71	0.75		91	2.24	0.62		287
T119A60	2.15	1.03	0.48	0.3250	47	0.59	0.27	0.1178	132
T119A40	2.40	1.37	0.57		76	0.74	0.31		164

PITCH MOTION

(TRAPEZOID)

TEST	WAVE AMP	PITCH (RAD)	NON-DIM'L PITCH	PREDICTED	DISCREPANCY
T557A60	3.15	0.0555	0.8526	0.4832	76
T557A40	5.50	0.0666	0.5860		21
T697A60	2.77	0.0460	0.8034	0.4405	82
T697A40	3.92	0.0582	0.7178		63
T836A60	1.92	0.0357	0.8993	0.4217	113
T836A40	2.83	0.0529	0.9039		114
T104A60	1.15	0.0397	1.6680	0.4475	272
T104A40	1.81	0.0476	1.2720		184
T119A60	1.08	0.0222	0.9950	0.5436	83
T119A40	1.20	0.0264	1.0650		96

SPHERE

TEST	WAVE HGT	SURGE	SURGE / WAVE HGT	PREDICTED *	% DISCREPANCY	HEAVE	HEAVE / WAVE HGT	PREDICTED	% DISCREPANCY
S557A60	8.00	4.10	0.51	0.4742	7.5	5.33	0.67	0.6069	10
S697A60	5.98	9.60	1.60	0.4465	259	3.23	0.54	0.6755	20
S836A60	5.22	5.17	0.99	0.4056	144	2.11	0.41	1.2390	67
S104A60	3.42	2.98	0.87	0.3371	159	1.27	0.37	0.1362	174
S119A60	2.56	1.72	0.67	0.2954	128	0.67	0.26	0.0256	919

PITCH MOTION
(SPHERE)

TEST	WAVE AMP	PITCH (RAD)	NON-DIM'L PITCH	PREDICTED	DISCREPANCY
S557A60	4.00	0.1058	0.6876	1.547	56
S697A60	2.99	0.1745	1.5175	1.245	22
S836A60	2.61	0.0582	0.5795	1.045	45
S104A60	1.71	0.0307	0.4664	0.805	42
S119A60	3.78	0.0130	0.0894	0.681	87

APPENDIX 2

TIMESERIES RESPONSE RECORDS

SMALL CUBE

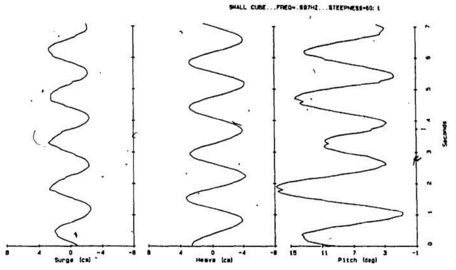
SMALL CUBE...FREQ=.697HZ...STEEPNESS=60:1
Surge (cm)
Heave (cm)
Pitch (deg)
Seconds

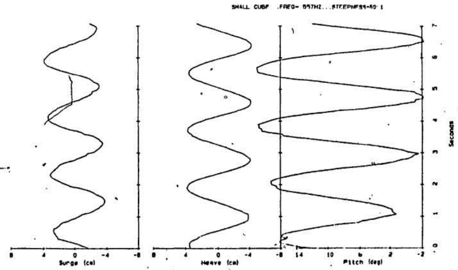
SMALL CUBE .FREQ=.597HZ...STEEPNESS=60:1
Surge (cm)
Heave (cm)
Pitch (deg)
Seconds

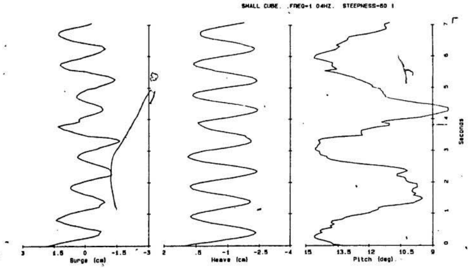
SMALL CUBE. FREQ=1 04HZ. STEEPNESS=60 1
Surge (cm)
Heave (cm)
Pitch (deg)
Seconds

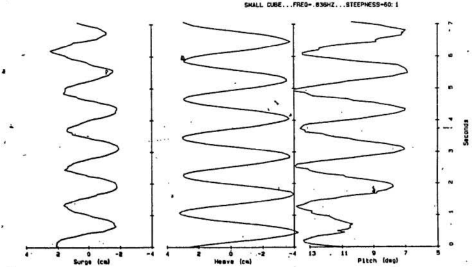
SMALL CUBE...FREQ=.836HZ...STEEPNESS=60:1
Surge (cm)
Heave (cm)
Pitch (deg)
Seconds

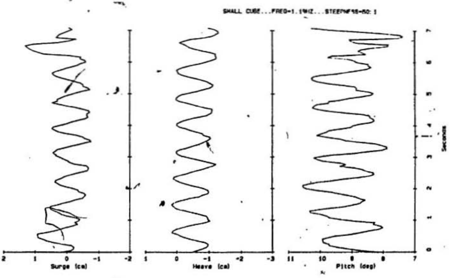
Surge (cm)
Heave (cm)
Pitch (deg)
Seconds

MEDIUM CUBE

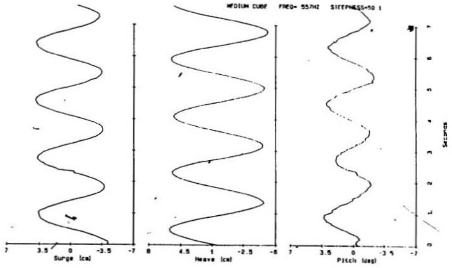
MEDIUM CUBE FREQ= 557HZ STEEPNESS=50 1
Surge (cm)
Heave (cm)
Pitch (deg)
Seconds

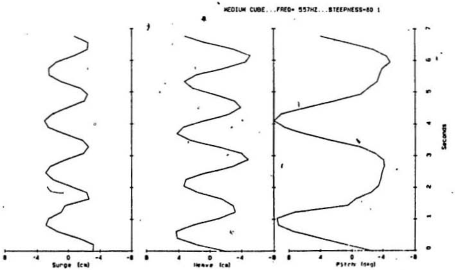
MEDIUM CUBE...FREQ= 557HZ...STEEPNESS=80 1
Surge (cm)
Heave (cm)
Pitch (deg)
Seconds

MEDIUM CUBE.. FREQ=.897HZ . STEEPNESS=60 1

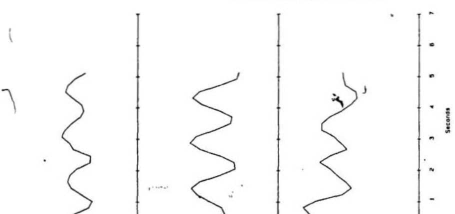

MEDIUM CUBE FREQ=.557HZ...STEEPNESS=40 1

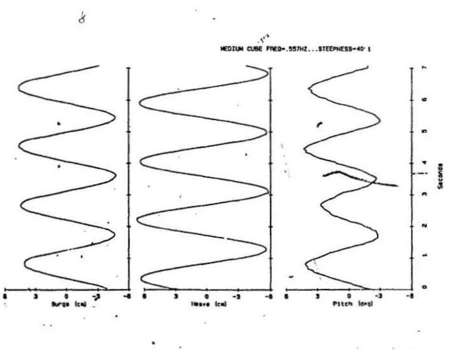

MEDIUM CUBE FREQ= 697HZ STEEPNESS=40 1

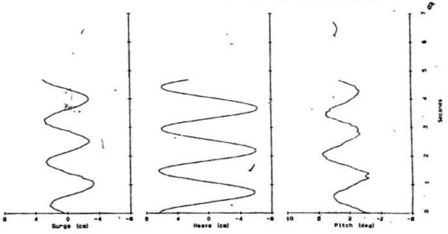

MEDIUM CUBE FREQ= 697HZ STEEPNESS=50 1

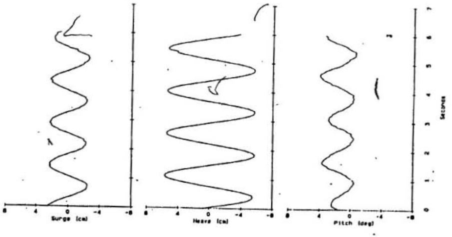

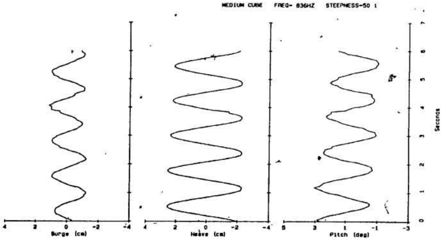
MEDIUM CUBE FREQ= 836HZ STEEPNESS=50 1
Surge (cm)
Heave (cm)
Pitch (deg)
Seconds

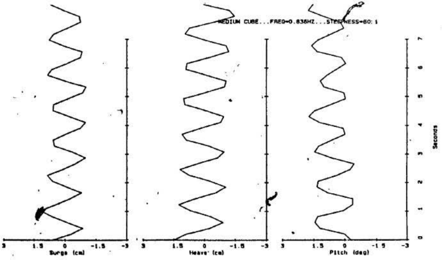
MEDIUM CUBE...FREQ=0.836HZ...STEEPNESS=60:1
Surge (cm)
Heave (cm)
Pitch (deg)
Seconds

MEDIUM CUBE. .FREQ=1.04HZ . .STEEPNESS=80:1

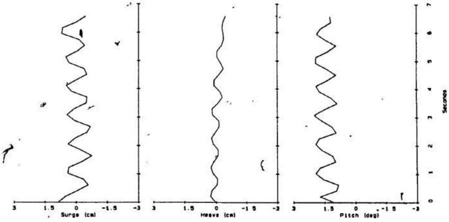

MEDIUM CUBE. FREQ=.836HZ . STEEPNESS=40:1

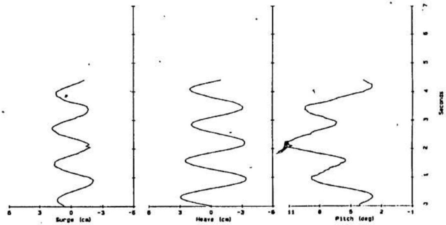

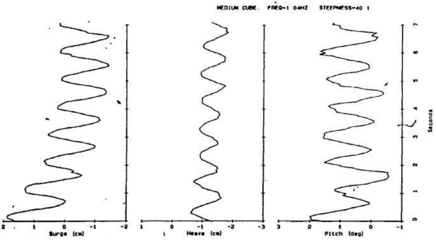
MEDIUM CUBE. FREQ=1 04HZ STEEPNESS=40 1
Surge (cm)
Heave (cm)
Pitch (deg)
Seconds

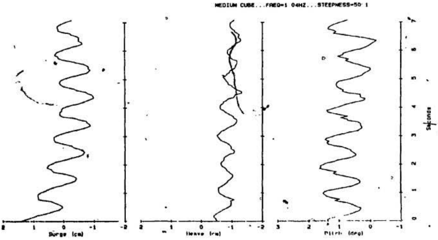
MEDIUM CUBE...FREQ=1 04HZ...STEEPNESS=50 1
Surge (cm)
Heave (cm)
Pitch (deg)
Seconds

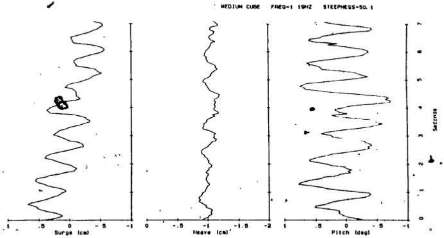
MEDIUM CUBE FREQ=1 19HZ STEEPNESS=50 1
Surge (cm)
Heave (cm)
Pitch (deg)
Seconds

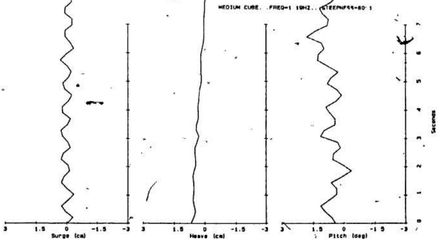
MEDIUM CUBE. .FREQ=1 19HZ.. STEEPNESS=80 1
Surge (cm)
Heave (cm)
Pitch (deg)
Seconds

MEDIUM CUBE. FREQ=1.19HZ .STEEPNESS=20:1

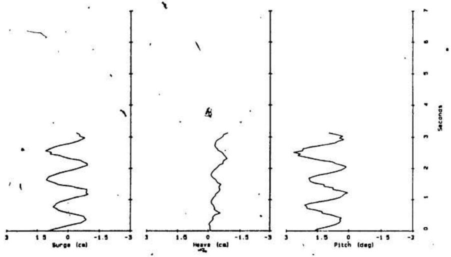

MEDIUM CUBE...FREQ=1.19HZ...STEEPNESS=40:1

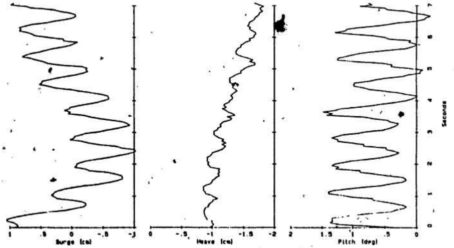

LARGE CUBE

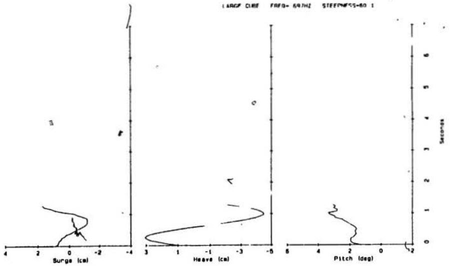
LARGE CUBE FREQ= .697HZ STEEPNESS=60.1
Surge (cm)
Heave (cm)
Pitch (deg)
Seconds

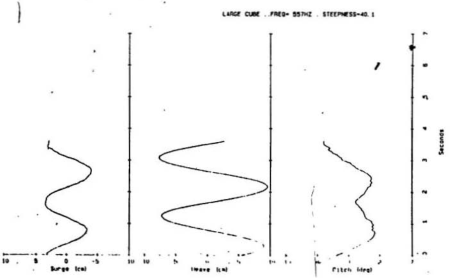
LARGE CUBE . FREQ= .557HZ . STEEPNESS=40.1
Surge (cm)
Heave (cm)
Pitch (deg)
Seconds

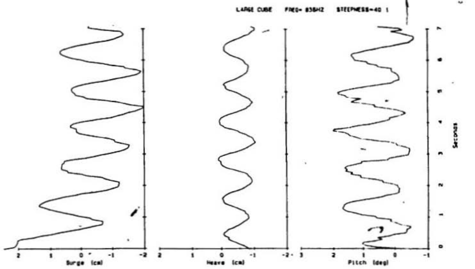
LARGE CUBE FREQ= 836HZ STEEPNESS=40 1
Surge (cm)
Heave (cm)
Pitch (deg)
Seconds

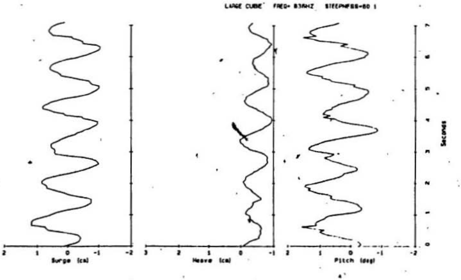
LARGE CUBE FREQ= 836HZ STEEPNESS=80 1
Surge (cm)
Heave (cm)
Pitch (deg)
Seconds

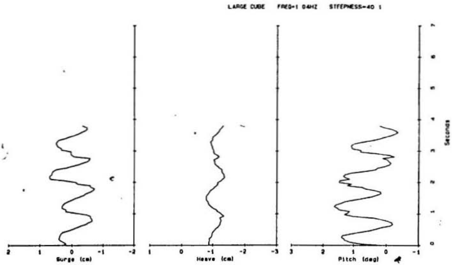
LARGE CUBE FREQ=1.04HZ STEEPNESS=40:1
Surge (cm)
Heave (cm)
Pitch (deg)
Seconds

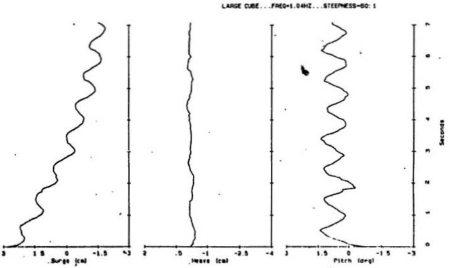
LARGE CUBE...FREQ=1.04HZ...STEEPNESS=60:1
Surge (cm)
Heave (cm)
Pitch (deg)
Seconds

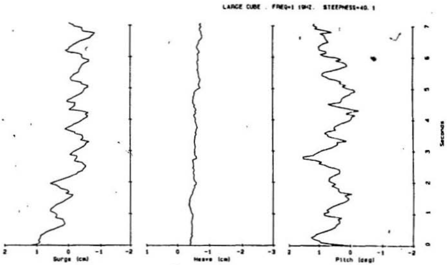
LARGE CUBE . FREQ=1.19HZ. STEEPNESS=40.1
Surge (cm)
Heave (cm)
Pitch (deg)
Seconds

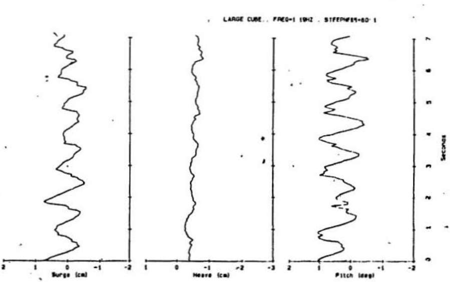
LARGE CUBE.. FREQ=1.19HZ . STEEPNESS=60.1
Surge (cm)
Heave (cm)
Pitch (deg)
Seconds

LARGE CUBE...IRR SEA (2)...HS=8.57CM

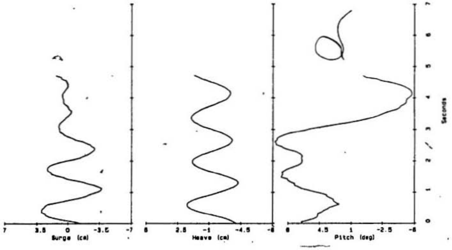

LARGE CUBE...IRR SEA (1)...HS=8.57CM

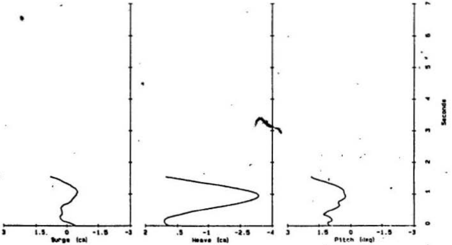

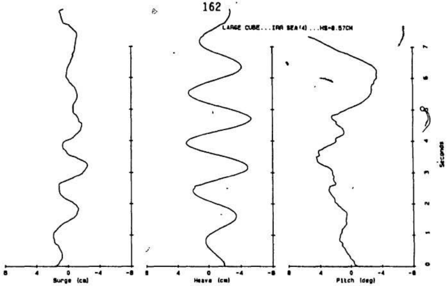
LARGE CUBE...IRR SEA(4)...HS=8.57CM
Surge (cm)
Heave (cm)
Pitch (deg)
Seconds

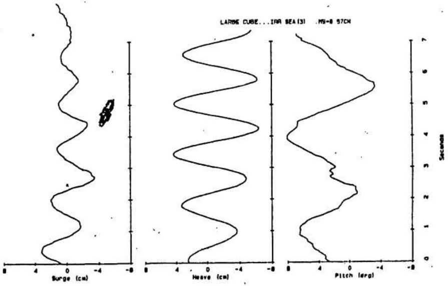
LARGE CUBE...IRR SEA(3) .HS=8.57CM
Surge (cm)
Heave (cm)
Pitch (deg)
Seconds

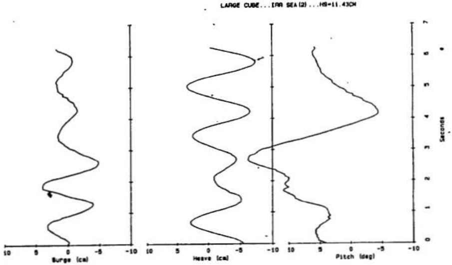
LARGE CUBE...IRR SEA(2)...HS=11.43CM
Surge (cm)
Heave (cm)
Pitch (deg)
Seconds
10 5 0 -5 -10
0 1 2 3 4 5 6 7

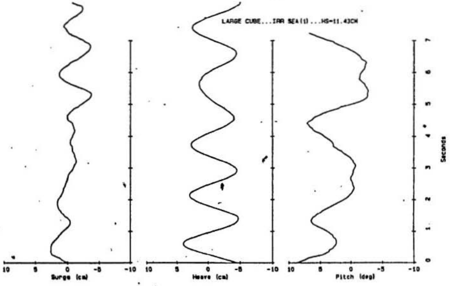
LARGE CUBE...IRR SEA(1)...HS=11.43CM
Surge (cm)
Heave (cm)
Pitch (deg)
Seconds
10 5 0 -5 -10
0 1 2 3 4 5 6 7

LARGE CUBE ...IRR SEA(3)...HS=11.43CM

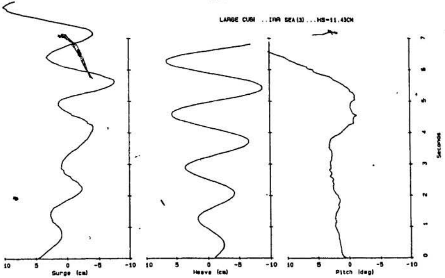

LARGE CUBE...IRR SEA(4)...HS=11.43CM

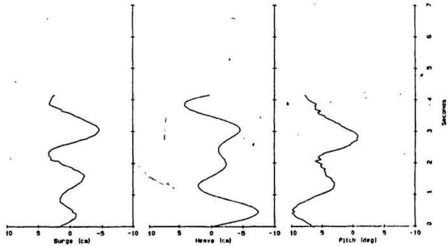

CYLINDER

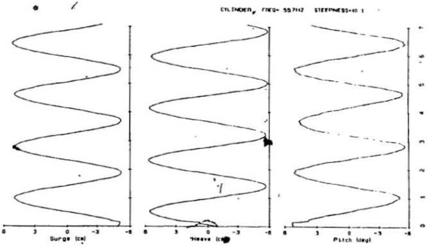
CYLINDER, FREQ= .557HZ STEEPNESS=40:1
Surge (cm)
Heave (cm)
Pitch (deg)
Seconds

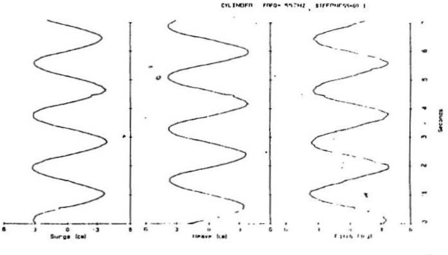
CYLINDER FREQ= .557HZ, STEEPNESS=60:1
Surge (cm)
Seconds

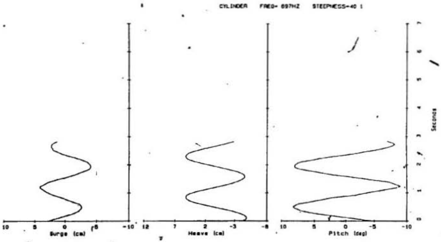
CYLINDER FREQ= 697HZ STEEPNESS=40 1
Surge (cm)
Heave (cm)
Pitch (deg)
Seconds

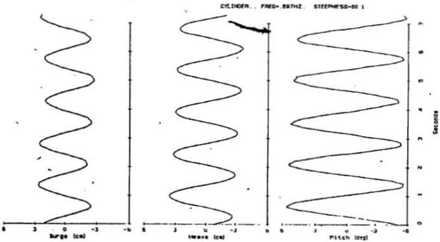
CYLINDER.. FREQ=.897HZ. STEEPNESS=60 1
Surge (cm)
Heave (cm)
Pitch (deg)
Seconds

CYLINDER FREQ= .836HZ STEEPNESS=40 1

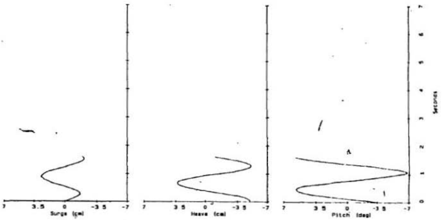

CYLINDER . FREQ= .836HZ STEEPNESS=60 1

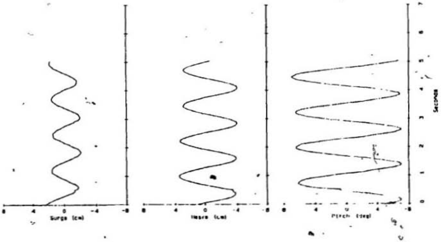

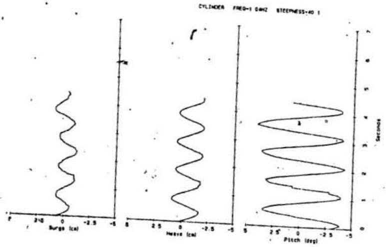
CYLINDER FREQ=1.04HZ STEEPNESS=40:1
Surge (cm)
Heave (cm)
Pitch (deg)
Seconds

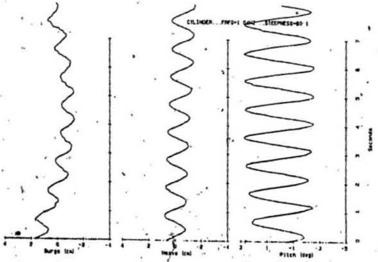
Surge (cm)
Heave (cm)
Pitch (deg)
Seconds

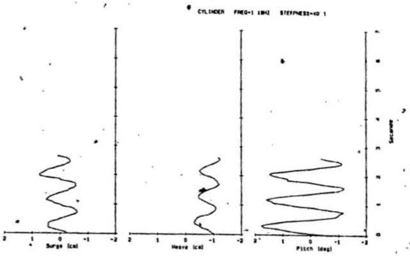
CYLINDER
Surge (cm)
Heave (cm)
Pitch (deg)
Seconds

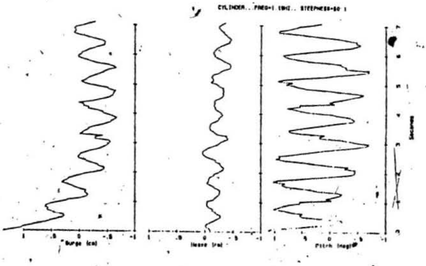
CYLINDER
Surge (cm)
Heave (cm)
Pitch (deg)
Seconds

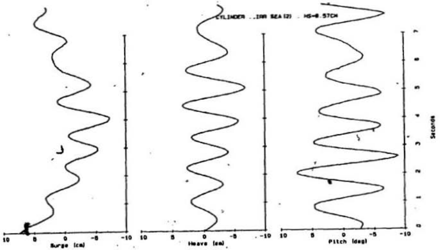
CYLINDER ..IRR SEA(2) . HS=8.57CM
Surge (cm)
Heave (cm)
Pitch (deg)
Seconds

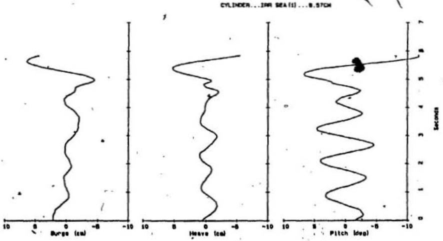
CYLINDER...IRR SEA(1)...8.57CM
Surge (cm)
Heave (cm)
Pitch (deg)
Seconds

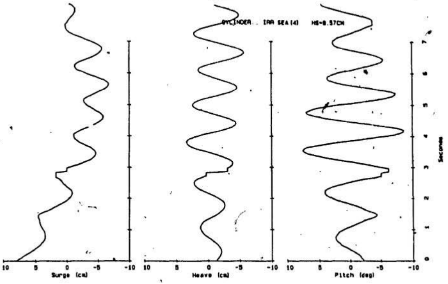
CYLINDER.. IRR SEA (4) HS=8.57CM
Surge (cm)
Heave (cm)
Pitch (deg)
Seconds

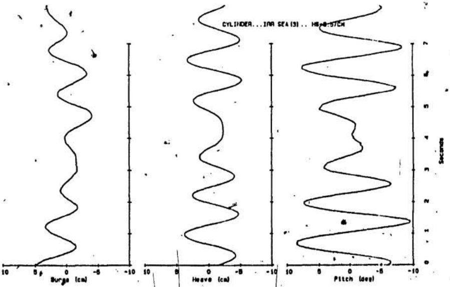
CYLINDER...IRR SEA (3).. HS=8.57CM
Surge (cm)
Heave (cm)
Pitch (deg)
Seconds

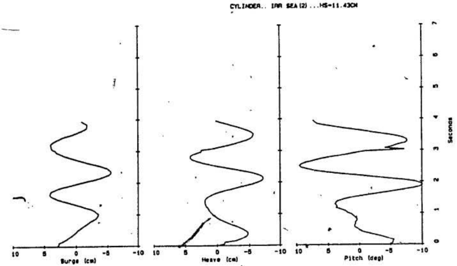
CYLINDER.. IRR SEA(2)...HS=11.43CM
10 5 0 -5 -10
Surge (cm)
10 5 0 -5 -10
Heave (cm)
10 5 0 -5 -10
Pitch (deg)
0 1 2 3 4 5 6 7
Seconds

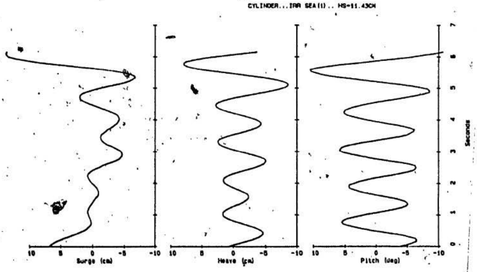
CYLINDER...IRR SEA(1).. HS=11.43CM
10 5 0 -5 -10
Surge (cm)
10 5 0 -5 -10
Heave (cm)
10 5 0 -5 -10
Pitch (deg)
0 1 2 3 4 5 6 7
Seconds

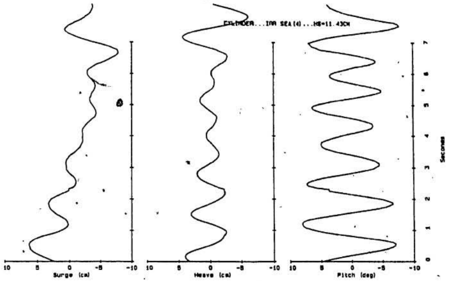
CYLINDER...IRR SEA(4)...HS=11.43CM
Surge (cm)
Heave (cm)
Pitch (deg)
Seconds

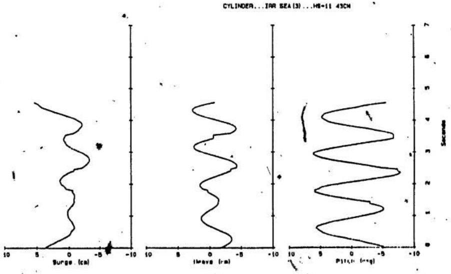
CYLINDER...IRR SEA(3)...HS=11.43CM
Surge (cm)
Heave (cm)
Pitch (deg)
Seconds

CYLINDER ..IRR SEA(2) .HS-14 29CM

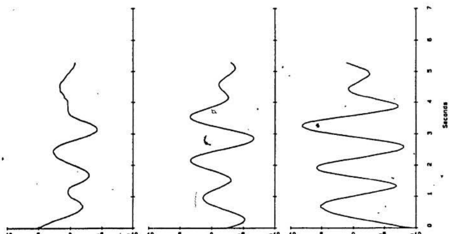

CYLINDER...IRR SEA(1)...HS-14.29CM

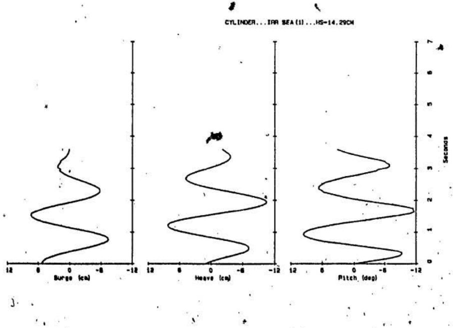

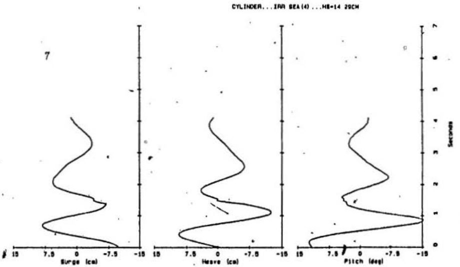
CYLINDER...IRR SEA(4)...HS=14 29CM
7
15
7.5
0
-7.5
-15
Surge (cm)
Heave (cm)
Pitch (deg)
Seconds
0
1
2
3
4
5
6
7

TRAPEZOID

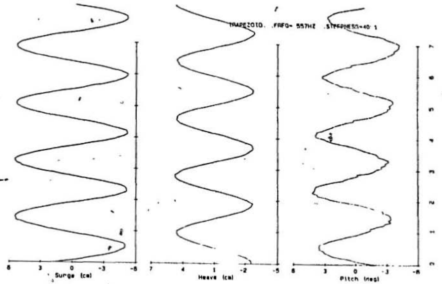
TRAPEZOID
Surge (cm)
Heave (cm)
Pitch (deg)
Seconds

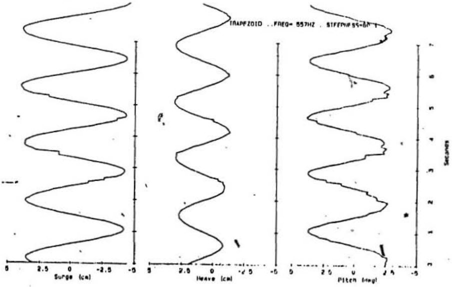
TRAPEZOID
Surge (cm)
Heave (cm)
Pitch (deg)
Seconds

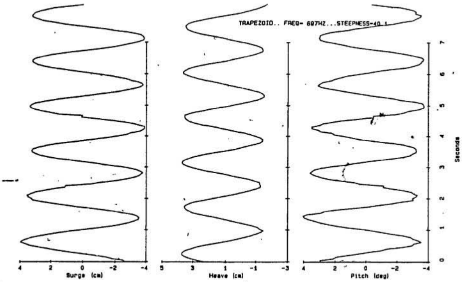

TRAPEZOID.. FREQ= .697HZ...STEEPNESS=40:1
Surge (cm)
Heave (cm)
Pitch (deg)
Seconds

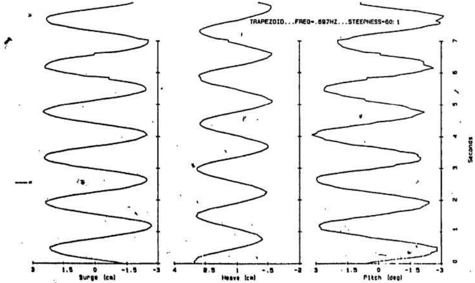

TRAPEZOID...FREQ=.697HZ...STEEPNESS=60:1
Surge (cm)
Heave (cm)
Pitch (deg)
Seconds

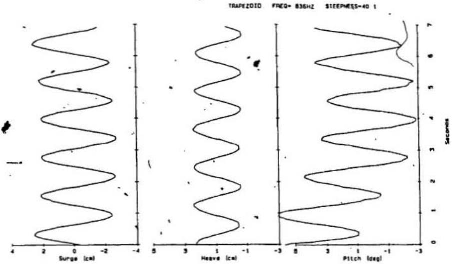
TRAPEZOID FREQ= 836HZ STEEPNESS=40 1
Surge (cm)
Heave (cm)
Pitch (deg)
Seconds

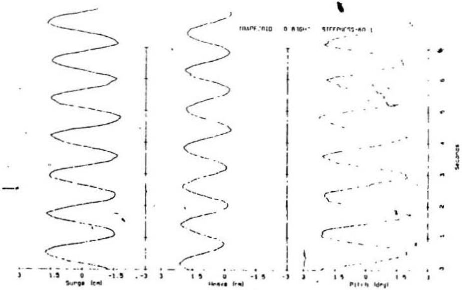
Surge (cm)
Heave (cm)
Pitch (deg)
Seconds

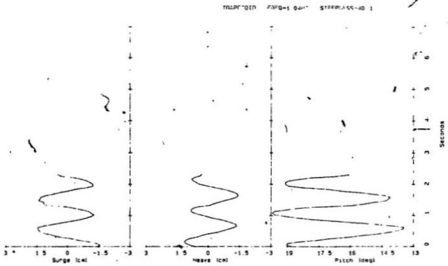
Surge (cm)
Heave (cm)
Pitch (deg)
Seconds

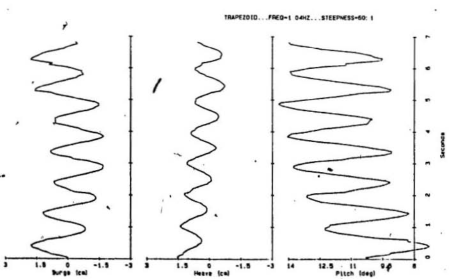
TRAPEZOID...FREQ=1 04HZ...STEEPNESS=60: 1
Surge (cm)
Heave (cm)
Pitch (deg)
Seconds

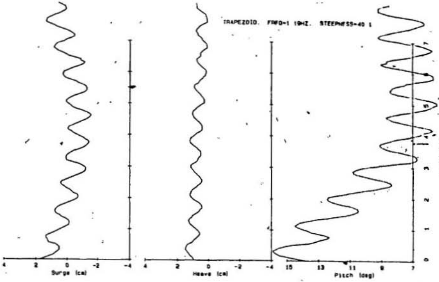
TRAPEZOID. FREQ=1 19HZ. STEEPNESS=40 1
Surge (cm)
Heave (cm)
Pitch (deg)
Seconds

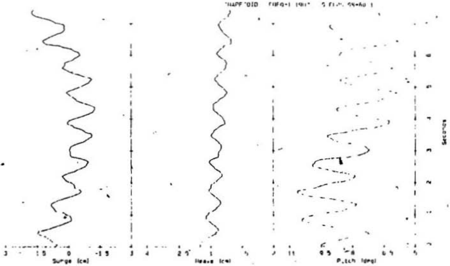
Surge (cm)
Heave (cm)
Pitch (deg)
Seconds

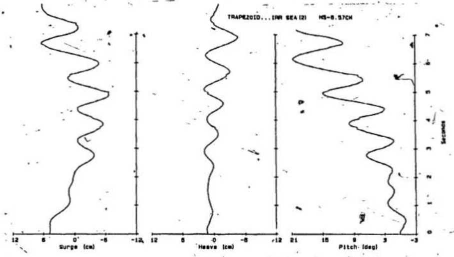
TRAPEZOID...IRR SEA (2) HS=8.57CM
Surge (cm)
Heave (cm)
Pitch (deg)
Seconds

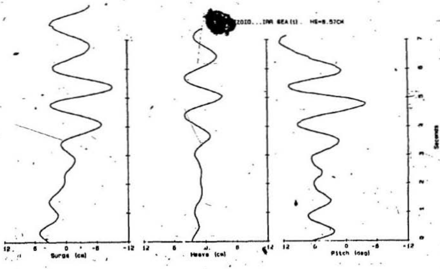
ZOID...IRR SEA (1) HS=8.57CM
Surge (cm)
Heave (cm)
Pitch (deg)
Seconds

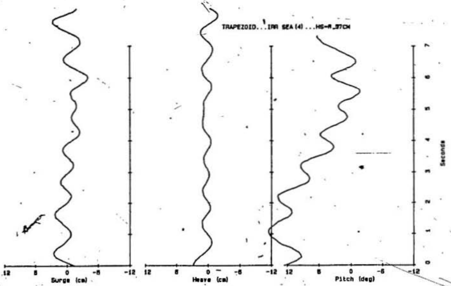
TRAPEZOID...IRR SEA (4)...
12 6 0 -6 -12
Surge (cm)
12 6 0 -6 -12
Heave (cm)
12 6 0 -6 -12
Pitch (deg)
Seconds
0 1 2 3 4 5 6 7

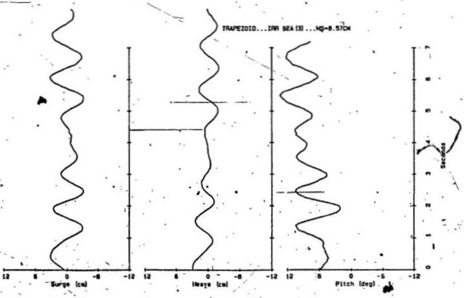
TRAPEZOID...IRR SEA (3)...HS=8.57CM
12 6 0 -6 -12
Surge (cm)
12 6 0 -6 -12
Heave (cm)
12 6 0 -6 -12
Pitch (deg)
Seconds
0 1 2 3 4 5 6 7

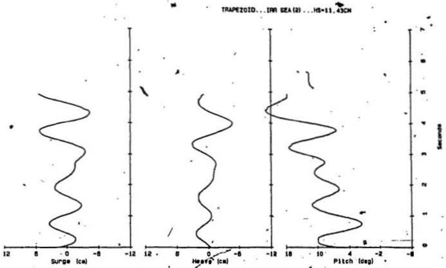
TRAPEZOID...IRR SEA(2)...HS=11.43CM
Surge (cm)
Heave (cm)
Pitch (deg)
Seconds

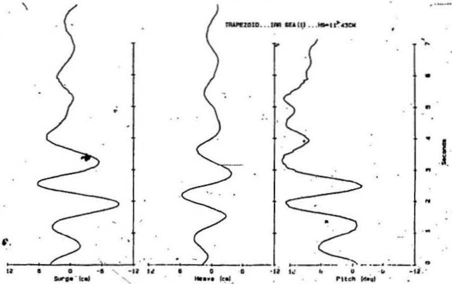
TRAPEZOID...IRR SEA(1)...HS=11.43CM
Surge (cm)
Heave (cm)
Pitch (deg)
Seconds

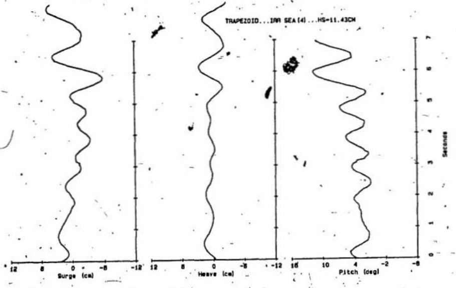
TRAPEZOID...IRR SEA(4)...HS=11.43CM
12 8 0 -8 -12
Surge (cm)
12 8 0 -8 -12
Heave (cm)
16 10 4 -2 -8
Pitch (deg)
0 1 2 3 4 5 6 7
Seconds

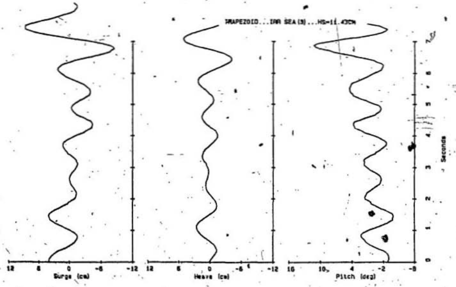
TRAPEZOID...IRR SEA(3)...HS=11.43CM
12 8 0 -8 -12
Surge (cm)
12 8 0 -8 -12
Heave (cm)
16 10 4 -2 -8
Pitch (deg)
0 1 2 3 4 5 6 7
Seconds

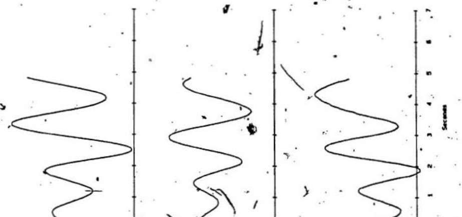
TRAPEZOID...IRR SEA(2)...HS=14.29CM
Surge (cm)
Heave (cm)
Pitch (deg)
Seconds

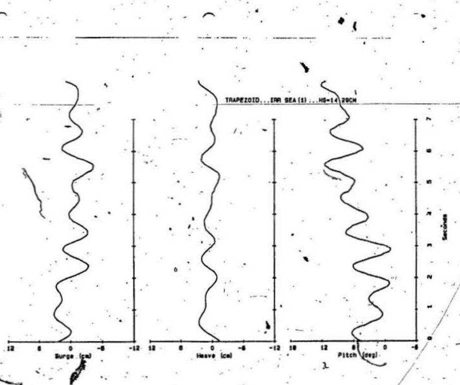
TRAPEZOID...IRR SEA(1)...HS=14.29CM
Surge (cm)
Heave (cm)
Pitch (deg)
Seconds

TRAPEZOID...IRR SEA(3)...HS=14.29CM

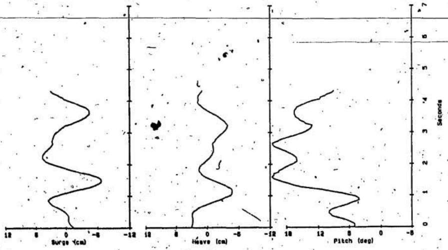

SPHERE

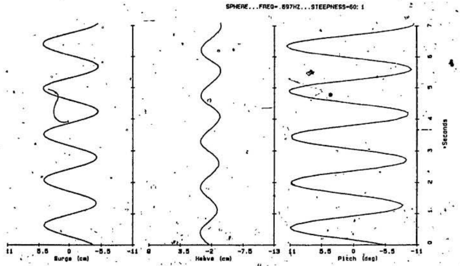
SPHERE...FREQ=.897HZ...STEEPNESS=60: 1
Surge (cm)
Heave (cm)
Pitch (deg)
Seconds

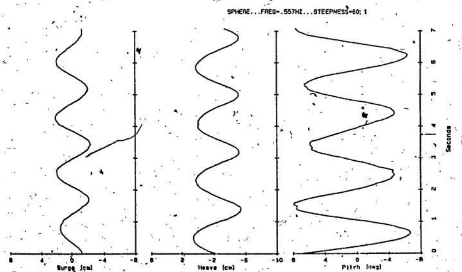
SPHERE...FREQ=.557HZ...STEEPNESS=60: 1
Surge (cm)
Heave (cm)
Pitch (deg)
Seconds

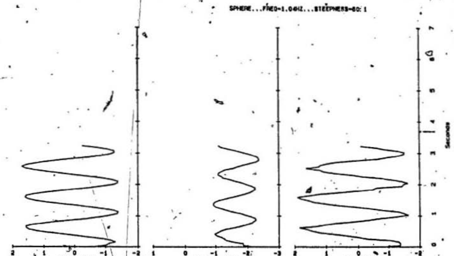

SPHERE...FREQ=1.04HZ...STEEPNESS=60:1
Surge (cm)
Heave (cm)
Pitch (deg)
Seconds

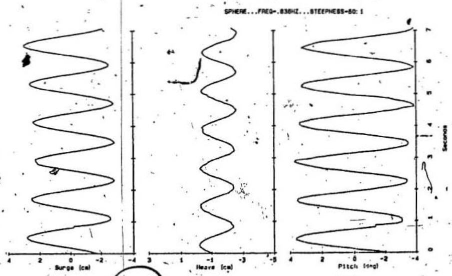

SPHERE...FREQ=.838HZ...STEEPNESS=60:1
Surge (cm)
Heave (cm)
Pitch (deg)
Seconds

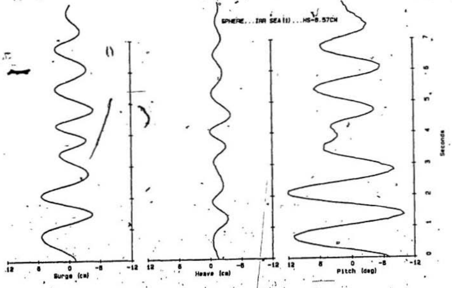
SPHERE...IRR SEA(1)...HS=8.57CM
Surge (cm)
Heave (cm)
Pitch (deg)
Seconds

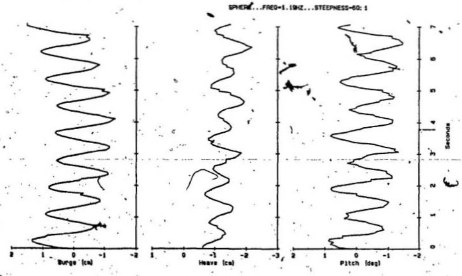
SPHERE...FREQ=1.19HZ...STEEPNESS=60:1
Surge (cm)
Heave (cm)
Pitch (deg)
Seconds

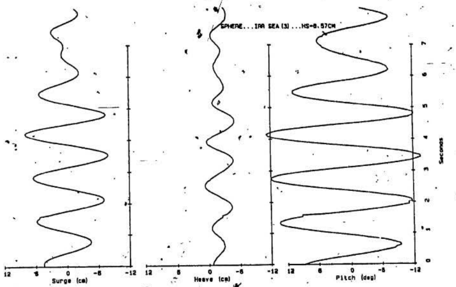
SPHERE...IRR SEA (3)...HS=8.57CM
Surge (cm)
Heave (cm)
Pitch (deg)
Seconds

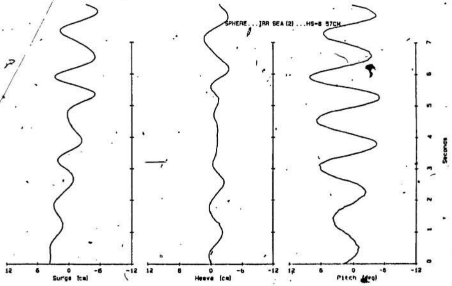
SPHERE...IRR SEA (2)...HS=8.57CM
Surge (cm)
Heave (cm)
Pitch (deg)
Seconds

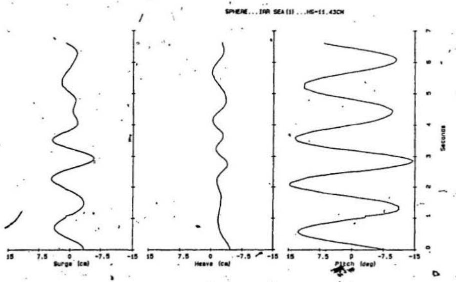
SPHERE...IRR SEA(1)...HS=11.43CM
Surge (cm)
Heave (cm)
Pitch (deg)
Seconds

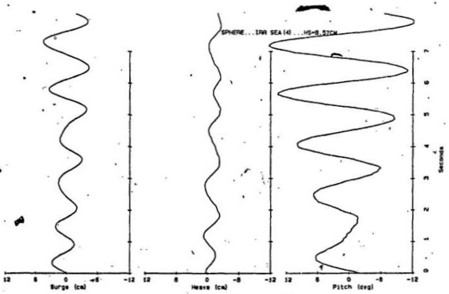
SPHERE...IRR SEA(4)...HS=8.57CM
Surge (cm)
Heave (cm)
Pitch (deg)
Seconds

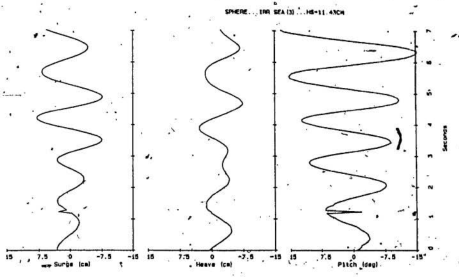
SPHERE...IRR SEA (3)...HS=11.43CM
15
7.5
0
-7.5
-15
Surge (cm)
Heave (cm)
Pitch (deg)
Seconds
0
1
2
3
4
5
6
7

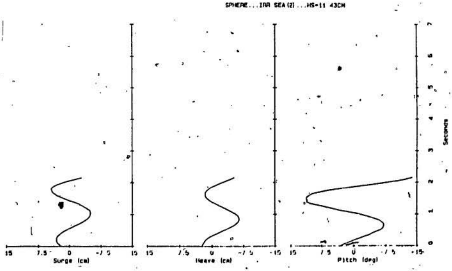
SPHERE...IRR SEA (2)...HS=11.43CM
15
7.5
0
-7.5
-15
Surge (cm)
Heave (cm)
Pitch (deg)
Seconds
0
1
2
3
4
5
6
7

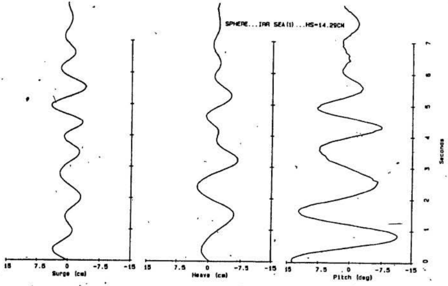
SPHERE...IRR SEA(1)...HS=14.29CM
15
7.5
0
-7.5
-15
Surge (cm)
Heave (cm)
Pitch (deg)
0
1
2
3
4
5
6
7
Seconds

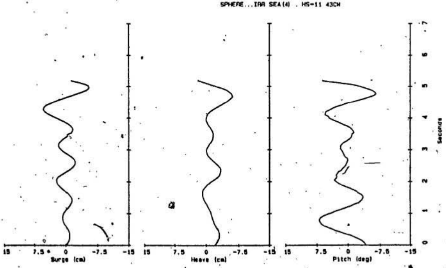
SPHERE...IRR SEA(4) . HS=11 43CM
15
7.5
0
-7.5
-15
Surge (cm)
Heave (cm)
Pitch (deg)
0
1
2
3
4
5
6
7
Seconds

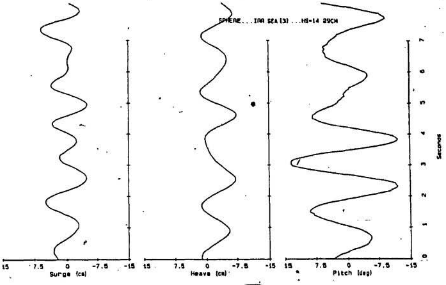
SPHERE...IRR SEA (3)...HS=14 29CM
15 7.5 0 -7.5 -15
Surge (cm)
15 7.5 0 -7.5 -15
Heave (cm)
15 7.5 0 -7.5 -15
Pitch (deg)
0 1 2 3 4 5 6 7
Seconds

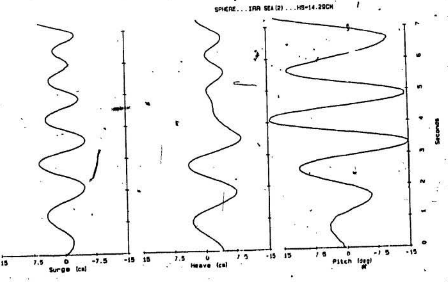
SPHERE...IRR SEA (2)...HS=14.29CM
15 7.5 0 -7.5 -15
Surge (cm)
Heave (cm)
Pitch (deg)
0 1 2 3 4 5 6 7
Seconds

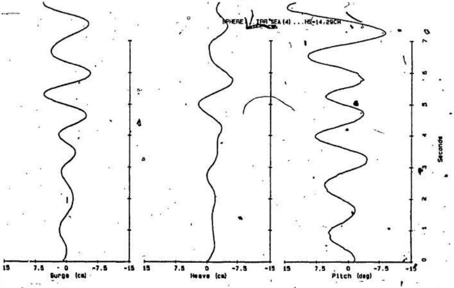
SEA (4) ... HS=14.29CM
15 7.5 0 -7.5 -15
Surge (cm)
15 7.5 0 -7.5 -15
Heave (cm)
15 7.5 0 -7.5 -15
Pitch (deg)
0 1 2 3 4 5 6 7
Seconds

APPENDIX 3

WAVE RECORDS

SMALL CUBE

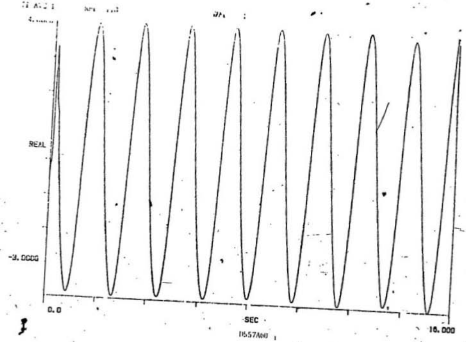

D557A60

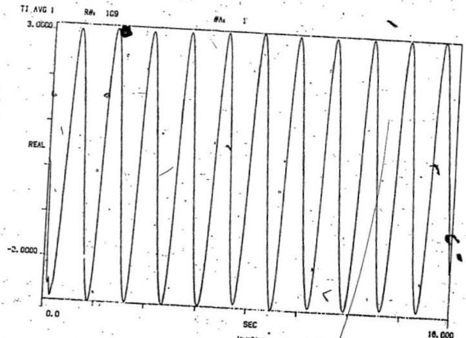

D097A60

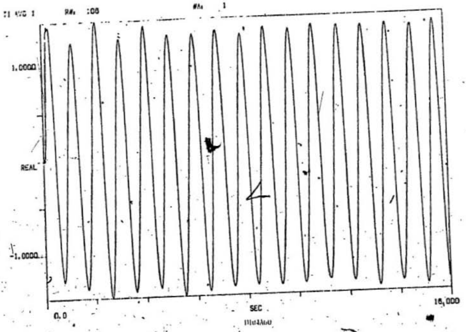
TI AVG 1
R#: 108
#A: 1
1.0000
REAL
-1.0000
0.0
SEC
16.000

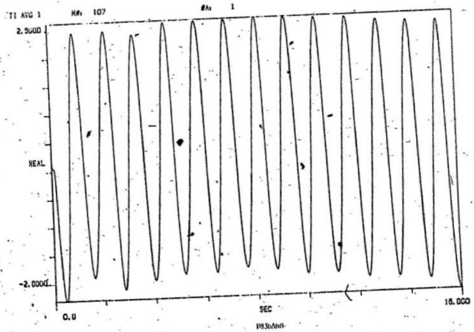
TI AVG 1
R#: 107
#A: 1
2.5000
REAL
-2.0000
0.0
SEC
16.000

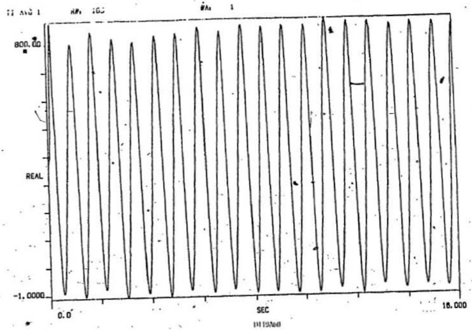
800.00
REAL
-1.0000
0.0
SEC
16.000

MEDIUM CUBE

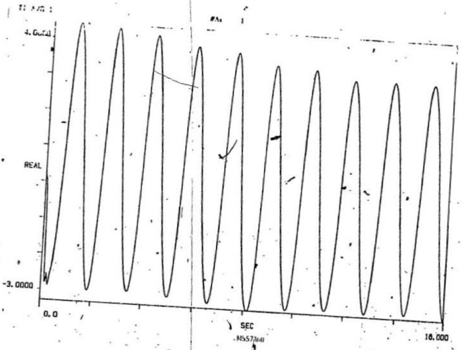
TI AVG 1
#A: 1
4.0000
REAL
-3.0000
0.0
SEC
16.000

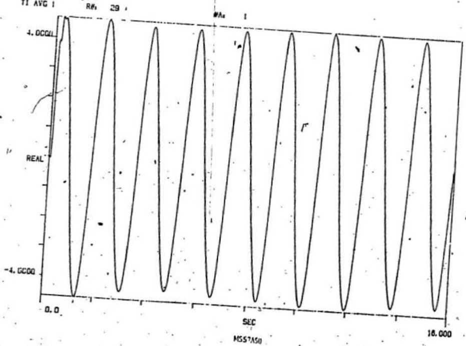
TI AVG 1
R#: 29
#A: 1
4.0000
REAL
-4.0000
0.0
SEC
16.000

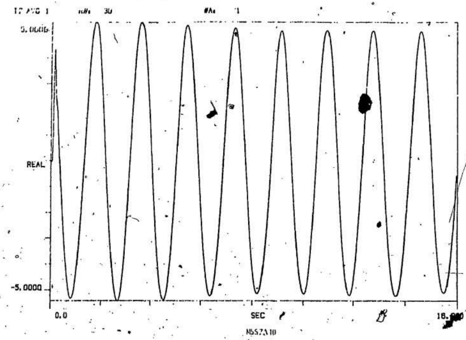
5.0000
REAL
-5.0000
0.0
SEC
16.000
N557A10

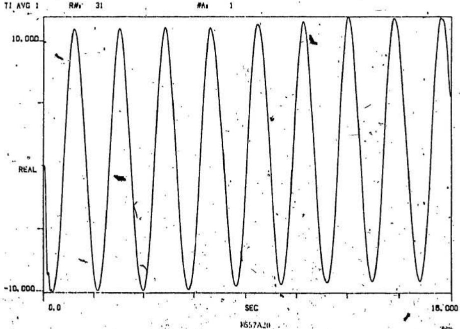
TI AVG 1
R#: 31
#A: 1
10.000
REAL
-10.000
0.0
SEC
16.000
N557A20

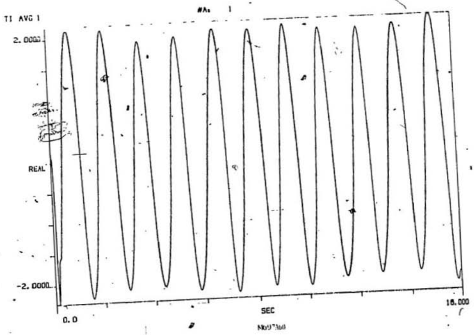
#A: 1
TI AVG 1
2.0000
REAL
-2.0000
0.0
SEC
16.000

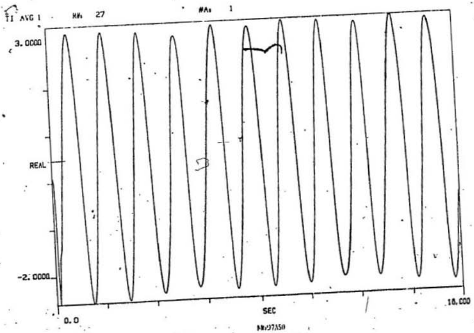
TI AVG 1
R#: 27
#A: 1
3.0000
REAL
-2.0000
0.0
SEC
16.000

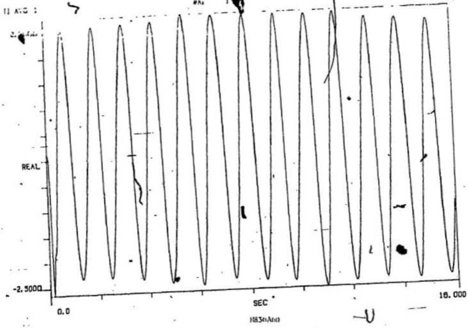
TI AVG 1
#A: 1
REAL
-2.5000
0.0
SEC
16.000
N836A60

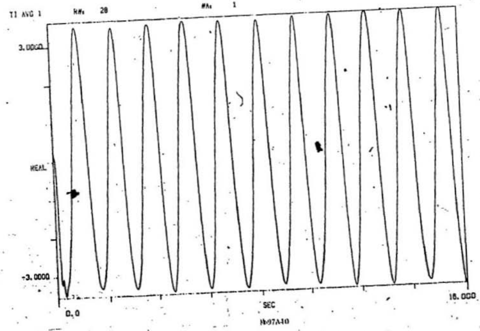
TI AVG 1
R#: 28
#A: 1
3.0000
REAL
-3.0000
0.0
SEC
16.000
N97A40

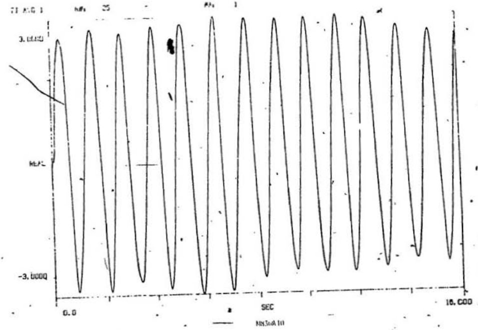
TI AVG 1
R#: 25
#A: 1
3.0000
REAL
-3.0000
0.0
SEC
16.000
NB36A10

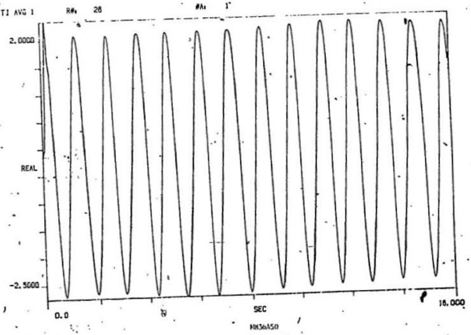
TI AVG 1
R#: 28
#A: 1
2.0000
REAL
-2.5000
0.0
SEC
16.000
NB36A50

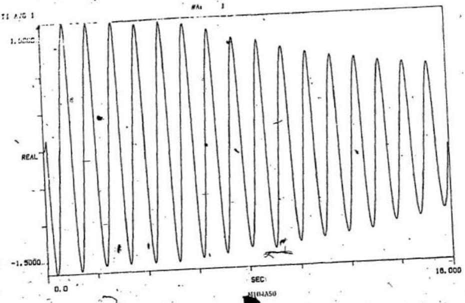
#A: 1
TI AVG 1
1.5000
REAL
-1.5000
0.0
SEC
16.000
M104A50

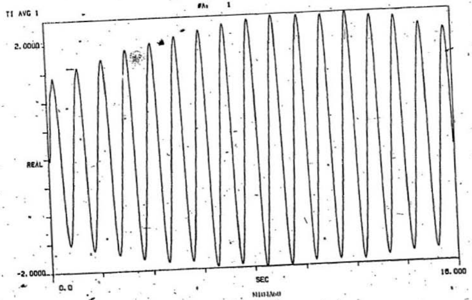
#A: 1
TI AVG 1
2.0000
REAL
-2.0000
0.0
SEC
16.000
M104A60

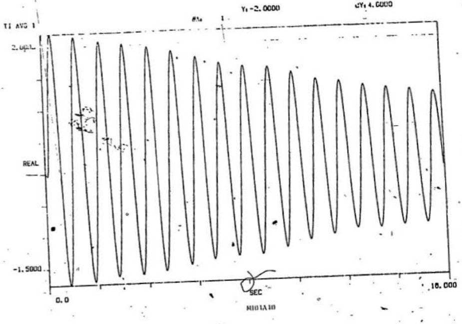
Y: -2.0000
dY: 4.0000
#A: 1
TI AVG 1
2.0000
REAL
-1.5000
0.0
SEC
16.000
M101A10

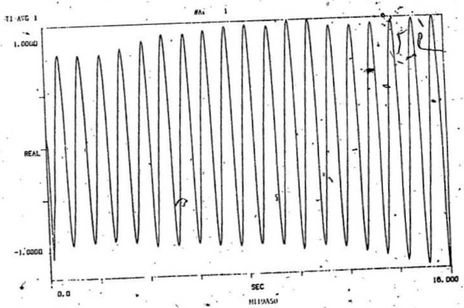
#A: 1
TI AVG 1
1.0000
REAL
-1.0000
0.0
SEC
16.000
M119A50

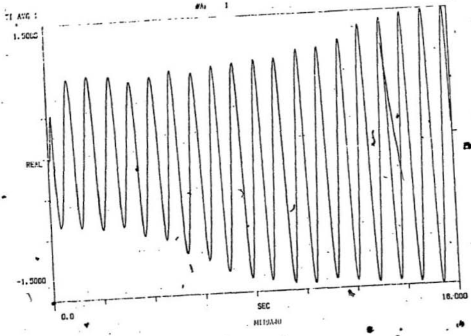
TI AVG 1
#A: 1
1.5000
REAL
-1.5000
0.0
SEC
16.000
MI19A40

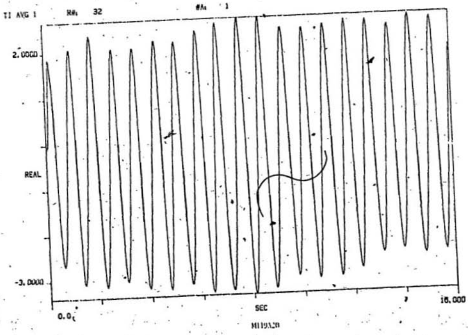
TI AVG 1
R#: 32
#A: 1
2.0000
REAL
-3.0000
0.0
SEC
16.000
MI19A20

LARGE CUBE

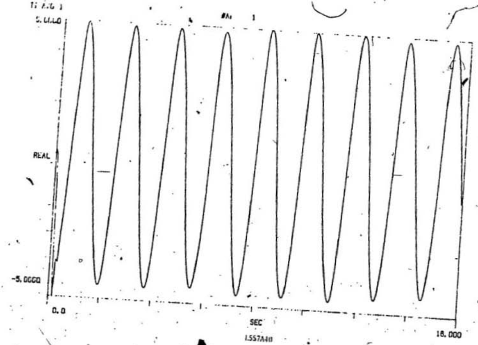
REAL
-5.0000
0.0
SEC
18.000

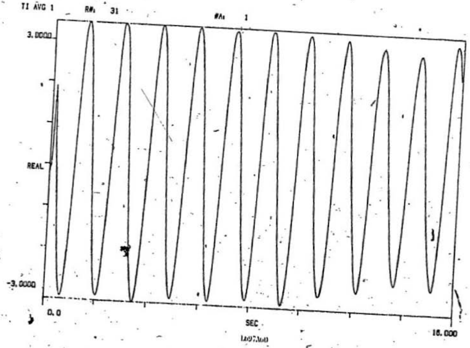
TI AVG 1
R#: 31
#A: 1
3.0000
REAL
-3.0000
0.0
SEC
18.000

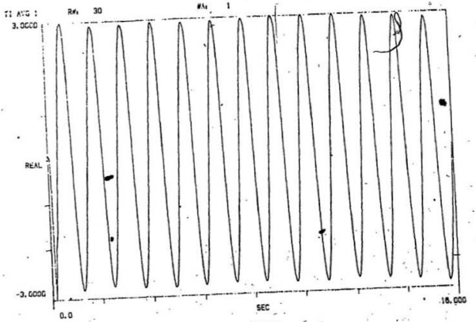
TI AVG 1
R#: 30
#A: 1
3.0000
REAL
-3.0000
0.0
SEC
16.000

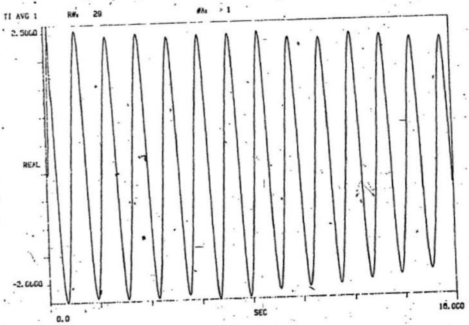
TI AVG 1
R#: 29
#A: 1
2.5000
REAL
-2.0000
0.0
SEC
16.000

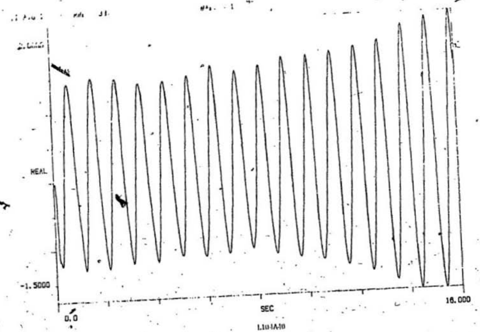

1.1014A-10

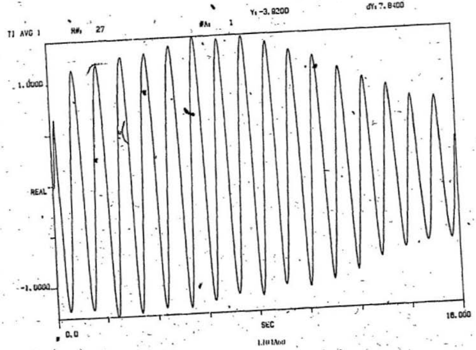

1.1014A60

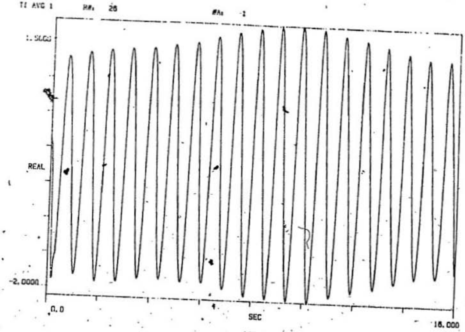

L119A40

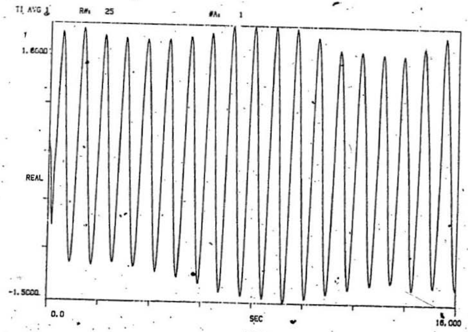

L119A60

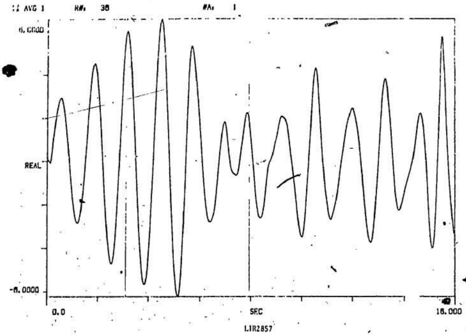
AVG 1
R#: 38
#A: 1
6.0000
REAL
-6.0000
0.0
SEC
16.000
LIR2857

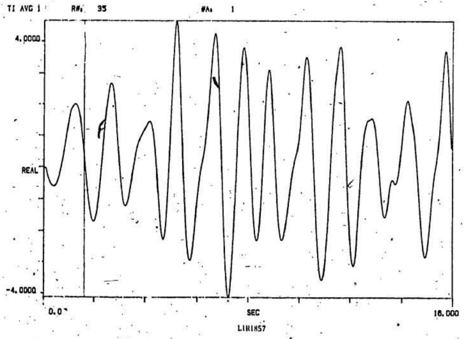
TI AVG 1
R#: 35
#A: 1
4.0000
REAL
-4.0000
0.0
SEC
16.000
LIR1857

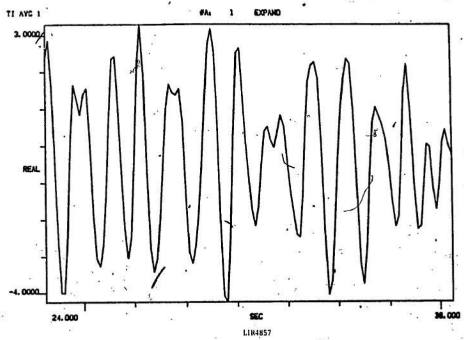
TI AVG 1
#A: 1 EXPAND
3.0000
REAL
-4.0000
24.000
SEC
36.000
LIR4857

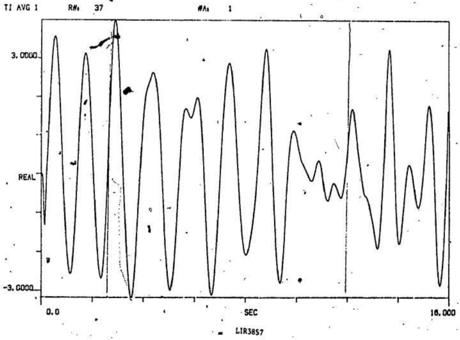
TI AVG 1
R#: 37
#A: 1
3.0000
REAL
-3.0000
0.0
SEC
16.000
LIR3857

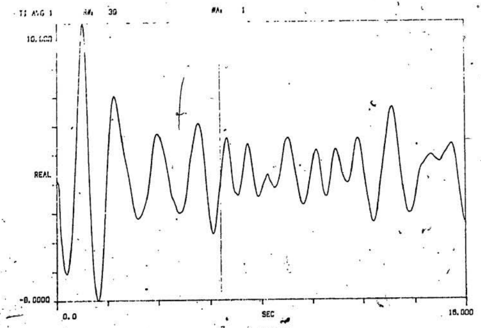

LIR21143

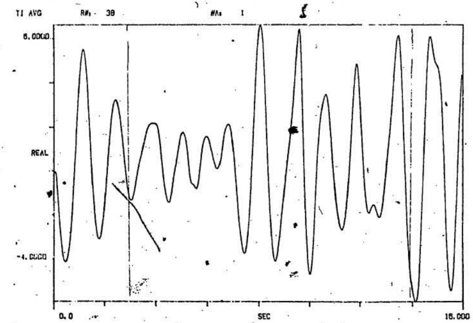

LIR11143

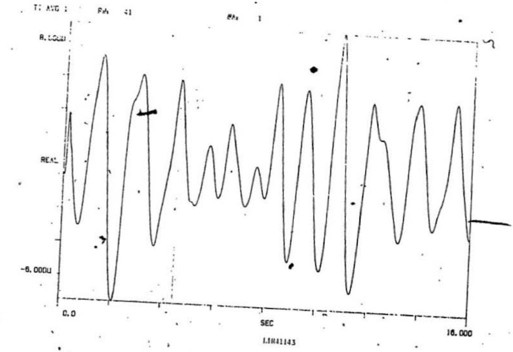
R#: 41
#A: 1
REAL
0.0
SEC
16.000
LIR41143

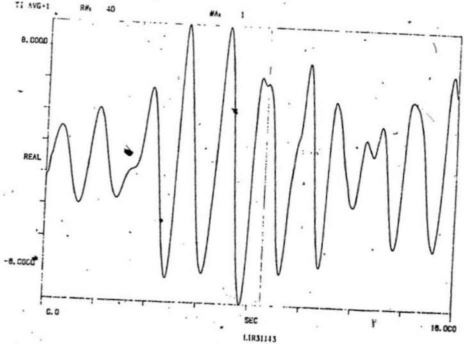
TI AVG+1
R#: 40
#A: 1
8.0000
REAL
-8.0000
0.0
SEC
16.000
LIR31143

CYLINDER

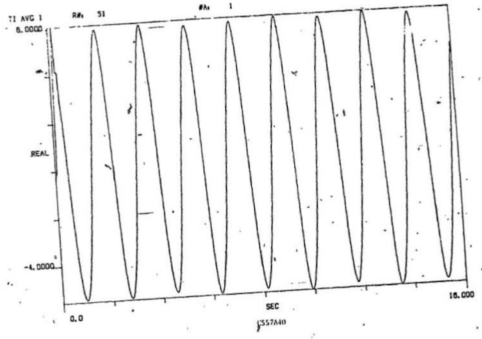
TI AVG 1
R#: 51
#A: 1
6.0000
REAL
-4.0000
0.0
SEC
16.000
CSS7A40

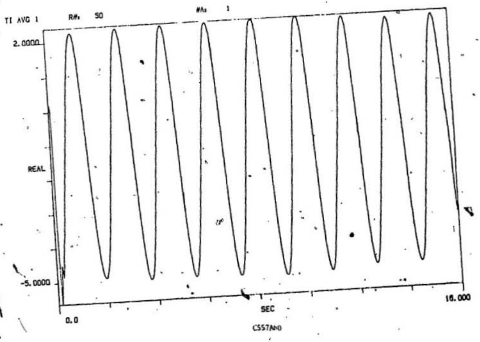
TI AVG 1
R#: 50
#A: 1
2.0000
REAL
-5.0000
0.0
SEC
16.000
CSS7A60

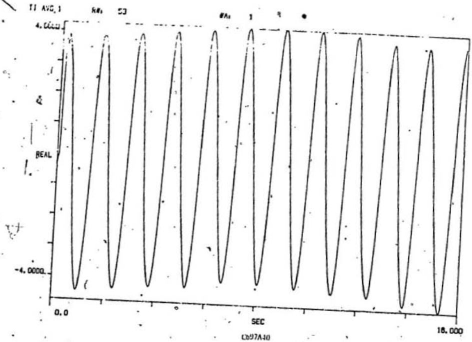

Cb97A40

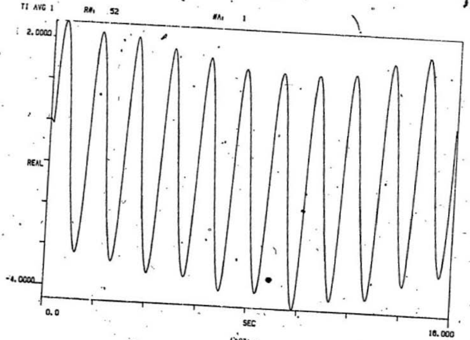

Cb97A60

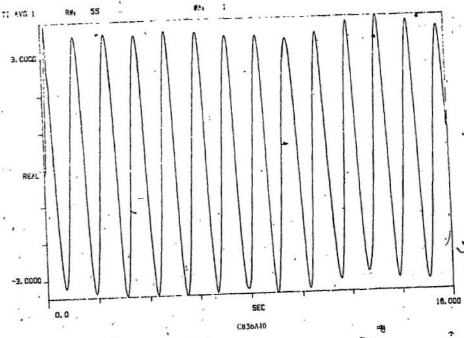
TI AVG 1
R#: 55
#A: 1
3.0000
REAL
-3.0000
0.0
SEC
16.000
C836A40

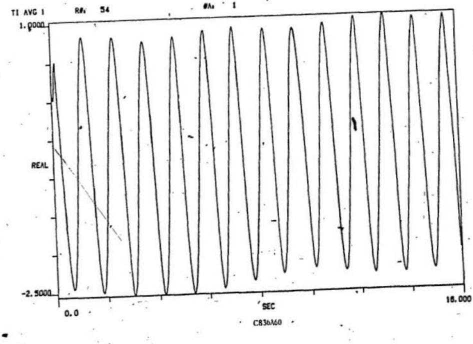
TI AVG 1
R#: 54
#A: 1
1.0000
REAL
-2.5000
0.0
SEC
16.000
C836A60

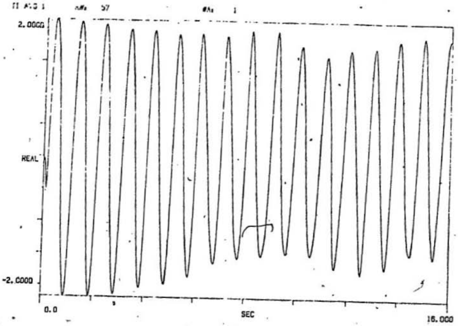

C104A40

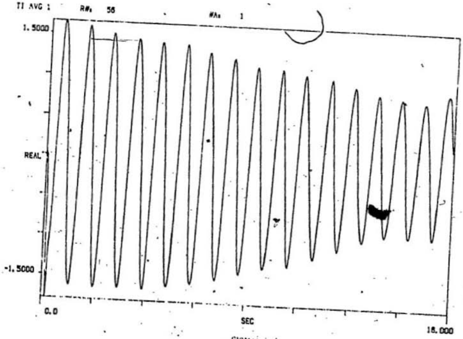

C104A60

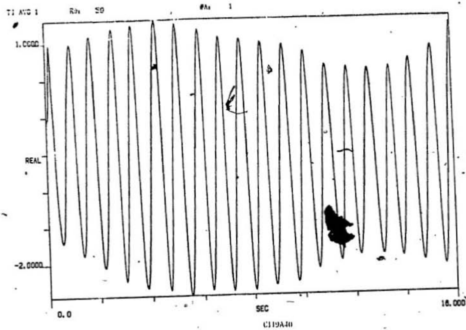

C119A40

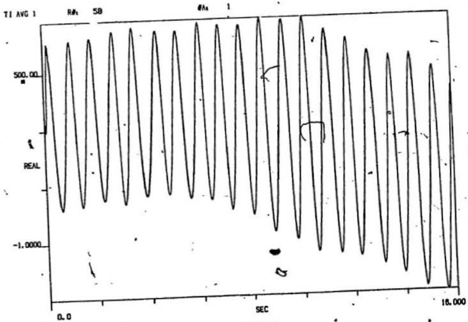

C119A60

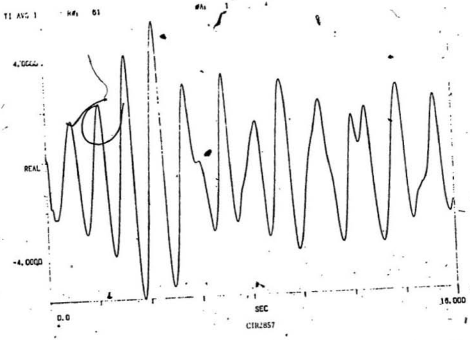
TI AVG 1
R#: 61
#A: 1
4.0000
REAL
-4.0000
0.0
SEC
16.000
CIR2857

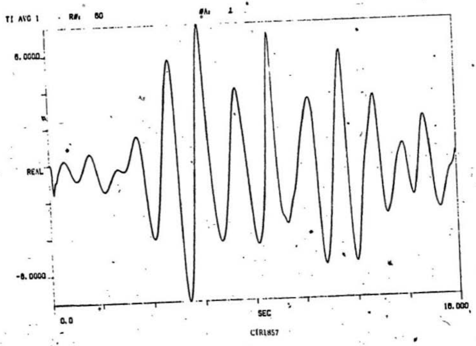
TI AVG 1
R#: 60
#A: 1
8.0000
REAL
-8.0000
0.0
SEC
16.000
CIR1857

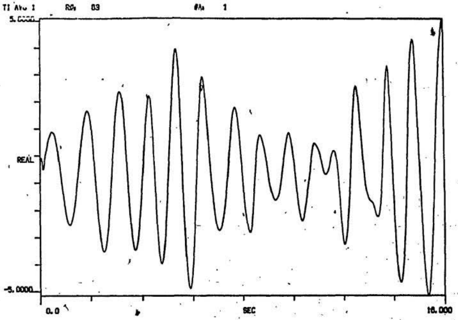

CIR4857

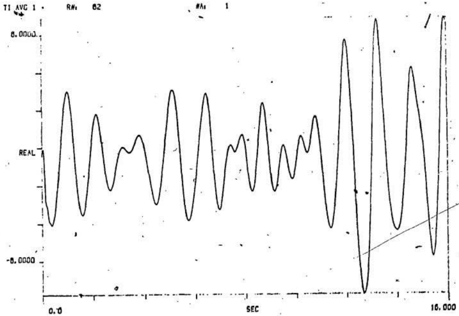

CIR3857

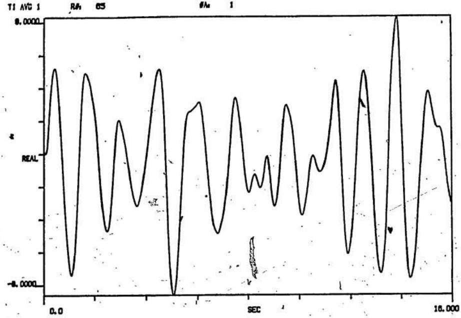

CIR21143

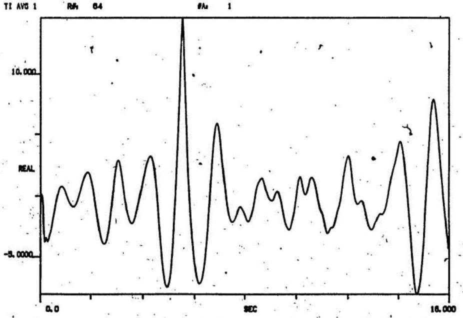

CIR11143

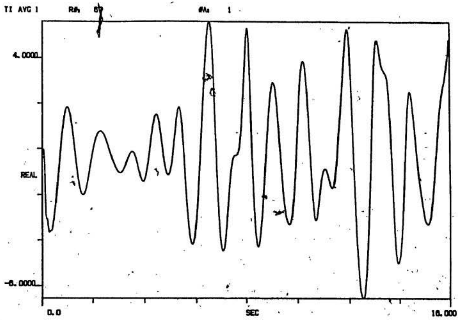

CIR41143

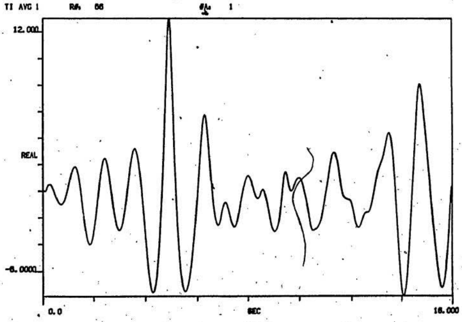

CIR31143

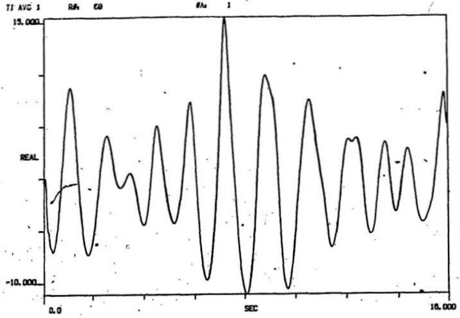

CIR11429

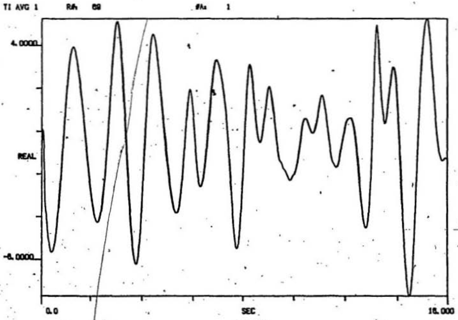

CIR21429

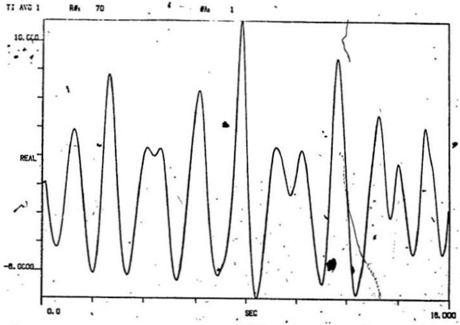

CIR31429

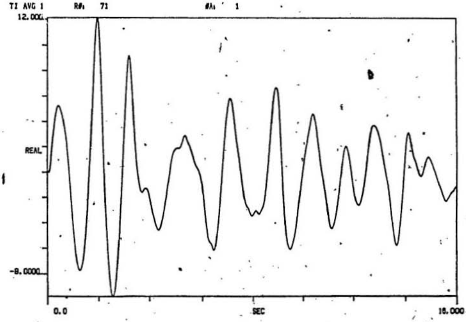

CIR41429

TRAPEZOID

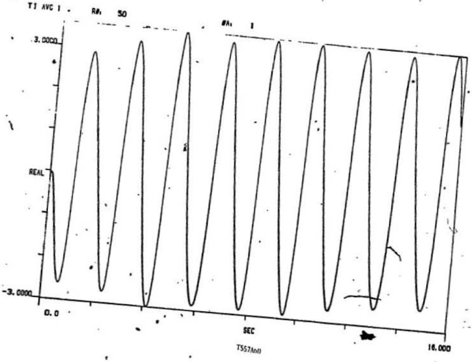
TI AVG 1
R#: 50
#A: 1
3.0000
REAL
-3.0000
0.0
SEC
10.000
T557A60

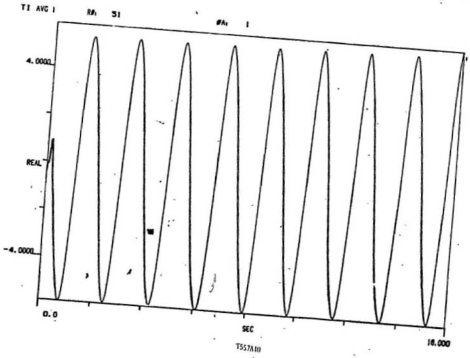
TI AVG 1
R#: 51
#A: 1
4.0000
REAL
-4.0000
0.0
SEC
10.000
T557A10

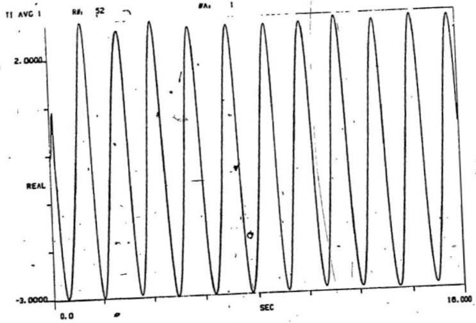

T697A60

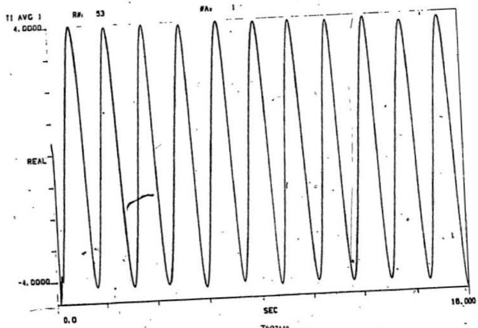

T697A40

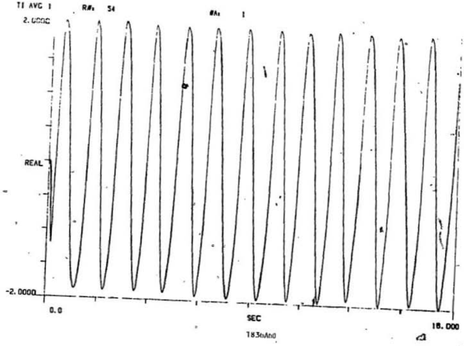
TI AVG 1
R#: 54
#A: 1
2.0000
REAL
-2.0000
0.0
SEC
16.000
T836A40

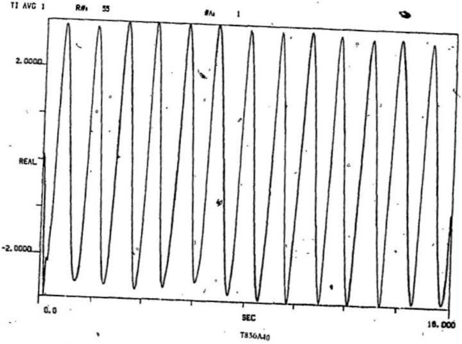
TI AVG 1
R#: 55
#A: 1
2.0000
REAL
-2.0000
0.0
SEC
16.000
T836A40

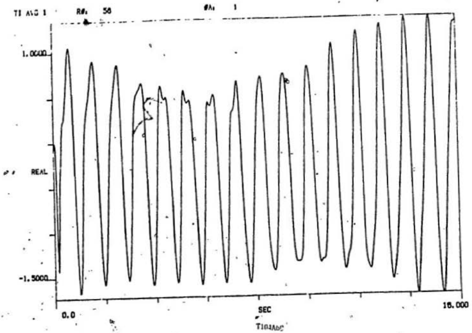
TI AVG 1
R#: 56
#A: 1
1.0000
REAL
-1.5000
0.0
SEC
16.000

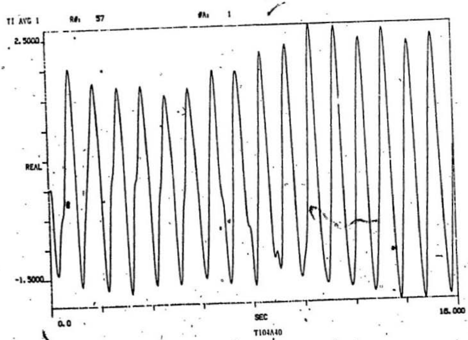
TI AVG 1
R#: 57
#A: 1
2.5000
REAL
-1.5000
0.0
SEC
16.000
T104A40

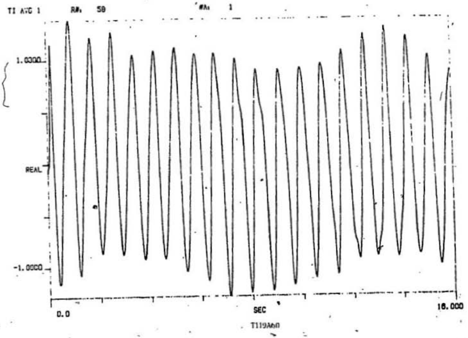
TI AVG 1
R#: 58
#A: 1
1.0000
REAL
-1.0000
0.0
SEC
16.000
T119A60

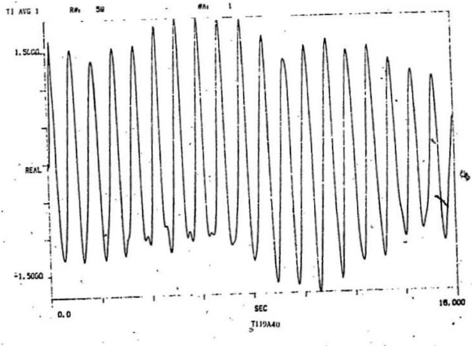
TI AVG 1
R#: 58
#A: 1
1.5000
REAL
-1.5000
0.0
SEC
16.000
T119A40

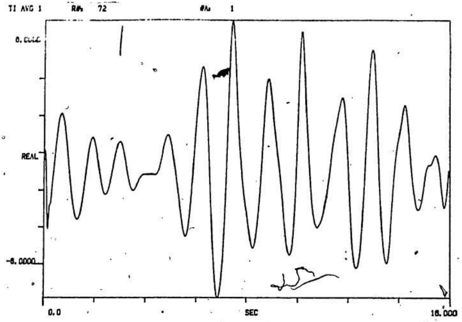

TIR1857

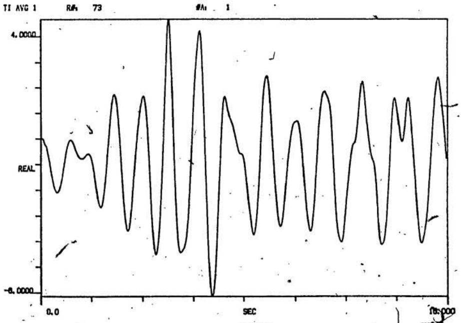

TIR2857

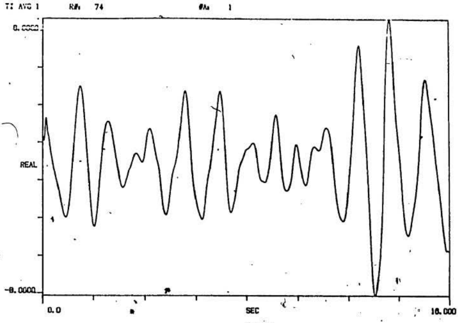

TIR3857

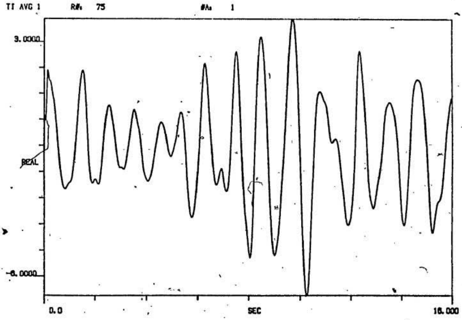

TIR4857

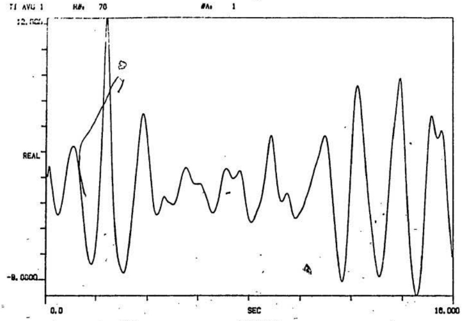

TIR11143

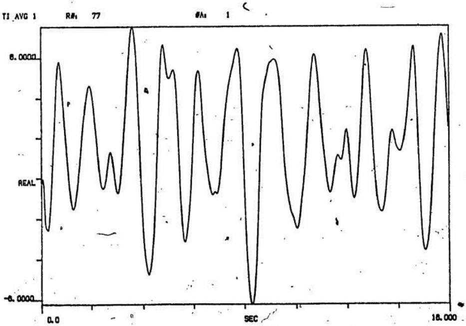

TIR21143

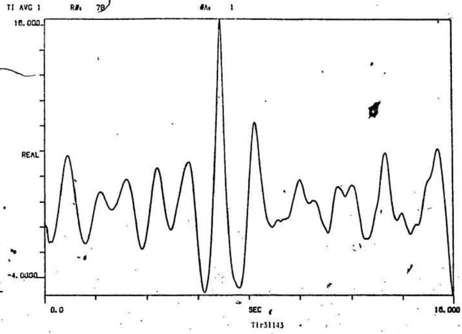
TI AVG 1
R#: 78
#A: 1
16.000
REAL
-4.0000
0.0
SEC
16.000
TIr31143

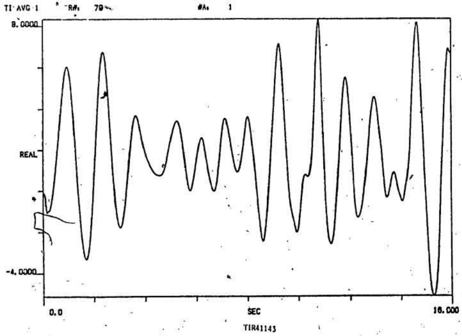
TI AVG 1
R#: 79
#A: 1
8.0000
REAL
-4.0000
0.0
SEC
16.000
TIR41143

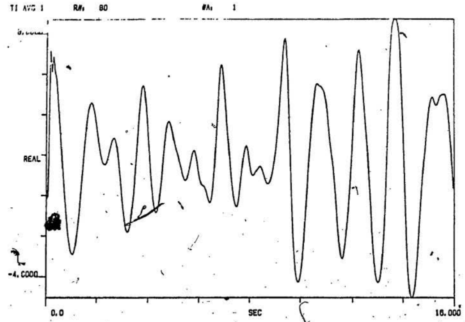

TIR11429

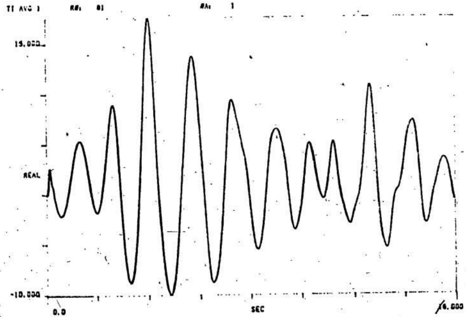

TIR21429

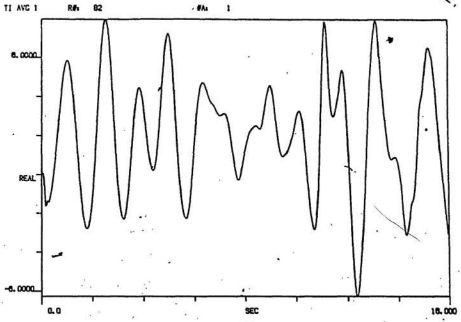

TIR31429

SPHERE

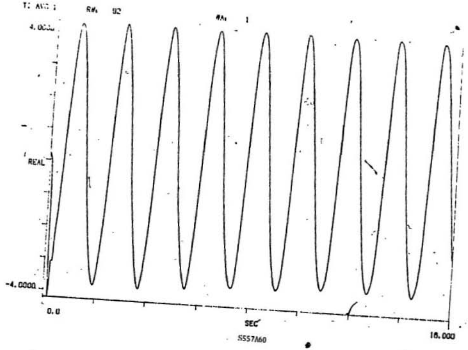

S557A60

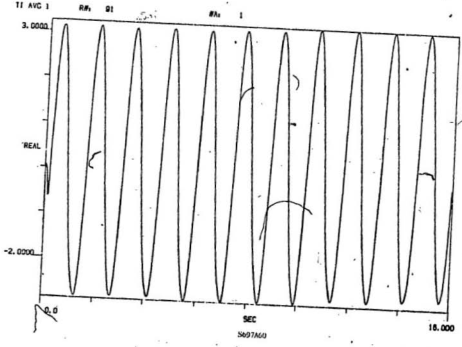

S697A60

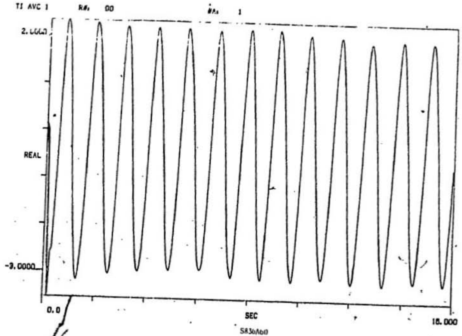
TI AVG 1
R#: 00
#A: 1
REAL
-3.0000
0.0
SEC
16.000
S836A60

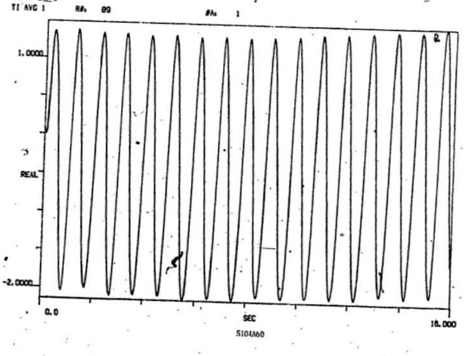
TI AVG 1
R#: 89
#A: 1
1.0000
REAL
-2.0000
0.0
SEC
16.000
S104A60

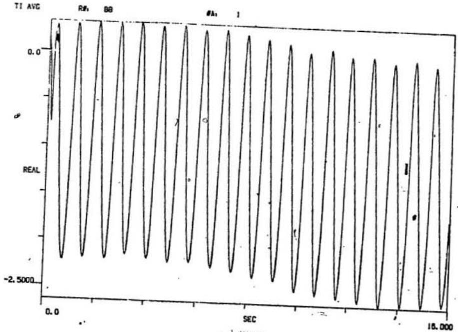

S119A60

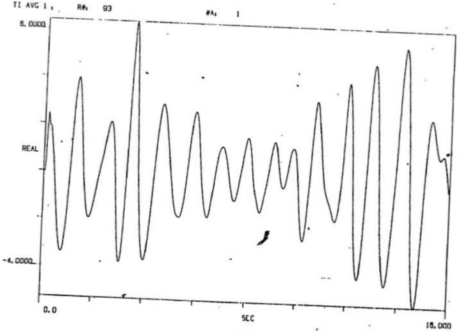

S1R1857

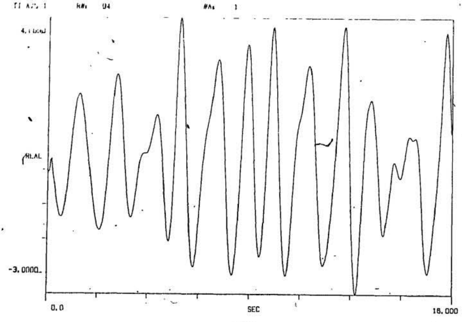

SIR2857

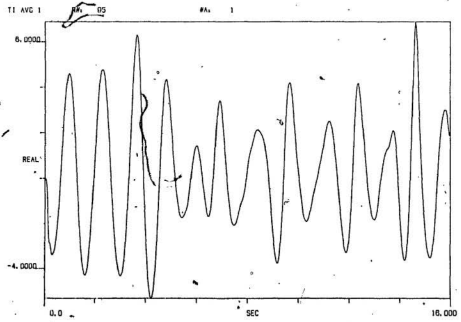

SIR3857

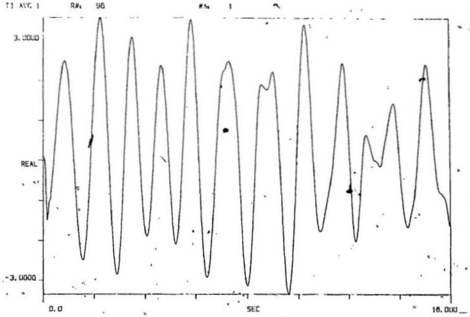

SIR4857

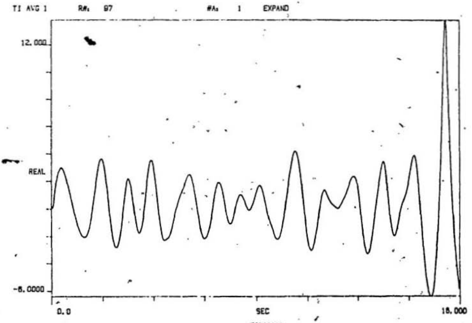

SIR11143

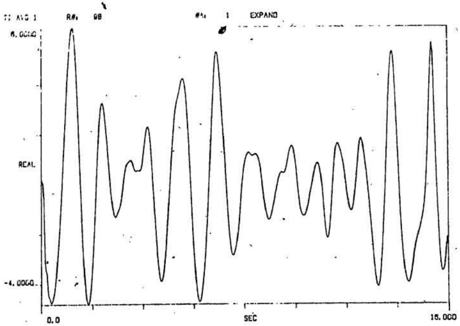

SIR21143

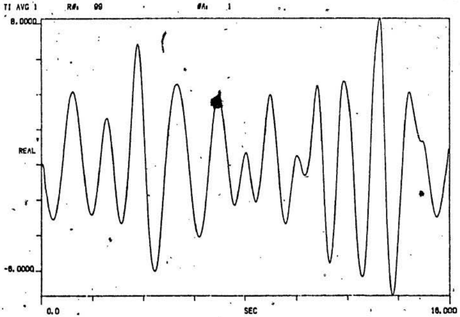

SIR31143

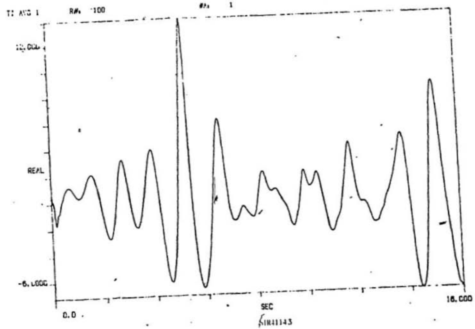

SIR41143

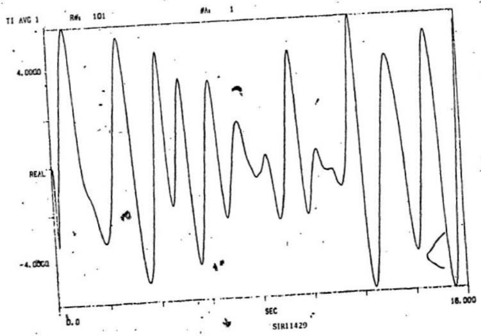

SIR11429

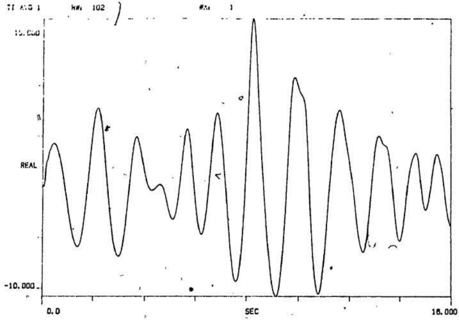

SIR21429

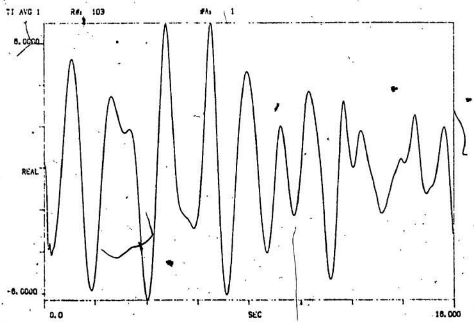

SIR31429

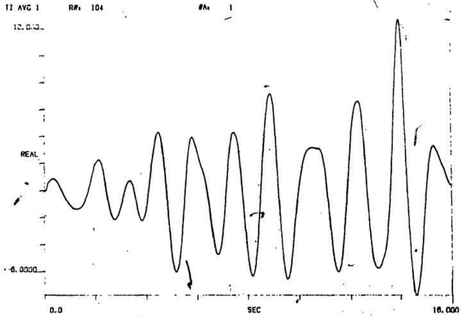

SIR41429